UNIVERSITY OF OKLAHOMA

GRADUATE COLLEGE

A MECHANISTIC ANALYSIS OF PARTICLE FLOW IN A MULTIPHASE CHEMICAL LOOPING REACTOR WITH THEORIES OF CONTACT MECHANICS

A THESIS

SUBMITTED TO THE GRADUATE FACULTY

in partial fulfillment of the requirements for the

Degree of

MASTER OF SCIENCE

By

SAYYAM CHOPRA
Norman, Oklahoma
2023

A MECHANISTIC ANALYSIS OF PARTICLE FLOW IN A MULTIPHASE CHEMICAL LOOPING REACTOR WITH THEORIES OF CONTACT MECHANICS

A THESIS APPROVED FOR THE
MEWBOURNE SCHOOL OF PETROLEUM AND GEOLOGICAL ENGINEERING

BY THE COMMITTEE CONSISTING OF

Dr. Baharak Sajjadi, Chair

Dr. Runar Nygaard

Dr. Reza Foudazi

ACKNOWLEDGEMENTS

I would like to express my sincere gratitude to my mentor and advisor, Dr. Baharak Sajjadi, for allowing me to work under her able guidance. Her support and expertise have helped me accomplish my research goal of working on sustainable energy technology.

During my time at OU MPGE, I was able to expand my technical knowledge, advance my skill set and learn Petroleum Engineering concepts from notable faculty members which has prepared me for a career in the petroleum engineering industry. I am grateful to everyone I have collaborated with during these two years. I am extremely grateful for the support I have received from Dr. Chandra S. Rai, Dr. Catalin Teodoriu, Dr. Deepak Devegowda, Ms. Katie Shapiro, and Mr. Derrick Whitney. This journey would not have been the same without your encouragement and support.

I am overwhelmed with appreciation and love for my parents and sister for never giving up on me and believing in me even when I resisted.

After two years of hard work and determination, I reached here when I decided to follow my passion. This process has taught me patience, endurance, and firm confidence that dreams come true.

TABLE OF CONTENT

ACKNOWLEDGEMENTS iv
LIST OF TABLES vi
LIST OF FIGURES vii
ABSTRACT x
CHAPTER 1: INTRODUCTION 1
1.1 Background 1
1.2 Problem statement 3
1.3 Objectives 4
1.4 Outline of thesis 5
Chapter 1: Introduction 5
Chapter 2: Literature Review 6
Chapter 3: Methodology 6
Chapter 4: Results and Discussions 6
CHAPTER 2: LITERATURE REVIEW 7
2.1 Introduction 7
2.1.1 Hydrogen Production from Fossil Fuels 10
2.1.2 Chemical Looping for Hydrogen Production 16
2.1.3 Chemical Looping Technologies (CLT) 17
2.1.4 Review of the Current CFD simulations and Pilot scale studies of CL Technology ... 26
CHAPTER 3: METHODOLOGY 33
3.1 CFD-DEM 33
3.1.1 Equations governing the Eulerian-Lagrangian approach (CFD-DEM model) 34
3.2 Reactor Design and its Working 39
3.3 Boundary Conditions 45
3.4 Simplification Assumption 46
CHAPTER 4: RESULTS AND DISCUSSIONS 49
4.1 Chemical looping flow pattern 49
4.2 Flow pattern in the fuel reactor 52
4.3 Flow pattern in Connection loop 56
4.3.1 Filling up of connection loop 56

4.3.2 Backflow in connection loop 60
4.4 Flow pattern in AR 62
4.4.1 Fluidization in the AR 62
4.4.2 Particles Rise in the AR 66
4.4.3 Flow pattern through Riser tube 69
4.5 Flow pattern in the Cyclone distributor 72
4.6 Flow pattern in downcomer 76
4.7 Impact of Velocity in AR on Chemical loop 79
4.8 Impact of Mass flow rate in FR on Chemical Loop 82
4.9 Backflow inside FR 86
4.10 Geometric Modification 91
4.10.1 Impact of variable Connection Loop diameter 91
CHAPTER 5: VALIDATION OF SIMULATION RESULTS 95
CHAPTER 6: CONCLUSIONS 97
Nomenclature 99
Reference 100
Appendix A: Probe setting 106
Appendix B: Meshing 107

LIST OF TABLES

Table 1: Advantages and challenges for the most used types of reactors for chemical looping applications 25
Table 2: Geometrical Parameters 42
Table 3: Mesh parameters and Conditions 43
Table 4: Simulation Parameters 45
Table 5: Initial Conditions 46
Table 6: Boundary Conditions 46

LIST OF FIGURES

Figure 1. IEA 2021-Global demand for pure hydrogen 2
Figure 2. Hydrogen production from fossil fuels and renewable sources and hydrogen applications 9
Figure 3. Hydrogen production processes from fossil fuels (adapted from (Nikolaidis & Poullikkas, 2017a)) 11
Figure 4. Hydrogen production processes from Renewable Sources (adapted from (Nikolaidis & Poullikkas, 2017a)) 14
Figure 5. Chemical Looping Combustion Principle (CLC). Me_xO_y is the metal oxide that is circulated. (adapted from (Lyngfelt, 2020). 18
Figure 6. Description of chemical-looping reforming (CLR) process (adapted from (Rydén et al., 2008)). 20
Figure 7. Diagram of CLG of biomass (adapted from (Roshan Kumar et al., 2022)). 20
Figure 8. Diagram of CLOU (adapted from (Li & Zhao, 2009)). 22
Figure 9. Diagram of CLOU (adapted from (Moghtaderi, 2010)). 23
Figure 10. Sketch of 120 kW Chemical looping pilot plant (AR…air reactor, FR…fuel reactor) 27
Figure 11. A fluidized bed with two components: 1 air reactor, 2 downcomers, 3 fuel reactors, 4 slots, 5 gas distributors, and 6 wind boxes. 29
Figure 12. Schematics of a 900 W continuous atmospheric CLR pilot plant 30
Figure 13. Schematics of a 25-kW CLC linked fluidized bed reactor. 31
Figure 14. Flow pattern of solid phase in a Gas-Fueled Chemical Looping Combustion Unit... 32
Figure 15. Reactor design with labeled sections and zones used for data analysis 41
Figure 16. Geometric design and sectional dimensions. 43
Figure 17. Quadrilateral meshing as viewed from the front. 44
Figure 18. Quadrilateral meshing as viewed from the top and front (cyclone distributor). 44
Figure 19. Circulation of catalytic solid particles between FR. (right) and AR (left) a) Particles velocity magnitude, b) Pressure in AR and riser. Simulation condition: V.AR: 3.2 m/sec, V_{FR}: 0.0025 kg/sec, Volume fraction of solid inside LC/AR/FR: 0.5 52
Figure 20. Circulation of catalytic solid particles inside FR. a) Velocity vectors magnitude, b) Particle velocity magnitude. Simulation condition: V_{AR}: 3.2 m/sec, V_{FR}: 0.0025 kg/sec, Volume fraction of solid inside LC/AR/FR: 0.5 54
Figure 21. Pressure contours in chemical loop during time interval of 3.3-7.4 sec. Simulation condition: V_{AR}: 3.2 m/sec, V_{FR}: 0.0025 kg/sec, Volume fraction of solid inside LC/AR/FR: 0.5 55
Figure 22. The graph between Pressure and time for — Avg (P_G) ZONE-F**,** — Avg (P_G) ZONE-G — and Avg (P_G) ZONE-A for time intervals 0-25seconds. 55
Figure 23. The graph between Volume fraction of Solids and time for — Avg (EP_S) ZONE-F and — Avg (EP_S) ZONE-G between time intervals 0-25 second 56

Figure 24. Circulation of catalytic solid particles inside connection loop a) Velocity vectors magnitude, b) Particle velocity magnitude. Simulation condition: V.AR: 3.2 m/sec, V_{FR}: 0.0025 kg/sec, Volume fraction of solid inside LC/AR/FR: 0.5 58
Figure 25. Pressure contours in chemical loop during time interval of 7.22-8.50 sec. Simulation condition: V.AR: 3.2 m/sec, V_{FR}: 0.0025 kg/sec, Volume fraction of solid inside LC/AR/FR: 0.5 58
Figure 26. The graph between Volume fraction of Solids and time for — Avg (EP_S) ZONE-A and — Avg (EP_S) ZONE-G between time intervals 0-25 second. 59
Figure 27. The graph between Gas velocity and time for — Avg (Gas_Velocity (Magnitude)) ZONE-A — Avg (Gas_Velocity (Magnitude)) ZONE-G between the time interval 0-25 sec. ... 59
Figure 28. Circulation of catalytic solid particles inside connection loop a) Velocity vectors magnitude, b) Particle velocity magnitude. Simulation condition: V.AR: 3.2 m/sec, V_{FR}: 0.0025 kg/sec, Volume fraction of solid inside LC/AR/FR: 0.5 61
Figure 29. Pressure contours in chemical loop during time interval of 6.98-7.20 sec. Simulation condition: V.AR: 3.2 m/sec, V_{FR}: 0.0025 kg/sec, Volume fraction of solid inside LC/AR/FR: 0.5 62
Figure 30. Circulation of catalytic solid particles inside AR a) Velocity vectors magnitude, b) Particle velocity magnitude. Simulation condition: V.AR: 3.2 m/sec, V_{FR}: 0.0025 kg/sec, Volume fraction of solid inside LC/AR/FR: 0.5..... 64
Figure 31. The graph between Pressure and time for —Avg(P_G) ZONE-A, — Avg(P_G) ZONE-B, — Avg(P_G) ZONE-D and — Avg(P_G) ZONE-H for time intervals 0-25seconds. 65
Figure 32. The graph between Volume fraction of Solids and time for — Avg (EP_S) ZONE-C, — Avg (EP_S) ZONE-D and — Avg (EP_S) ZONE-H between time intervals 0-25 second. ... 65
Figure 33. The graph between Gas velocity and time for — Avg (Gas Velocity (Magnitude)) ZONE-B, — Avg (Gas Velocity (Magnitude)) ZONE-C, and — Avg (Gas Velocity (Magnitude)) ZONE-H between the time interval 0-25 sec 66
Figure 34. Circulation of catalytic solid particles inside AR a) Velocity vectors magnitude, b) Particle velocity magnitude. Simulation condition: V.AR: 3.2 m/sec, V_{FR}: 0.0025 kg/sec, Volume fraction of solid inside LC/AR/FR: 0.5..... 69
Figure 35. Circulation of catalytic solid particles inside AR and riser a) Velocity vectors magnitude, b) Particle velocity magnitude. Simulation condition: V.AR: 3.2 m/sec, V_{FR}: 0.0025 kg/sec, Volume fraction of solid inside LC/AR/FR: 0.5 71
Figure 36. Pressure contours in chemical loop during time interval of 6.95-7.06 sec. Simulation condition: V.AR: 3.2 m/sec, V_{FR}: 0.0025 kg/sec, Volume fraction of solid inside LC/AR/FR: 0.5 72
Figure 37. Circulation of catalytic solid particles inside the cyclone distributor a) Velocity vectors magnitude, b) Particle velocity magnitude. Simulation condition: V.AR: 3.2 m/sec, V_{FR}: 0.0025 kg/sec, Volume fraction of solid inside LC/AR/FR: 0.5 74
Figure 38. The graph between Pressure and time for — Avg (P_G) ZONE-D, — Avg (P_G) ZONE-E, and — Avg (P_G) ZONE-F for time intervals 0-25seconds. 75
Figure 39. The graph between Volume fraction of Solids and time for — Avg (EP_S) ZONE-D, — Avg (EP_S) ZONE-E and — Avg (EP_S) ZONE-H between time intervals 0-25 second. 75

Figure 40. Circulation of catalytic solid particles inside the downcomer a) Velocity vectors magnitude, b) Particle velocity magnitude. Simulation condition: V.AR: 3.2 m/sec, V_{FR}: 0.0025 kg/sec, Volume fraction of solid inside LC/AR/FR: 0.5 78
Figure 41. The graph between Volume fraction of Solids and time for — Avg (EP_S) ZONE-E and — Avg (EP_S) ZONE-F between time intervals 0-25 second. 78
Figure 42. The graph between Pressure and time at ZONE-B for different velocities — Avg(P_G) Vel_2.6, — Avg(P_G) Vel_2.7, — Avg(P_G) Vel_3.2, and — Avg(P_G) Vel_3.5 for time intervals 0-25seconds..... 81
Figure 43. The graph between Pressure and time at ZONE-F for different velocities — Avg(P_G) Vel_2.6, — Avg(P_G) Vel_2.7, — Avg(P_G) Vel_3.2, and — Avg(P_G) Vel_3.5 for time intervals 0-25seconds..... 81
Figure 44. The graph between Volume fraction of Solids and time for different velocities. — Avg (EP_S) Vel_2.6, — Avg (EP_S) Vel_2.7, — Avg (EP_S) Vel_3.2, and — Avg (EP_S) Vel_3.5 between time intervals 0-25 second. 82
Figure 45. Circulation of catalytic solid particles inside the downcomer and FR. representing velocity vectors magnitude. Simulation condition: V.AR: 3.2 m/sec, Volume fraction of solid inside LC/AR/FR: 0.5. 84
Figure 46. The graph between Pressure and time at zone-F for different mass flow rate — Avg(P_G) MFR_0.0025, — Avg(P_G) MFR_0.0075, — Avg(P_G) MFR_0.05, and — Avg(P_G) MFR_0.1 for time intervals 0-25seconds. Zone-F 85
Figure 47. The graph between Volume fraction of Solids and time at zone-F for different mass flow rates — Avg (EP_S) MFR_0.0025, — Avg (EP_S) MFR_0.0075, — Avg (EP_S) MFR_0.05, and — Avg (EP_S) MFR_0.1 between time intervals 0-25 second..... 85
Figure 48. Circulation of catalytic solid particles inside the downcomer and FR. depicting backflow condition. a) Velocity vectors magnitude, b) Particle velocity magnitude. Simulation condition: V.AR: 3.2 m/sec, MFR_{FR}: 0.05 kg/sec, Volume fraction of solid inside LC/AR/FR: 0.5..... 89
Figure 49. The graph between Pressure and time at different zones — Avg(P_G) Zone-E and — Avg(P_G) Zone-F for time intervals 0-25seconds..... 90
Figure 50. The graph between Volume fraction of Solids and time at different zones — Avg (EP_S) Zone-E and — Avg (EP_S) Zone-F between time intervals 0-25 second. 90
Figure 51. The graph between Pressure and time at ZONE-B for different velocities — Avg(P_G) 25mm, — Avg(P_G) 30mm, — Avg(P_G) 35mm, and — Avg(P_G) 40mm for time intervals 0-25seconds..... 93
Figure 52. The graph between Pressure and time at ZONE-F for different velocities — Avg(P_G) 25mm, — Avg(P_G) 30mm, — Avg(P_G) 35mm, and — Avg(P_G) 40mm for time intervals 0-25seconds..... 94
Figure 53. The graph between Volume fraction of Solids and time at Zone-B for different velocities — Avg (EP_S) 25mm, — Avg (EP_S) 30mm, — Avg (EP_S) 35mm, and — Avg (EP_S) 40mm between time intervals 0-25 second. 94
Figure 54. Selection of probe at specific zones to determine data such as pressure, volume fraction and pressure 106
Figure 55. Poor meshing as a result of higher cell size selection 108

ABSTRACT

Understanding particles dynamics and their characteristics is essential to the operation, design, and optimization of chemical looping reactors. The chemical looping dry reforming (CLDR) process is a novel hydrogen production process in which methane and carbon dioxide mixture is converted into syngas in a cyclic oxidation-reduction reaction in the presence of an oxygen carrier. This paper presents a three-dimensional computational fluid dynamic model to study the fluid flow pattern in a chemical looping dry reforming methane (CLDRM) reactor. The numerical analysis was applied through Eulerian and Lagrangian approaches. This multiphase model design comprises a dual circulating fluidized bed consisting of a high-velocity air reactor (AR) with a high-velocity riser, a cyclone chamber (CC), a fluidizing bed fuel reactor (FR), and a connecting loop, which closes the loop between AR and FR. Analysis of gas-solid hydrodynamics in CLDRM was performed to understand the particles distribution, volume fraction, flow pattern, velocity and circulation between the AR and FR. The evolution of particle flow circulation rate was carefully analyzed to understand the particle material rebalance and the transfer of solid particles between reactors operating on different velocities. The results showed that the CLDR system experiences a pressure imbalance between the reduction and oxidation zones, which causes solid particles to undergo a highly intricate and turbulent pulse flow. This results in periodic bursts of pulses that lead to the intermittent transportation of particles — in the form of particle clusters— from high-pressure areas to regions with lower pressure. This paper discusses the impacts of velocity and geometric modifications on the distribution of the particles. The results showed that the fluidized beds exhibited a periodic pulse pattern with various phenomena occurring in a millisecond, and it was concluded that an air velocity of 3.2 m/sec, fuel mass flow rate of 0.0025 kg/sec, and connection loop diameter of 25 mm were idea operating parameters.

CHAPTER 1: INTRODUCTION

1.1 Background

The need for energy is increasing on a daily basis. It is backed up by findings about fossil fuels and other energy sources like hydrogen, solar electricity, wind power, or a combination of these technologies or geothermal energies (Sharma et al., 2021). Extensive research has been performed in the field of oil and gas, and several technological advancement have been achieved both with experimentation and machine learning (Sharma et al., 2023; Sharma et al., 2020). Hydrogen and energy have a long history together, from powering the earliest internal combustion engines over 200 years ago to becoming an essential component of today's refining industry. It is lightweight, storable, and energy dense, with no direct emissions of pollutants or greenhouse gases. Hydrogen has a very high energy density as an energy carrier. It can be seen as a promising alternative source for addressing the diminishing concerns of fossil fuels as well as environmental issues such as greenhouse gas emissions and pollution. However, for hydrogen to make a meaningful contribution to clean energy transitions, it must be accepted in sectors where it is almost totally absent, such as transportation, buildings, and power production. Hydrogen supply to industrial users is currently a substantial industry all over the world. Demand for hydrogen has more than tripled since 1975 (Figure 1), and it is nearly completely provided by fossil fuels, with 6% of world natural gas and 2% of global coal going to hydrogen production (Sgouros & Digkas, 2021). According to the International Energy Agency (IEA) publication, Energy Technology Perspectives 2017 (Figure 1), fossil fuels will continue to be the dominant source of hydrogen in the United States (-75%), Europe (-65%), and Japan (-85 percent) by 2050. This estimate is based on the abundance of fossil fuels in the region, the cheap cost of hydrogen production, and the various benefits (e.g., lower emissions via CCUS) of getting hydrogen from fossil fuels rather than directly

utilizing them for power generation. Hydrogen can be seen as a promising alternative source for addressing the diminishing concerns of fossil fuels as well as environmental issues such as greenhouse gas emissions and pollution (Xu et al., 2019).Considering fossil fuels to produce hydrogen, altogether, 144 billion cubic meters of methane are either flared into the atmosphere or used as a fossil fuel which emits a comparatively higher concentrations of inevitable carbon dioxide. Because methane resources are abundant, researchers have concentrated their efforts on reforming methane into liquid fuels or hydrogen. The focus on these sources, which generate larger volumes of unavoidable carbon dioxide, has provided incentive for major research into converting methane into liquid fuels or hydrogen. The process of converting methane into a syngas combination (CO/H_2) (Kang et al., 2020), which can also be utilized as a raw material for liquid hydrocarbon synthesis, offers a sustainable alternative to methane combustion.

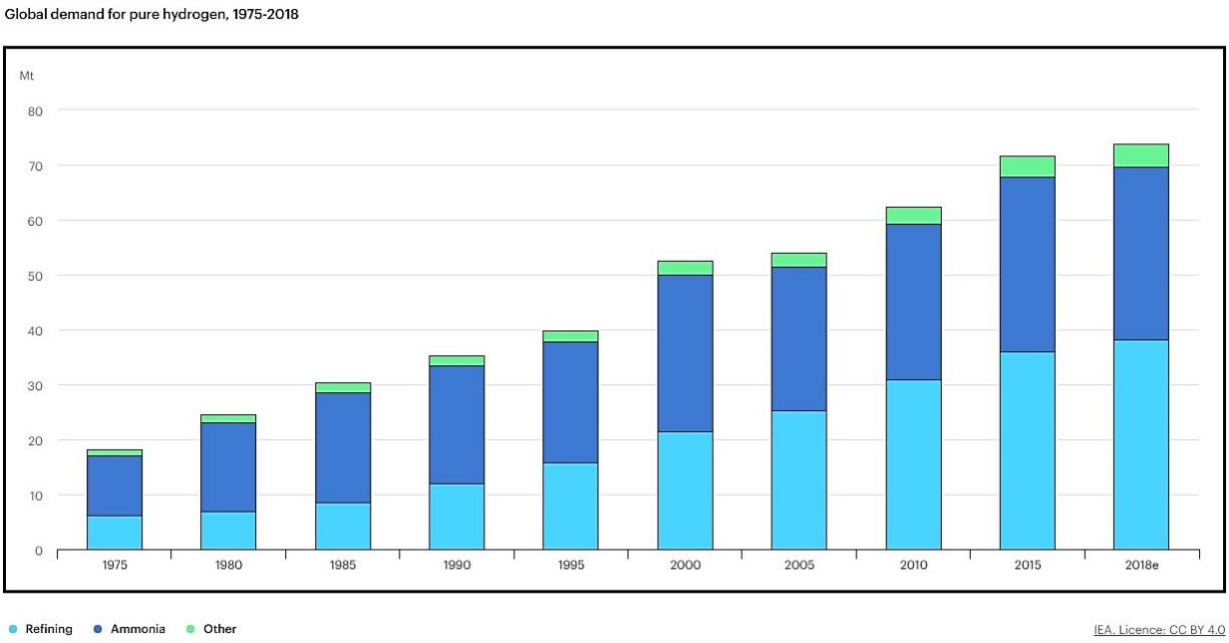

Figure 1. IEA 2021-Global demand for pure hydrogen

1.2 Problem statement

Several methods for producing syngas from methane have been proposed, including steam reforming of methane (SRM), partial oxidation (POX), auto-thermal reforming (ATR), and dry reforming methane (DRM) (Mantripragada & Veser, 2021). Each of these processes has inherent advantages as well as disadvantages. In SRM, methane reacts with steam to produce syngas with a stoichiometric H_2/CO ratio of 3 (Chibane & Djellouli, 2011). This process is highly endothermic. The benefit of a high H_2/CO ratio and relatively more specific process conditions in comparison to POX and ATR make SRM the most widely used technology for hydrogen production to date (Carapellucci & Giordano, 2020). Unlike steam reforming, "dry reforming" of methane (DRM) uses CO_2 as the oxidizing agent for methane. In DRM, CH_4 reacts with CO_2 to produce syngas with an H_2/CO ratio of 1. SRM is a mature commercial process typically utilizing Ni-based catalysts, while DRM has not been tested commercially due to limitations. It is typically based on expensive bi-metallic or noble metal catalysts, and it is hampered by carbon deposition during the reaction, which causes catalyst degradation and decreases the reaction's effectiveness. Also, a high reaction temperature is required for Dry Reforming of Methane (DRM) (Löfberg et al., 2017). There is a need to develop and integrate a new approach that eliminates the shortcomings of these processes, such as high endothermic heat, catalyst deactivation, coke deposition, the usage of cryogenic air separation, and the requirement for expensive noble metal catalysts. Integrating chemical looping (CL) with DR overcomes the problems of reforming procedures, the issue of CO_2 capture, and excessive NOx emissions (Khan & Shamim, 2016), enables the synthesis of syngas and H_2 at a reasonable cost. The chemical looping reaction strategy involves dividing a reaction into numerous auxiliary responses, which are helped by solid intermediates known as 'oxygen carriers,' which alternate between reacted and regenerated states. The oxygen carrier,

which is frequently comprised of metal oxides, nitrides, hydrides, and sulfides, acts as a reservoir for oxygen donation and regeneration. One such reforming approach is chemical looping dry reforming (CLDR), which tries to achieve significant oxygen carrier reduction in the first half-cycle to maximize CO_2 consumption. It employs a bifunctional looping material that combines the role of oxygen storage for redox cycling with catalytic activity for efficient fuel conversion. It converts syngas from the looping process's two reactors into two streams of CO and H_2 (Yu et al., 2019). CO_2 may be used as an oxidant, resulting in a unique approach for successfully utilizing CO_2 by reducing it to CO (Hu et al., 2018). To construct the carriers that will be employed in combination with the system's reactor architecture, a partnership between reaction engineering and particle physics is required for any chemical looping application. Chemical looping reactors include a very complicated dual looped circulating fluidized beds which work under turbulent conditions. A thorough analysis of gas-solid fluxes, particular section design characteristics, the use of valves (mechanical and non-mechanical), and transport phenomena is required for the proper design of CL reactors. Correct design of the reactor and control over the circulation of the particles are among the core issues in the scale-up of CL reactors. CFD simulation can help minimize the challenges associated with the design of this kind of complicated reactors and at the same time provide analysis data such as oxidation capabilities, particle flow dynamics and impact of chemical reaction on the system without a need to invest into experimentation.

1.3 Objectives

The chemical looping reactor includes complicated interactions of particle-particle, particle-gas, and particle-gas in a turbulent dual looping fluidized bed. Understanding the fluid flow pattern in these reactors, controlling the solid particles circulation, and reducing the instabilities may further

advance the development of these reactors. Therefore, the motivation for this research can be split into four segments:

a. Analysis of fluid flow pattern in Air Reactor (AR), Fuel Reactor (FR), Connection Loop (also known as seal loop) (CL or SL), Cyclone Distributor (CD), and Downcomer using a transient 3D CFD-Discrete Element Modelling (DEM).
b. Investigation of instabilities in CL reactor, which includes back flows, formation of vortexes, and development of high-pressure zones.
c. Investigation of the impacts key variable including the AR and FR inlet velocities, and reactor geometry specifically the diameter of connection loop.
d. Investigation of the impact of spring factor which is the most important simulation parameter specifying the particle-particle interactions in CFD-DEM modeling.

1.4 Outline of thesis

Chapter 1: Introduction

This chapter contains a concise introduction to the problems/limitations related to the hydrogen production, chemical looping (CL) technology and different CL reactors used for hydrogen production. We briefly highlight a number of challenges associated with the design of chemical looping reactors and explain about the model developed in this study to simulate the fluid flow pattern, instabilities, and key variables in CL reactors. The objectives of the project are formed, and the outline of the thesis is clarified.

CHAPTER 2: LITERATURE REVIEW

The first part of this chapter provides a comprehensive literature survey of the classification of hydrogen production processes and the importance of modern hydrogen synthesis techniques, e.g., chemical looping technology. Accordingly, the main categories of chemical looping technology are reviewed with additional focus on hydrogen production through this technology. The second part of this chapter presents a brief review of the designs of the chemical looping reactors through computational Fluid Dynamics (CFD).

CHAPTER 3: METHODOLOGY

In this chapter, the essential background and fundamental equations, models and theories used for CFD-DEM simulation of fluid flow pattern in CL technology in the current study, are provided. All explanations are based on Eulerian-Lagrangian approach. This chapter also includes all of the parameters and values applied to the initial conditions, boundary conditions, and all variable. Based on all these equations and variables, a transient 3D simulation model was developed using ANSYS and simulated using MFiX 22.4 —Multiphase Flow with Interphase eXchanges.

CHAPTER 4: RESULTS AND DISCUSSIONS

This chapter is divided and presented in three parts. The first section includes understanding typical flow patterns and behaviors found inside the chemical loop, as well as insight into backflow phenomena noticed in the connecting loop and FR. The second section addresses operational characteristics such as AR velocity, and FR. mass flow rate, as well as their effects on geometric configurations. Each of these characteristics is important in understanding gas and particles hydrodynamics. The output data is classified as cell data, which is simulated using a Eulerian and Lagrangian framework and offers fluid data such as pressure contours and gas phase volume

percentage. The third part of the chapter discusses particle data that is described in a Lagrangian framework and offers solid data such as diameter, translational velocity, rotational velocity, and, and residence time.

CHAPTER 2: LITERATURE REVIEW

2.1 Introduction

Because of the repercussions of climate change caused by the production of carbon dioxide and greenhouse gases, as well as the depletion of fossil fuels, it is critical for humans to pursue future energy sources that are sustainable and carbon-free (Nikolaidis & Poullikkas, 2017a; Rafi et al., 2023). Hydrogen is the sole carbon-free energy carrier and the most plentiful element on the Earth; yet it is typically found in conjunction with other elements. Hydrogen has long been regarded as an ecologically friendly secondary source of renewable energy (Momirlan & Veziroglu, 2005). During the production of hydrogen by hydrocarbons and biomass, a synthesis gas called 'syngas' is formed at some point of the process. Syngas is essentially a mixture containing mainly hydrogen and carbon monoxide and it is generated in all hydrogen production processes with a hydrocarbon feed and is the mainstream for hydrogen processing and separation (Kothari et al., 2008a).

Hydrogen can be critical in the transition to a low-carbon economy. At the moment, hydrogen is largely employed in the following applications:

- As a chemical component in the synthesis of ammonia (NH_3) (fertilizers)
- As a catalyst and chemical feedstock
- As a hydrogenating component in food and pharmaceutical manufacture
- As a chemical component in the production of petrochemicals and refineries
- As a low-carbon fuel for transportation, generation of energy, and manufacturing

Many processes can generate hydrogen, which can be classified as either conventional or renewable. Natural gas and coal are utilized as feedstocks in conventional technologies, whereas biomass, solar, and wind are used in renewable technologies. These operations generate hydrogen, which may be stored, transported, and supplied, as well as utilized to generate energy (Figure 2). It is also crucial to emphasize the importance of the energy storage system (Hadjipaschalis et al., 2009) which must be adaptable enough to (a) keep the stored energy for the specified length and (b) deliver energy when needed. A variety of techniques can be used to create hydrogen. First, thermochemical processes liberate hydrogen from their molecular structure by utilizing the energy in diverse resources such as natural gas, coal, or biomass. Heat, in conjunction with closed-chemical cycles, creates hydrogen from feedstocks such as water in other processes. The biomass resources are processed using thermochemical and biological methods. Each technique employs a variety of technology. Pyrolysis, gasification, combustion, liquefaction, and bio-photolysis and biological fermentation are all examples of thermochemical techniques. Steam methane reforming, for example, happens in the hydrocarbon process of fossil fuels, while pyrolysis and gasification of biomass and waste generated come from thermochemical processing of renewable sources. Second, electrolyzes split water into hydrogen and oxygen using electricity. This technology is highly established and commercially accessible, and systems that can utilize intermittent renewable energy effectively are being developed. Third, water, being a renewable resource, may be utilized to generate hydrogen by water-splitting techniques. Photolytic or direct solar water splitting techniques employ light energy to split water into hydrogen and oxygen. These techniques are currently at varying phases of development, but they have the potential to provide long-term sustainable hydrogen production with little environmental effect. Finally, microorganisms such as bacteria and microalgae can generate hydrogen via biological processes involving sunlight or

organic materials. These latter technological routes are still in the research and development stage, but they offer the potential for long-term, low-carbon hydrogen generation. With the exception of electrolysis, biomass gasification, and steam/coal-based reforming, the most of these technologies are either in development or in small scale testing, necessitating the need to explore and advance these processes

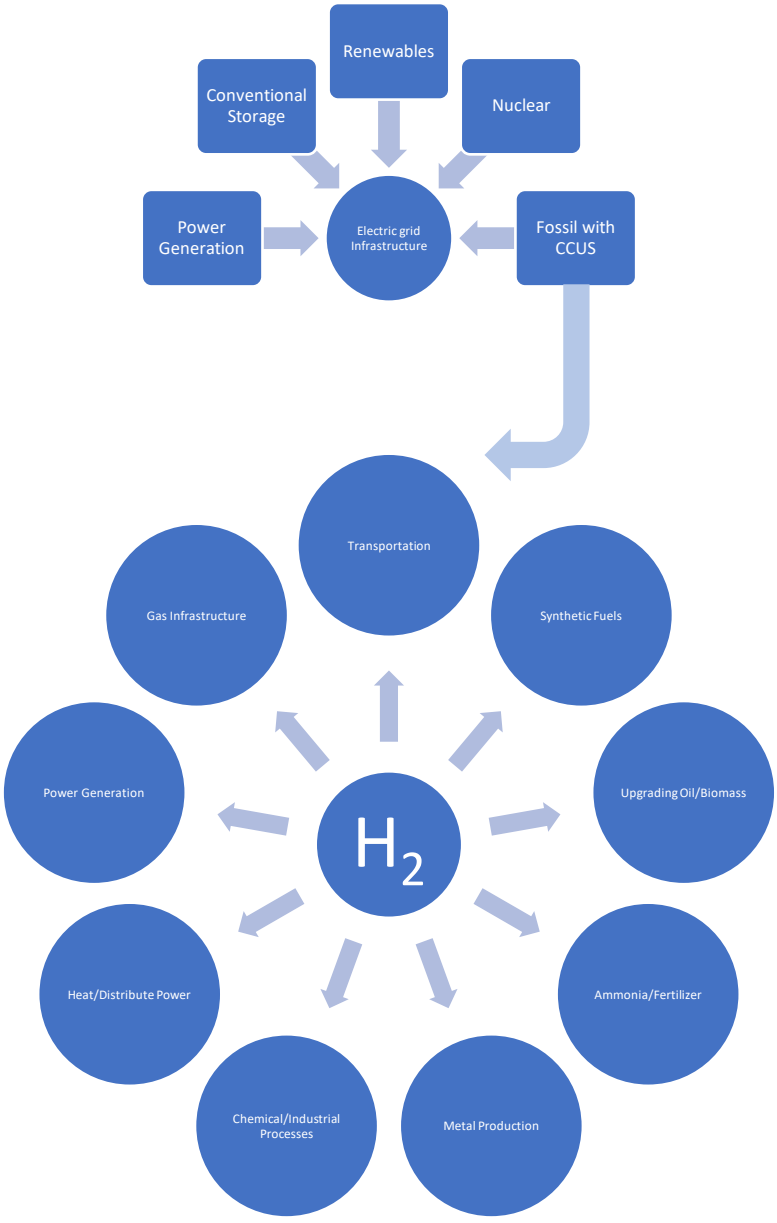

Figure 2. Hydrogen production from fossil fuels and renewable sources and hydrogen applications

Today, natural gas reforming in big central facilities produces 95% of the hydrogen generated in the United States. Today, low-cost natural gas reforming can generate hydrogen for fuel cell electric cars (FCEVs) and other purposes. Long-term hydrogen generation from natural gas will be complemented by renewable, nuclear, coal (with carbon capture and storage), and other low-carbon domestic energy sources. This is a critical technological approach for near-term hydrogen production.

2.1.1 Hydrogen Production from Fossil Fuels

2.1.1.1 Hydrocarbon reforming process

Hydrocarbon reforming and pyrolysis Figure 3 technologies have been successfully developed to convert fossil fuels to hydrogen. These are two old methods of producing hydrogen utilizing traditional resources or fossil fuels (Figure 3). Chemical processes such as steam reforming, partial oxidation, and autothermal steam reforming are used in the hydrocarbon reforming process. So far, hydrogen has been produced in 48% of cases from natural gas (NG), 30 percent from heavy oil and naphtha reforming in refinery/chemical industrial off-gases, 18% from coal gasification, 3.9% from water electrolysis, and 0.1 percent from other sources (Kothari et al., 2008b) (Muradov & Veziroğlu, 2005). In the United States, 99% of hydrogen is produced from fossil fuels, with 95% originating from natural gas by steam methane reforming and 4% from partial oxidation of natural gas via coal gasification (DOE 2020).

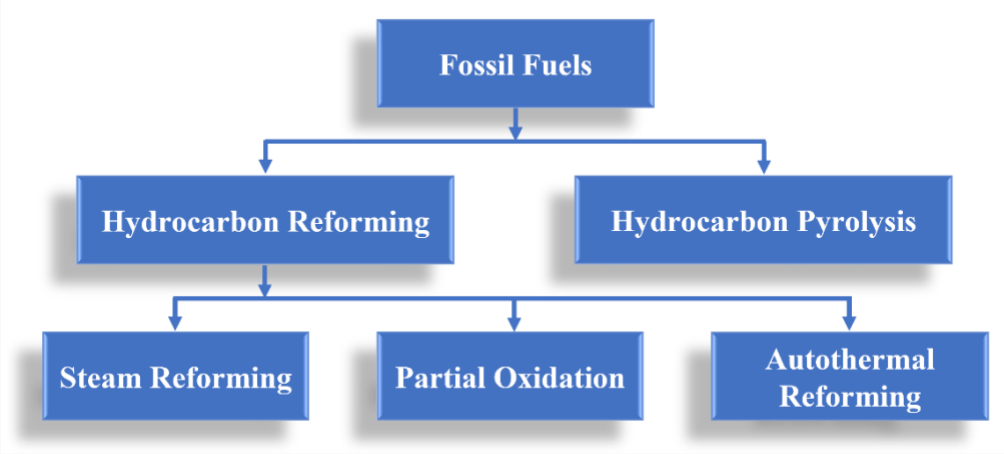

Figure 3. Hydrogen production processes from fossil fuels (adapted from (Nikolaidis & Poullikkas, 2017a))

Steam Methane Reforming (SMR)

The steam methane reforming (SMR) process is unquestionably the most widely used process for hydrogen production globally, owing to its high conversion and appealing economics, which are a result of the high process efficiency (65-80 percent) and lower capital cost compared to other syngas production technologies (Muradov, 2008). Steam reforming is the catalytic process by which methane and light hydrocarbons are transformed to syngas in the presence of steam.

The initial stage in the manufacturing of syngas from natural gas through SRM (or other methane reforming processes) is the desulphurization of the input fuel. Sulphur is removed from light hydrocarbons such as natural gas and refined petroleum products using the desulfurization process (Rothenberg, 2013). This process step is required to prevent the sulphur content from poisoning and deactivating the downstream reactor catalysts. The first step is to catalytically hydrogenate the sulphur organic molecules to produce H2S. Co-Mo catalyst (290-370 ^{o}C) (Armor, 1999) and the created H_2S is then scrubbed onto a ZnO bed (340-390 ^{o}C) to get ZnS and H2O in the second stage. The reaction describes the latter:

$$H_2S + ZnO \rightarrow ZnS + H_2O \quad (1)$$

Natural gas supply often contains heavier hydrocarbon fractions that are removed one step before the primary reformer, a process known as pre-reforming. The heavier fractions are more reactive, and when they react, they cause carbon deposition, which deactivates the reformer catalyst. The pre-reformer is an adiabatic reactor that operates at lower temperatures than traditional reforming (inlet temperature of 450 - 600 °C) ("Index," 2014). Along with the breakdown of the higher hydrocarbons, some hydrogen is created at this step. The process gas is warmed to 500 °C, compressed to 26 bar pressure, and delivered to the reforming reactor after pre-reforming. The reactor tubes are filled with Ni catalyst and put within a furnace where the burners supply the necessary heat demand to accomplish the needed conversion at 850 - 900 °C dependent on the reaction:

$$CH_4 + H_2O \leftrightarrow 3H_2 + CO \quad \Delta H^{298K} = 205.8\ kJ/mol \quad (2)$$

Because the reaction is extremely endothermic, heat from a furnace is used in a fired tubular reactor (FTR). Although the reaction is favored by low pressures since two moles create four moles of products, high operating pressures (20-26 bar) are favored in industrial settings because hydrogen is required at these pressures in later stages of processing and to lower the unit's volume. Because high pressure enhances the reactor's production rate, a more compact reactor is required, resulting in material cost savings. While the reaction's stoichiometry on the reactants is 1:1, an excess of steam (2.5-3 to methane) is injected to minimize carbon deposition on the catalyst since the gas includes more accessible oxygen. Carbon deposition in the steam reformer reactor is caused by three reactions: a) methane breakdown to H2 and C, b) CO to C and CO_2, known as the Boudouard reaction, and c) carbon monoxide reduction. (Snoeck et al., 2002).

$$CH_4 \leftrightarrow C + 2H_2 \quad \Delta H^{298K} = 122.3\ kJ/mol \quad (3)$$

$$2CO \leftrightarrow C + CO_2 \; \Delta H^{298K} = -125.2 \; kJ/mol \quad (4)$$

$$CO + H_2 \leftrightarrow C + H_2O \; \Delta H^{298K} = -84 \; kJ/mol \quad (5)$$

Partial Oxidation (POX) Method

Steam, oxygen, and hydrocarbons are converted to hydrogen and carbon oxides using the partial oxidation (POX) process. Because the POX process is exothermic, it takes less energy than the steam reforming approach. However, an air separation unit (ASU) is necessary to produce pure O_2 for POX, which dramatically raises the plant's construction and operational costs. Yet, the POX process is the most suited technology for converting heavy hydrocarbon feedstocks such as oil wastes, naphtha, coal, and light hydrocarbon (methane) to hydrogen.

$$C_mH_n + m/2O_2 \rightarrow n/2H_2 + mCO \quad (6)$$

Lighter feedstock, such as natural gas or naphtha, is used in catalytic reactions *(Steinberg & Cheng, 1989)* and it function at temperatures ranging from 700 to 900 °C and pressures ranging from 25 to 35 bar, whilst non-catalytic ones work at temperatures ranging from 1150 to 1500 °C and pressures ranging from 25 to 80 bar *(Iulianelli & Basile, 2014)*. The syngas generated by non-catalytic POX has a very high temperature of 1,200-1,400°C and significant impurities due to the heavy hydrocarbon feedstocks that must be cleaned and cooled *(Elbadawi et al., 2021)*. Texaco and Shell worked together to create a non-catalytic POX that produced a high syngas yield at high temperatures and pressures *(Pen˜a et al., 1996)*. The pure oxygen supply and considerable safety risk are two key downsides of the POX method. Because of the lower hydrogen-to-carbon ratios of the heavy feedstocks utilized in the POX process, a large amount of the hydrogen is created from steam.

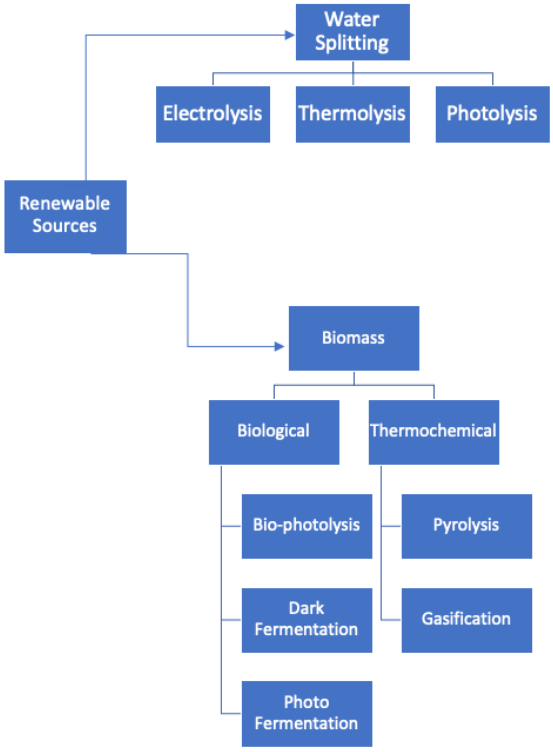

Figure 4. Hydrogen production processes from Renewable Sources (adapted from (Nikolaidis & Poullikkas, 2017a))

Autothermal Reforming (ATR)

Autothermal reforming is a hybrid of the two previously stated technologies, SMR and POX, in which the heat necessary for the reforming component is produced by the combustion of the feed in an adiabatic reactor. As a result, this approach employs the exothermic partial oxidation process to give the required thermal energy and the endothermic steam reforming process to boost hydrogen production. In ATR, the reaction (7) occurs in the early section of the reactor, in the combustion chamber, and supplies heat and steam for the reforming processes that occur in the catalytic zone to produce hydrogen. Generally, in the autothermal reforming process, steam and oxygen or air are introduced into the reformer, and the oxidation and reforming processes proceed concurrently *(Nikolaidis & Poullikkas, 2017b)*.

$$CH_4 + 3/2O_2 \rightarrow 2H_2O + CO \ \Delta H^{298K} = 519.0\ kJ/mo \quad (7)$$

The autothermal reforming process has a thermal efficiency of 60-75% when using methane as the feedstock, the optimum operating conditions are at inlet temperatures of around 700°C for steam to carbon (S/C) ratio 1.5 and oxygen to carbon (O_2/C) ratio 0.45, and the maximum hydrogen yield is around 2.8 (Halabi et al., 2008). The H_2/CO ratio may be adjusted by altering the amount of O_2 and H_2O fed and the temperature with the gases exiting at temperatures over 1000 °C. Because ATR consumes less oxygen than POX, the cost of pure O_2 supply is lowered [16]. Because N_2 is required in the ammonia synthesis process, air can be utilized as the feed instead of pure O_2. When compared to the SMR arrangement, ATR can withstand pressures of up to 80 bar and has a more compact design, resulting in a smaller plant footprint; nevertheless, when utilized for pure hydrogen generation, the capital cost is raised since an ASU unit is required to generate pure O_2 (Liu et al., 2009).

Autothermal Reforming Combined with Gas Heated Reforming (ATR + GHR)

To considerably boost process efficiency, the ATR can be paired with a gas heated reformer (GHR). The heated gases exiting the ATR (1020-1050 °C) provide some of the heat for the endothermic steam reforming that occurs within the GHR in the ATR-GHR scenario. The ATR reactor vessel is made up of a refractory-lined pressure shell, a combustion zone, and a fixed catalyst bed. ATR is typically operated at temperatures ranging from 950 to 1050°C, pressures ranging from 30 to 50 bar, a steam-to-carbon molar ratio (S/C ratio) of 0.5-1.5, and an oxygen-to-carbon molar ratio (O/C ratio) of 0.6-1.0 (Lamb et al., 2020).

2.1.2 Chemical Looping for Hydrogen Production

Chemical looping methods offer an intriguing alternative for electricity and/or hydrogen generation when paired with CO_2 collection, which is more efficient than traditional CO_2 capture technology (Erlach et al., 2011; Spallina et al., 2013). Chemical looping is a method for addressing CO_2 collection and low NOx emissions (Khan & Shamim, 2016) and it enables the low-cost production of compounds such as syngas and H_2. The chemical looping reaction strategy involves dividing a reaction into numerous auxiliary responses, which are helped by solid intermediates known as "oxygen carriers", which alternate between reacted and regenerated states. The phrase "chemical looping" refers to the process of breaking down a reaction into discrete reactions in which the intermediates are in a continuous cycle of reaction and regeneration. The purpose of this procedure is to allow these reactions to take place in a way that maximizes system efficiency while also making it simple to separate the necessary products, making the process more efficient and cost effective. In 1987, Ishida et al. (Ishida et al., 1987) were the first to coin the phrase "chemical looping" to describe a method of using a metal oxide as an intermediate mechanism to accomplish a cyclic oxidation-reduction reaction process for power generation. A solid is employed as an oxygen-carrier (OC) in chemical looping processes to convert the fuel, and the solid is then oxidized with air in a continuous cycle. The oxygen carrier, which is frequently comprised of metal oxides, nitrides, hydrides, and sulfides, acts as a reservoir for oxygen donation and regeneration. A redox loop is formed in a conventional chemical looping process, consisting of two or more reduction and oxidation stages. An oxygen carrier or redox catalyst initially transfers the most basic form of its lattice oxygen (Zhu et al., 2020). When the reduced oxygen carrier is exposed to an oxidant to replace its lattice oxygen, a two-step redox cycle is completed.

2.1.3 Chemical Looping Technologies (CLT)

CO_2 emissions must be reduced since they contribute considerably to global climate change. Carbon dioxide emissions from anthropogenic sources have received significant attention in recent decades, resulting in the fast development of carbon capture and storage technology (CCS). CCS is expected to be the ultimate technology capable of reducing carbon emissions and may one day play an important role in mitigating the greenhouse effect (Yao et al., 2023). Nonetheless, large-scale commercial adoption of CCS technology is currently quite limited, owing mostly to the substantial energy-efficiency penalty associated with ASU (air separation unit) operation (Czakiert et al., 2022). This issue, however, is unrelated to the novel approach of chemical looping combustion CLC (Hossain & de Lasa, 2008), where solid particles are employed to carry oxygen from combustion air to the burning fuel.

Chemical looping is a significant group of technologies that may be utilized for direct combustion, gasification, oxygen uncoupling, air separation, oxidative dehydrogenation, and epoxidation. In this technology, oxygen is added to the fuel gas via a solid carrier before it is released as a pure CO_2 stream suitable for consumption or, more likely, sequestration or storage. In chemical looping combustion, the oxygen carrier is typically a metal oxide, such as iron or copper oxide, which reacts with the fuel in a circulating fluidized bed reactor. As the metal oxide is reduced, it releases oxygen to the fuel, generating heat and producing a reduced metal product that is then reoxidized with air to regenerate the oxygen carrier. Chemical looping can also be used for other processes, such as gasification, where the oxygen carrier is used to convert solid fuels into a gaseous product, or for air separation, where the oxygen carrier is used to selectively extract oxygen from air. Other applications include oxidative dehydrogenation and epoxidation, where the oxygen carrier is used to catalyze specific chemical reactions.

Chemical Looping Combustion (CLC)

In the conventional chemical looping system Figure 5, the whole process may be thought of as burning and partial oxidation/reforming of the fuels, which necessitates certain oxygen carrier properties in order to effectively regulate the product selectivity (Zheng et al., 2022).

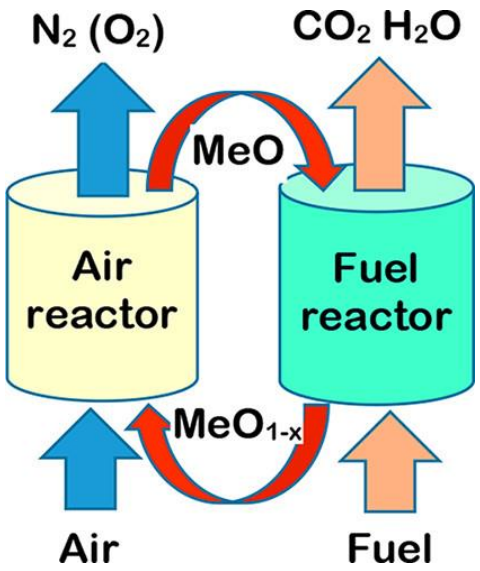

Figure 5. Chemical Looping Combustion Principle (CLC). Me_xO_y is the metal oxide that is circulated. (adapted from (Lyngfelt, 2020).

The CLC process is typically carried out in a two-reactor system consisting of the fuel reactor (FR), where combustion occurs, and the air reactor (AR), where oxygen carriers are regenerated. Thus, oxygen carriers are continuously oxidized and reduced (Eq. 8 and Eq. 9) as they flow throughout the combined CLC unit (Czakiert et al., 2022).

$$(2n + m)Me_xO_{y-1} + (n + 0.5m)O_2 \rightarrow (2n + m)Me_xO_y \quad (8)$$

$$C_nH_{2m} + (2n + m)Me_xO_y \rightarrow nCO_2 + mH_2O + (2n + m)Me_xO_{y-1} \quad (9)$$

Chemical Looping Reforming

Methane reforming is regarded as one of the key approaches for producing syngas from natural gas or renewable methane resources such as biogas. SRM (Eq. 10) and DRM (Eq. 11) entail the presence of an oxidant that transforms organic carbon to CO while also producing H_2 (Rydén et al., 2008) (Aouad et al., 2018). These techniques usually involve a high-temperature catalytic reformer for syngas generation, an intermediate-temperature WGS unit for hydrogen enrichment, and a low-temperature chemical/physical separation for carbon dioxide removal. Eventually, substantial catalyst deactivation occurs, either by coke buildup or active phase sintering, whereas their reactivity and selectivity are mostly regulated by thermodynamic constraints and concomitant RWGS reaction. Hao Zheng et al. (Zheng et al., 2022) demonstrated the fundamental strategies used for this CLR processes through equations 10 and 11.

$$C_nH_m + nH_2O \leftrightarrow nCO + \left(n + \frac{1}{2m}\right)H_2 \quad (10)$$

$$C_nH_m + nCO_2 \leftrightarrow 2nCO + 1/2mH_2 \quad (11)$$

Chemical looping reforming (CLR) (Figure 6), on the other hand, provides a viable alternative for creating syngas from carbonaceous fuel with inherent gas-gas separation. To present, numerous CLR processes have been developed that use various feedstocks (such as natural gas, oil, and ethanol) and oxygen carriers (such as Ni, Cu, Mn, and Fe oxides).

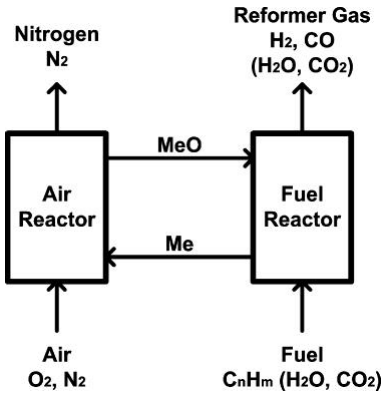

Figure 6. Description of chemical-looping reforming (CLR) process (adapted from (Rydén et al., 2008)).

Chemical Looping Gasification

Chemical looping gasification (CLG) of biomass is a revolutionary gasification technique for producing high-quality syngas for use in the downstream fuel synthesis process, with the inherent benefit of limiting CO2 emissions to the product gas stream (Roshan Kumar et al., 2022).

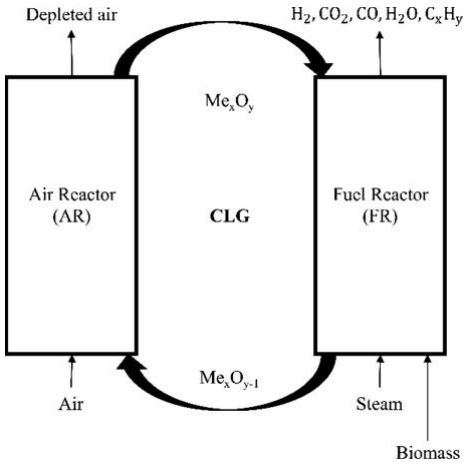

Figure 7. Diagram of CLG of biomass (adapted from (Roshan Kumar et al., 2022)).

CLG is the most promising process option for obtaining genuine and feasible negative emission solutions for Bio-Energy with Carbon Capture and Storage (NET) (Di Giuliano et al., 2022). As a

result, CLG would allow for lower expenses associated with carbon sequestration and gas cleansing. FR and AR reactions using OC particles are as below.

$$C_nH_{2m}O_p + (n-p)Me_xO_y \rightarrow nCO + mH_2 + (n-p)Me_xO_{y-1} \quad (12)$$

$$O_2 + 2Me_xO_{y-1} \rightarrow 2Me_xO_y \quad (13)$$

Unlike the CLC process, where the major goal is to get high fuel conversions in the FR through adequate oxygen delivery and solids circulation, total oxidation of fuel is undesired in CLG (Figure 9). The basic goal of CLG is to create high-quality syngas by partial oxidation of the fuel in the FR. Still, in CLG, part of the fuel must and will be oxidized to CO_2 and H_2O in addition to CO and H_2. Unlike indirect gasification, the inert bed material in CLG processes is replaced with OC particles. OC not only supplies a portion of the oxygen necessary for gasification, but it also serves as a heat carrier in the process, with the heat required in the gasifier generated by cyclic oxidation of reduced OC particles with air in the air reactor (AR). Fuel-air mixing is prevented when OC particles are used in an interconnected circulating fluidized bed (CFB) system, resulting in two independent gas streams, namely raw syngas from the fuel reactor (FR) with low nitrogen dilution and oxygen-depleted air from the AR Because it is devoid of gas pollutants, the ensuing oxygen-depleted air stream from the AR would ideally be cooled to ambient temperatures for heat recovery. In contrast to the IG process, most CO_2 in CLG is preferably limited to the FR, where it is accessible for carbon capture. The partial pressure of CO_2 would be higher in comparison to the IG process, while the amounts of diluents and tars would be smaller.

Chemical Looping with Oxygen Uncoupling

Lyngfelt and Mattisson offered an alternative to chemical-looping combustion in a patent application in 2005, which was eventually dubbed chemical-looping with oxygen uncoupling (CLOU). This novel technology enables the gas-phase oxygen combustion of solid fuels without the need for an energy-intensive air separation equipment. Carbon dioxide from combustion is naturally separated

from the rest of the flue gas. CLOU (Figure 8) is built on CLC, which consists of three processes carried out in two reactors. A metal oxide absorbs oxygen from the combustion air in the first stage, and then releases oxygen into the gas phase, where it combines with a fuel in the second (Mattisson et al., 2009). In contrast to CLC, the CLOU method necessitates the use of an oxygen carrier that emits gaseous O_2 in the fuel reactor, as seen in the diagram below (Li & Zhao, 2009).

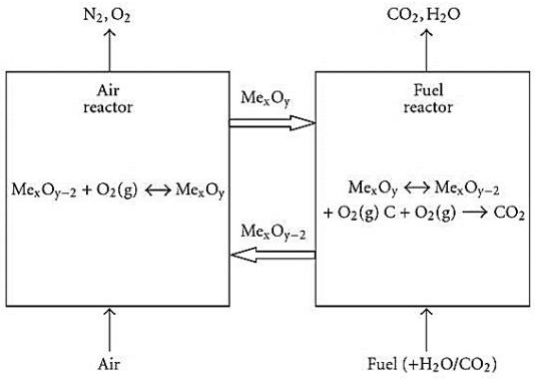

Figure 8. Diagram of CLOU (adapted from (Li & Zhao, 2009)).

Following that, fuel combustion happens in the fuel reactor in a homogeneous gaseous environment. The decreased oxygen carrier is then returned to the air reactor and re-oxidized. The overall reaction for the CLOU method is the same as for the CLC process and includes

hydrocarbon oxidation. Furthermore, CO_2 extraction from the gaseous product mixture formed during the CLOU process appears to be as simple as in chemical-looping combustion.

Chemical looping air separation (CLAS)

With a wide range of uses in industries such as metallurgy, glass manufacture, chemical synthesis, and health care, oxygen is the second-largest chemical produced by volume in the present global industrial market. At the moment, the most prevalent large-scale method for producing oxygen in the industry is cryogenic air separation, which has significant drawbacks such as high auxiliary energy use and high capital costs. Chemical Looping Air Separation (CLAS) (Figure 9), on the other hand, is a newer oxygen generating method that uses substantially less energy. With a 2 to 3.5 net percentage point better energy efficiency than cryogenic processes (Cormos, 2020), CLAS drew a lot of attention for its ability to overcome the constraints of traditional air separation systems.

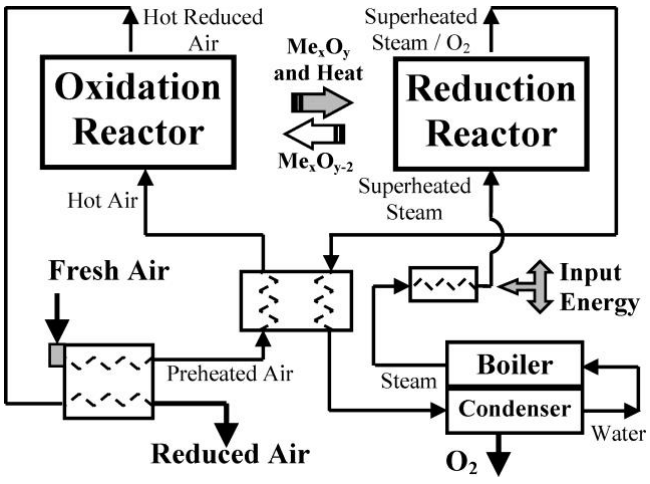

Figure 9. Diagram of CLOU (adapted from (Moghtaderi, 2010)).

CLAS is based on the same premise as CLC and combines the concept of oxygen decoupling into a two-step redox reaction mechanism:

Oxidation: $Me_xO_{y-2}(s) + O_2(g) \rightarrow Me_xO_y(s)$ (14)

Reduction $Me_xO_y(s) \rightarrow Me_xO_y(s) + O_2(g)$ (15)

Chemical Looping Dry Reforming (CLDR)

The Chemical looping dry reforming (CLDR) configuration aims to achieve profound oxygen carrier reduction in the first half-cycle to maximize CO_2 usage. It uses a bifunctional looping material that combines oxygen storage function for redox cycling with catalytic activity for effective fuel conversion. It produces syngas into two streams of CO and H_2 from the two reactors of the looping process (Yu et al., 2019). It is possible to employ CO_2 as an oxidant, leading to a novel method for effectively using CO_2 by reducing it to CO (Hu et al., 2018). In a fuel reactor (FR), CH_4 is first thermocatalytically cracked (Eq.16) over a metal catalyst to produce pure H2 and solid carbon. The deposited carbon is subsequently oxidized with CO_2 to CO in an oxidizing reactor (AR) via the Boudouard reaction (Eq. 17), yielding a high-purity CO stream and recycling the metal back to the fuel reactor. Because the metal transports carbon from one reactor to another, it is referred to as a "carbon carrier" instead of an "oxygen carrier" in a traditional Chemical looping process. The net reaction equals the DRM reaction (Eq. 18).

$C H_4 \rightarrow C + 2 H_2 \quad \Delta H^o = 75 KJ/mol$ (16)

$CO_2 + C \rightarrow 2CO \quad \Delta H^o = -171 KJ/mol$ (17)

$CH_4 + CO_2 \rightarrow 2CO + 2H_2 \quad \Delta H^o = 247.3 KJ/mol$ (18)

Advantages of CLRD over other Reforming techniques

CLDR outperforms SRM and DRM in terms of catalyst activity and lifetime, as well as the flexibility of discrete reaction steps and product streams that create segregated, high-purity CO and H_2 streams that allow combining syngas at any H_2/CO ratio required for downstream application. CLDR combines catalytic methane cracking with CO_2 activation, addressing some of the disadvantages of traditional methane cracking, such as low CH_4 conversion, quick catalyst degradation, and high-temperature excursions during carbon burn-off. Furthermore, it has inherent advantages. First, because the solid is regenerated in each cycle, accumulated carbon may be removed, and coking deactivation is prevented. Second, because the hydrogen produced in the first step is never in contact with the carbon dioxide, the RGWS reaction is suppressed, so syngas selectivity is optimized. On the other hand, the CLDR process, like SRM and DRM, is endothermic, requiring the combustion of more methane in a furnace for heat requirement. The O/C carrier plays a crucial role in controlling the heat of reaction in CLDR (Yu et al., 2019). Part of the heat can be balanced between the two reactors. The reactor's fluidization helps distribute the reaction's heat, thus preventing catalyst deactivation, coke deposition, the need for high endothermic heat, and the use of costly noble metal catalysts. For any chemical looping application, a collaboration between reaction engineering and particle science is essential to build the carriers, which should be used in conjunction with the system's reactor architecture. A comprehensive examination of reactor design encompasses crucial engineering features such as gas-solid fluxes, the usage of valves (mechanical and non-mechanical), and transport phenomena. Table 1 summarizes Advantages and challenges for the most used types of reactors for chemical looping applications (Cabello et al., 2023; Osman et al., 2021)

Table 1: Advantages and challenges for the most used types of reactors for chemical looping applications

REACTOR TYPE	ADVANTAGES	CHALLENGES
Moving Bed	• Higher fuel conversion than fluidized beds • Little OC attrition due to lower velocities • Easier to operate at high pressures because of low fluidization	• Large vessel size to have sufficient time for the low velocities • Larger particles create mass and heat transfer limitations
Packed Bed	• No circulation of solids • More compact design than fluidized bed • More suitable for pressurized operation • Extensive use in current industrial applications for syngas production	• High temperature valve switching system is required • Dynamic operation • Pressure drops for large columns
Fluidized Bed	• Mostly studied configuration for chemical looping. • Many configurations tackle the challenges but generate new ones • Pilot scale-demonstration projects	• Less preferred for pressurized operation due to the negative effect of gas density on fluidization • Solid circulation requires loop seals and cyclones • OC attrition from recirculation

2.1.4 Review of the Current CFD simulations and Pilot scale studies of CL Technology

Fluidization technology has many applications, including biomass gasification, chemical looping, and power production, due to its good mixing and high heat and mass transfer rates. Fluidization technology could be combined with chemical looping to understand gas hydrodynamics numerically and experimentally. Several reactor configurations have been developed and described in the review paper (Luo et al., 2018). Chemical-looping reactors could be configured in a variety of ways, such as a 120KW pilot scale dual fluidized bed gasification (DFBG) (Ge et al., 2015), a two-compartment fluidized bed reactor (CFB) (Pröll et al., 2010) (Thiemsakul et al., 2021) for CLC, a 900 W continuous atmospheric chemical looping reforming (CLF)(de Diego et al., 2009) with dual circulating reactors and a single loop seal gas analysis skid, coal-direct chemical looping combustion (CD-CLC) with dual interconnected reactors (Subhodeep & Ramesh, 2016), and a 10 kW Gas-Fueled Chemical Looping Combustion Unit (Sun et al., 2022).

The Vienna University of Technology has successfully built and run a 120 kW prototype plant for the CLR of natural gas (Pröll et al., 2010). The geometry design (Figure 10) consists of a steam-fluidized loop seals between the reactors, a cyclone separator, a variable cooling system, and two connected dual circulating fluidized beds (CFB) along with an AR and an FR make up the chemical looping unit (Kolbitsch et al., 2009). The two connected CFB reactors promise improved gas-solids contact and less solid inventory, but the complex geometry renders CFD simulation issues. The authors observed few challenges such as effective removal of dust and issues with high pressure operation of the system which can be understood better by performing 3-D numerical CFD simulating that reduces the cost of experimentation.

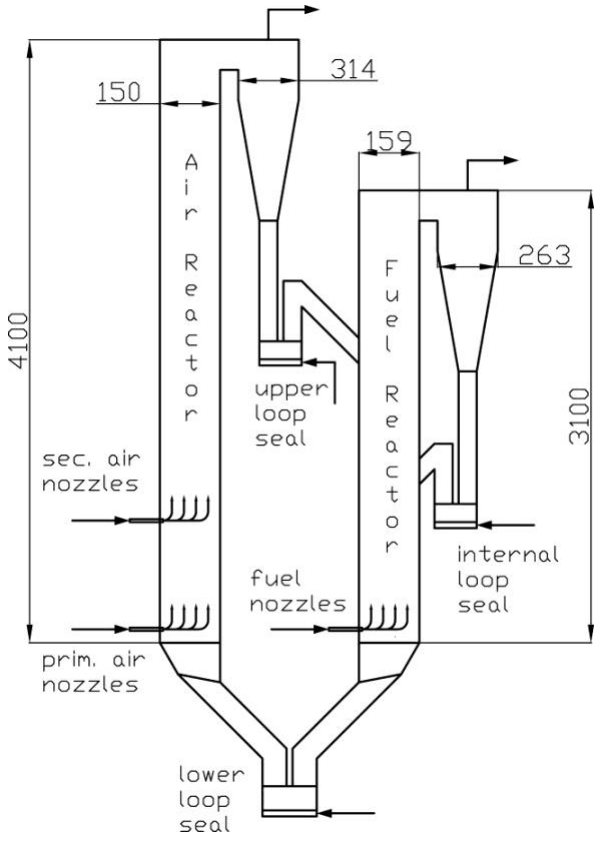

Figure 10. Sketch of 120 kW Chemical looping pilot plant (AR…air reactor, FR…fuel reactor)

Figure 11 presents a laboratory reactor design that includes AR, FR, downcomer, gas distributor and a wind box. A wind box is a chamber where air is initially injected, and it flows through the nozzles inside the gas distributor where the air is uniformly injected for fluidization. for a revolutionary combustion technology with inherent CO_2 separation at minimal cost and energy consumption for CO_2 collection. The reactor comprised two component fluidized beds—an air reactor and a fuel reactor—that were connected by a vertical wall connected with two different orifices. NiO, an oxygen carrier, circulated between the two reactors. The power range of the laboratory unit is 100-300 W, depending on the particle size and density of the oxygen carrier. The reactor's typical operating temperature is 950 ºC. Natural gas was altogether converted, and there was good selectivity for H_2 and CO. The authors (Kronberger et al., 2004) developed this compact pilot scale design considering the point that most of the other CLC reactors required large inventory oxygen carrier which affects the economics of operating the system. However, this design was constrained by the gas leakage problems, which may be solved by changing the slot layout and performing particle flow CFD numerical simulation to prevent the high cost of experimentation.

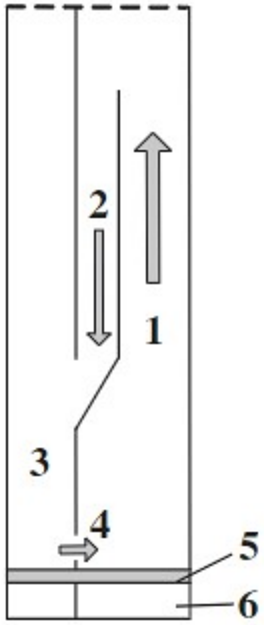

Figure 11. A fluidized bed with two components: 1 air reactor, 2 downcomers, 3 fuel reactors, 4 slots, 5 gas distributors, and 6 wind boxes.

Rydén et al. (Rydén et al., 2006) developed a continuous chemical-looping natural gas reforming in a laboratory reactor. The experimental findings from the 900 W continuous atmospheric CLR pilot plant were employed for the testing (de Diego et al., 2009). It has a sophisticated design (Figure 12), including two fluidized-bed reactors that were connected, a riser for moving solids from the air reactor to the fuel reactor, a solid valve for regulating the flow rate of solids supplied into the fuel reactor, a loop seal, a cyclone, and several flow control parameters. It resulted in an improved solid circulation flow rate, and the flow rate could also be controlled. Although designing and developing pilot plants uses a lot of expenditure, the initial expenditure cost could be saved with a numerical simulation. Numerical models such as CFD can be used in this work since the process's complex and microscopic behavior, particularly for three-dimensional structures, is poorly understood. In addition to offering thorough insights that cannot be obtained

through experimentation, CFD also enables the design of new reactors and the optimization of existing ones.

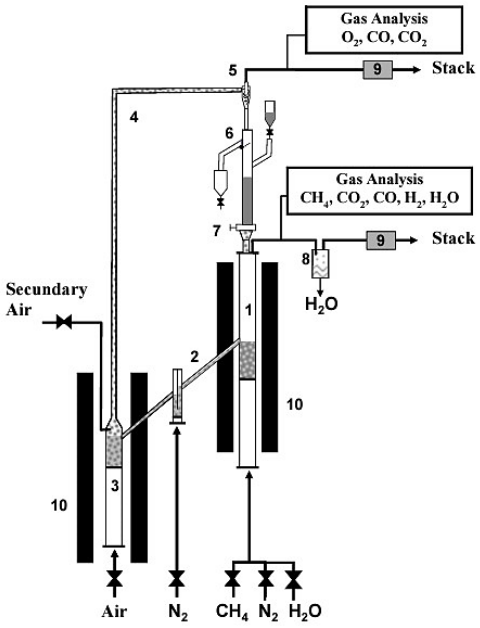

Figure 12. Schematics of a 900 W continuous atmospheric CLR pilot plant

Ge et al. (Subhodeep & Ramesh, 2016) examined how well a 25-kW CLC linked fluidized bed reactor produced syngas. The Eulerian technique was used to build a CFD simulation of a CLC reactor based on a dual fluidized bed reactor and to characterize the chemical reactions in the system. The two connected fluidized beds, an air reactor (25 x 25 mm), a fuel reactor (25 x 25 mm), a downcomer leaning against the wall, a water trap were attached to prevent leaks, pressure taps, and distributor plates made up the chemical-looping combustor (Figure 13). According to the authors, these pressure taps, a novel idea in this geometry, aid in avoiding de-fluidization in the system. Also, this study discovered that for CO_2 collection efficiencies above 90%, the marginal energy penalty associated with every subsequent rise in efficiency grows dramatically. This implies that the highest CO_2 efficiency achievable with calcium looping has a limit beyond which

the process becomes unfeasible owing to energy expenditure. Thus, certain experimental limitation to improve the efficiency requires a combination of Eulerian-Lagrangian CFD simulation along with chemical reaction to understand system kinetics.

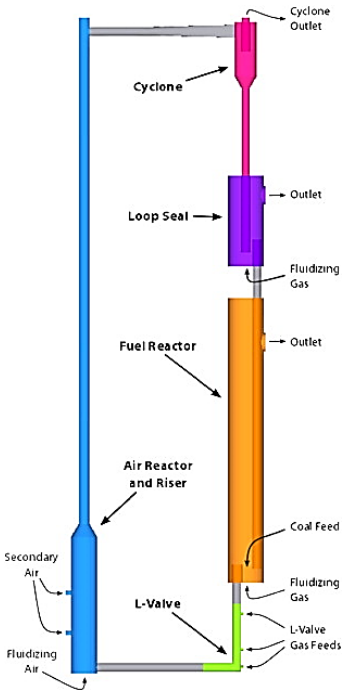

Figure 13. Schematics of a 25-kW CLC linked fluidized bed reactor.

Based on the research of Johansson et al. and Guann et al., (Sun et al., 2022) a gas-fueled chemical looping combustion unit (Figure 14) was numerically simulated. A dual-linked reactor, an air reactor, a fuel reactor, a cyclone, and a loop seal make up this system. To investigate the operation, a 3D model for a complete loop CLC system is constructed within the framework of the Eulerian-Eulerian method. The authors sought to calculate the oxidation level, which is possible through numerical simulation only. They also discovered that when the gas flow rate increases from 0.5 g/s to 1.0 g/s, the carbon capture efficiency declines from 0.54 to 0.2. The operating temperature is a critical parameter for the CLC.

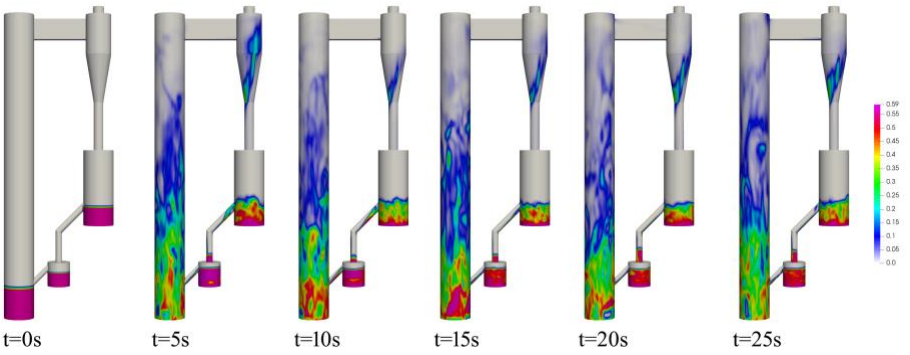

Figure 14. Flow pattern of solid phase in a Gas-Fueled Chemical Looping Combustion Unit.

CHAPTER 3: METHODOLOGY

Generally, two methods are used for simulation of multiphase flows containing solid particles. The Eulerian-Eulerian approach, also known as the two-fluid model (TFM), and the Eulerian-Lagrangian approach, known as CFD-DEM. In TFM, the kinetic theory of granular flows (KTGF) is utilized to implicitly describe particle-particle interaction. Conversely, in the CFD-DEM model, particle interactions are explicitly calculated using Newton's law by tracking each particle or parcel.

3.1 CFD-DEM

In this study, the Eulerian-Lagrangian approach (CFD-DEM model) was used to model the motion of solid particles and gas. This method combines two different frameworks: the Eulerian approach, which focuses on modeling the fluid flow, and the Lagrangian approach, which tracks the motion of individual particles. In the Eulerian framework, the fluid flow is modeled as a continuum, and the fluid properties, such as velocity, pressure, and density, are described by partial differential equations. This approach is suitable for modeling the behavior of the gas phase, but it cannot capture the individual motion of solid particles. In the Lagrangian framework, each particle is tracked as a discrete entity, and its position, velocity, and acceleration are described by ordinary differential equations. This approach is suitable for modeling the behavior of the solid phase, but it cannot capture the fluid dynamics of the gas phase.

In CFD-DEM, the two phases' governing equations are solved separately, or sequentially. Due to the possibility of different characteristic times, separate time steps are used for the CFD and DEM components, ensuring that the fluid flow is generally constant for several DEM (smaller) time steps. The Navier-Stokes and continuity equations are approximated locally to solve the fluid

phase flow. In this approach, the fluid motion is represented by solving Newton's second law equation based on the Euler framework. The gas flow is described by solving the Navier-Stokes equation considering volume fraction (Peng et al., 2015). Also, particle flow equations governing is based on the Eulerian-Lagrangian approach (Gu et al., 2018; Yang et al., 2019).

3.1.1 Equations governing the Eulerian-Lagrangian approach (CFD-DEM model)

3.1.1.1 Equations of Mass and Momentum Balance

The equations for continuity and momentum conservation are expressed as follows

$$\frac{\delta(\varphi_g \rho_g)}{\delta t} + \nabla.\left(\varphi_g \rho_g \overrightarrow{v_g}\right) = 0 \tag{19}$$

$$\frac{\delta(\varphi_g \rho_g \overrightarrow{v_g})}{\delta t} + \nabla.\left(\varphi_g \rho_g \overrightarrow{v_g}\overrightarrow{v_g}\right) = -\varphi_g \nabla p + \nabla\left(\varphi_f \overline{\overline{\tau_g}}\right) + \varphi_g \rho_g \vec{g} + \overrightarrow{F_{DEM}} \tag{20}$$

Where $\overline{\overline{\tau_g}}$ is the stress tensor, g is the gravitational acceleration, φ_g is the gas phase volume fraction, p is static pressure, $\overrightarrow{v_g}$ is the velocity vector, ρ_g is the gas density, φ_f is the fluid phase volume fration and F_{DEM} is the external force produced by all the moving particles that act on the infinitesimal fluid element (e.g., the force generated due to the interaction of the liquid phase with the discrete phase). The fluid phase's conservation of mass and momentum can also be applied to the dispersed phase. The fluid viscous stress tensor ($\overline{\overline{\tau_g}}$) can be modeled as

$$\overline{\overline{\tau_g}} = \left(\mu_g + \mu_t\right)\left\{\left[\nabla v_g + \left(\nabla v_g\right)^T\right] - \frac{2}{3}\left(\nabla . v_g\right)\overline{\overline{I}}\right\} \tag{21}$$

where μ_g is the gas dynamic viscosity, μ_t is the turbulent viscosity, and $\overline{\overline{I}}$ is the unit I tensor.

3.1.1.2 k- ϵ Turbulence Models

In this study, the default multiphase turbulence model is mixed turbulence. It is applicable when phases separate, for stratified (or nearly stratified) multiphase flows, and when the density ratio between phases is close to 1. It is the first extension of the single-phase k-model. In these circumstances, capturing significant aspects of the turbulent flow using a mixture of characteristics and velocities is sufficient. The standard k- ϵ turbulence model was used in CLDR with high solid concentrations to simulate the turbulent flow in the reactor (Cheng et al., 2003).

$$\mu_t = C_\mu \rho_g k^2/\varepsilon \tag{22}$$

Where C_μ is turbulence model constant

The k (turbulent energy) and ϵ (turbulent dissipation rate) equations are defined as follows:

$$\frac{\delta(\rho_g k)}{\delta t} + \nabla.\left(\varepsilon\rho_g\overrightarrow{v_g}k\right) = \nabla.\left[\sigma\left(\frac{\mu_t}{\epsilon_k}+\mu\right)\nabla k\right] + \epsilon G_k - \sigma\rho_m\epsilon_k + S_d^k \tag{23}$$

$$\frac{\delta(\rho_m \epsilon)}{\delta t} + \nabla.\left(\varepsilon\rho_g\overrightarrow{v_g}\epsilon\right) = \nabla.\left[\sigma\left(\frac{\mu_t}{\epsilon_k}+\mu\right)\nabla \epsilon\right] + \sigma\frac{\epsilon}{k}(C_{1\epsilon}G_k - C_{2\epsilon}\rho_g\epsilon) + S_d^\epsilon \tag{24}$$

where the mixture density ρ_m and velocity $\overrightarrow{v_m}$, are computed from.

The impact of the particle on the fluid is determined by S_d^k and S_d^ϵ, which are computed according to equations 10 and 11, respectively.

$$S_d^k = \beta\left|\overrightarrow{v_g} - \overrightarrow{v_p}\right|^2 + \beta\left(\Delta v_p\,\Delta v_p - \Delta v_g\,\Delta v_p\right) \tag{25}$$

$$S_d^\epsilon = C_3\frac{\epsilon_\epsilon}{k}S_d^k \tag{26}$$

$\beta\left|\overrightarrow{v_g} - \overrightarrow{v_p}\right|^2$ refers to the generation term resulting from particle resistance, while $\overrightarrow{v_p}$ represents the average velocity of particles in a given volume. The redistribution term, $\beta\left(\Delta v_p\,\Delta v_p - \Delta v_g\,\Delta v_p\right)$, denotes the transfer of kinetic energy velocity between the gas and particle. Specifically,

it accounts for the exchange of energy velocity between the gas fluctuating velocity, Δv_g, and the particle fluctuating velocity, Δv_p.

$$\beta\left(\Delta v_p \Delta v_p - \Delta v_g \Delta v_p\right) = -2\beta k\left(1 - \frac{\tau_I}{\tau_I+\tau_d}\right)\frac{\tau_I}{\tau_I+\tau_d} \quad (27)$$

τ_I represents the time scale of the Lagrangian for the gas phase, while τ_d denotes the time scale of response for the particle phase.

3.1.1.3 Drag Model

β is the inter–phase momentum exchange coefficient. Syamlal-O'Brien has been presented in this study to show the inter-phase momentum exchange between phases in a gas-solid bubbling fluidized bed. Different drag models are available, such as Wen-Yu, Syamal-O'Brien, and Gidaspow. Syamal-O'Brien has gained widespread acceptance and is used in the commercial-scale simulation of fluidized beds (Zhou et al., 2017). The Gidaspow model for the exchange coefficientβ_{sg} is given by

$$\beta_{sg} = \frac{\frac{150\,\varphi_s^2}{\varphi_g}\mu_g}{d_p^2} + 1.75\,\varphi_s\frac{\rho_g}{d_p}|\overrightarrow{v_g}\,\overrightarrow{v_s}| \quad \text{for } \varphi_g \le 0.8 \quad (28)$$

$$\beta_{sg} = 0.75|\overrightarrow{v_g}\,\overrightarrow{v_s}|\,\varphi_g\rho_g C_{D0}\varepsilon_g^{\left(-2.65\left(\frac{1-\varphi_g}{d_p}\right)\right)} \quad \text{for } \varphi_g \ge 0.8 \quad (29)$$

Where C_{D0} is the standard drag coefficient

$C_{D0} = 0.44$, for $Re_p > 1000$

$C_{D0} = 24/Re_p((1+0.15Re_p^{0.687}))$, $Re_p \le 1000$

With $Re_p = \rho_g\frac{d_p(v_g-v_p)\,\varphi_g}{\mu_g}$ (30)

3.1.1.5 Equation of Motion of particles and fluid

The forces acting on the particles usually include the contact force, the fluid drag force, the pressure gradient force, and the gravity force. The following equations are solved to determine the translational and rotational motion of each particle in the system:

$$m_i \frac{dv_i}{dt} = \sum_{j=1}^{Nc} F_{c,ij} + F_{h,i} + F_{g,i} + F_{k,i} \quad (31)$$

$$I_i \frac{d\omega_i}{dt} = \sum_{j=1}^{Nc} (T_{c,ij} + T_{r,ij}) + T_{fp,i} \quad (32)$$

Where the i-th particle's mass, velocity, moment of inertia, and angular velocity are, respectively, m_i, v_i, I_i, and ω_i, the total hydrodynamic force (i.e., drag + pressure gradient) $F_{h,i}$, gravity $F_{g,i}$, and cohesive/adhesive forces $F_{k,i}$ are included in the list of external actions that have contact forces $\sum_{j=1}^{Nc} F_{c,ij}$. Different models, such as van der Waals, capillary bridge, and electrostatic effects, can be included thanks to the cohesive forces.

The total of all torque contributions produced in the rotational direction by non-collinear collisions $T_{c,ij}$, the corresponding rolling friction torque $T_{r,ij}$, and the fluid-particle torque T_{fp}, added together.

3.1.1.6 Contact Models

The linear spring-dashpot-slider model is used to calculate the contact force (Zhou et al., 2017), and its expressions for the regular and tangential components are

$$F_{c,ij}^{n} = -K_n \delta_{n,ij} - \eta_\eta v_{n,ij} \quad (33)$$

$$F_{c,ij}^{t} = -\min\left(\mu F_{c,ij}^{n}, K_t \delta_{t,ij} + \eta_t v_{t,ij}\right) \quad (34)$$

Where the δ's stands for the (average, sub n, and tangential, sub t) displacements between the contacting particles, the ν stands for their relative velocity components at the contact point, the K stands for the spring stiffness constants, η the dashpot damping coefficient, and μ slider friction.

Also, it is to be noted that Coulomb's sliding limit caps the tangential contribution of the force in magnitude by:

$$F_{ct} \leq \mu F_{cn} \tag{35}$$

The impending associated energy is dissipated as friction force.

The relation between the coefficient of restitution e_n and the damping coefficient η_n is given by:

$$\eta_\eta = (-2\ln e_n \sqrt{m * K_n}) / \sqrt{(\ln e_n)^2 + \Pi^2} \tag{36}$$

Hertz-Mindlin theory, which ignores micro-slip on the contacting surfaces (no-slip approximation), provides a more accurate representation of the interparticle contact (Richesson & Sahimi, 2019). These parameters can be compared to those of their linear counterpart.

In this study, the following formulas are used for the contact model:

$$K_n = \frac{4}{3} E_{eq} \sqrt{R_{eq}}\, \delta_n \tag{37}$$

$$K_t = \kappa K_n \tag{38}$$

$$\kappa = K_t / K_n = \frac{\left[\left(1-\frac{\nu_1}{G_1}\right) + \left(1-\frac{\nu_2}{G_2}\right)\right]}{(1-1/2\nu_1)/G_1 + (1-1/2\nu_2)/G_2} \tag{39}$$

When particles of various materials or sizes are considered, and the equivalent properties, E_{eq}, and R_{eq}, are used. It is convenient to express the forces as

$$F_n = -K_n \delta_n - \eta_\eta^H \nu_g \tag{40}$$

$$F_t = -K_t \delta_t - \eta_t^H \nu_t \tag{41}$$

The parameters η_η^H an η_t^H, which are connected to the corresponding restitution coefficients, e_n and e_t, respectively, determine the velocity-dependent dissipative terms, according to

$$\eta_{\eta}^{H} = \frac{-\sqrt{5}\,\mathrm{lne_n}\sqrt{m*K_n}}{\sqrt{(\mathrm{lne_n})^2+\Pi^2}} \quad (42)$$

$$\eta_{t}^{H} = \frac{-\sqrt{\frac{10}{3}}\,\mathrm{lne_n}\sqrt{m*K_t}}{\sqrt{(\mathrm{lne_n})^2+\Pi^2}} \quad (43)$$

The computational model was created by The National Energy Technology Laboratory's (NETL's) computational fluid dynamics (CFD) code, MFiX 22.4 —Multiphase Flow with Interphase eXchanges, while the geometry has been created in ANSYS.

3.2 Reactor Design and its Working

The design Figure 15 in this study consists of a dual-circulating fluidized bed reactor. The particle circulation starts in an Air Reactor (AR) with an inlet diameter of 80 mm, which imparts high fluidization velocity to the particles. The particle then flows through a high-velocity riser with an inlet diameter of 35 mm. In a high-velocity riser, the velocity increases exponentially to impart sufficient momentum interaction among the particles to enter the fuel reactor (FR) with adequate energy. The flow then passes through a pipe bend which directs the flow towards the cyclone distributor (CD) through a tubing of length 300 mm. Cyclone distributor (CD) is an assembly that solves the purpose of removing particulate matter between fluid and solids. This cyclone distributor consists of a feed inlet (FI), overflow tube (OT), vortex forcer (VF), cylindrical section, conical section, and an atmospheric gas pressure outlet (25 mm). The cyclone separator works on the principle of vortex separation by imparting rotational energy to the solid, which enters through the feed inlet (FI), further strikes the cylindrical wall, and falls under the influence of gravitational forces. The vortex finder (VF) provides a passage for the particles to flow through it. Under gravity, the falling particles enter the FR with a diameter of 90 mm, a fluidized bed reactor. The

fluidized bed reactor (FBR) is a reactor, where the solids are suspended to act as a fluid with a minimum fluidization velocity. The geometrical design Figure 16 of AR and FR can be similar or different, but AR always works on the high fluidization regimes while FR is a bubbling column (Li & Shen, 2021). The fluidizing particles in the fuel reactor keep fine particles under fluidization and provide a path to enter through the loop connection. The fuel reactor has a pressure relief outlet with a diameter of 20 mm, which is open to the atmosphere. The loop seal connection with a diameter of 30 mm plays a key role in this reactor assembly. It helps maintain pressure balance between AR and FR and prevents severe backflow of particles from AR, which works on higher velocity. The particles from the FR are transferred to the AR by the loop connection to normalize the reactor's pressure. The cycle continues, and a part of only 10-15% of particles is prone to keep circulating between the reactors.

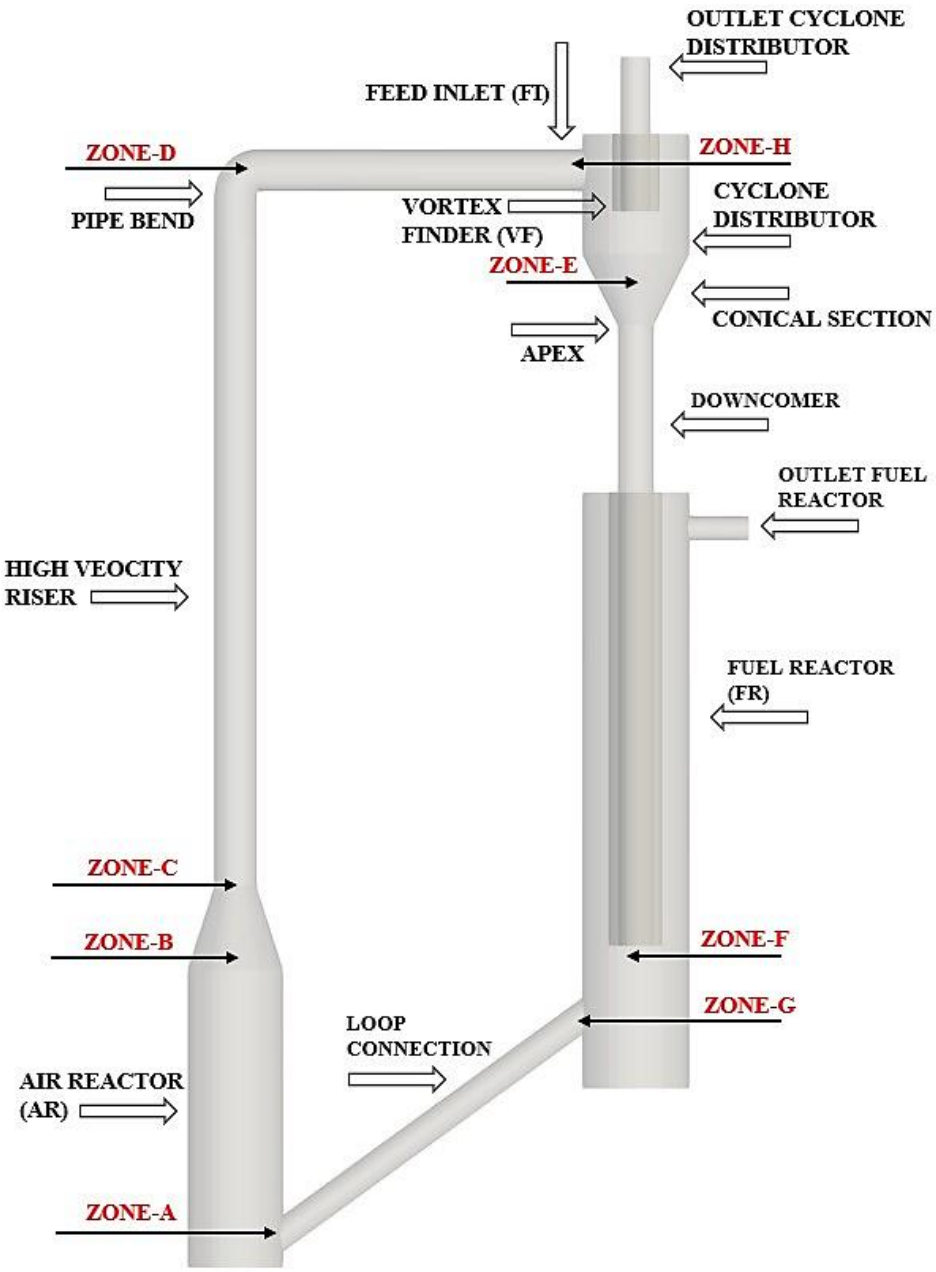

Figure 15. Reactor design with labeled sections and zones used for data analysis

Table 2: Geometrical Parameters

Parameter	**Air Reactor**	**High velocity riser**	**Pipe bend**	**Cyclone Distributor**	**Fuel Reactor**	**Loop Connection**	**Unit**
Diameter of air reactor inlet	80						mm
Height of the air reactor	250						mm
Height of convergence Zone	70						mm
Diameter of the riser tube		35					mm
Length of the riser tube		535					mm
Length of the bend to Feed inlet			300				mm
Diameter of the bend to Feed inlet			35				mm
Diameter of the cylindrical section				90			mm
Length of the cylindrical section				100			mm
Diameter of vortex finder				40			mm
Diameter of overflow tube				25			mm
Length of overflow tube				130			mm
Diameter of inverted conical outlet				30			mm
Length of the FR					500		mm
Diameter of fuel reactor					90		mm
Diameter of FR outlet					20		mm
Length of loop connection						350	mm
Diameter of loop connection						30	mm
Angle of loop connection						36^{o}	Degree

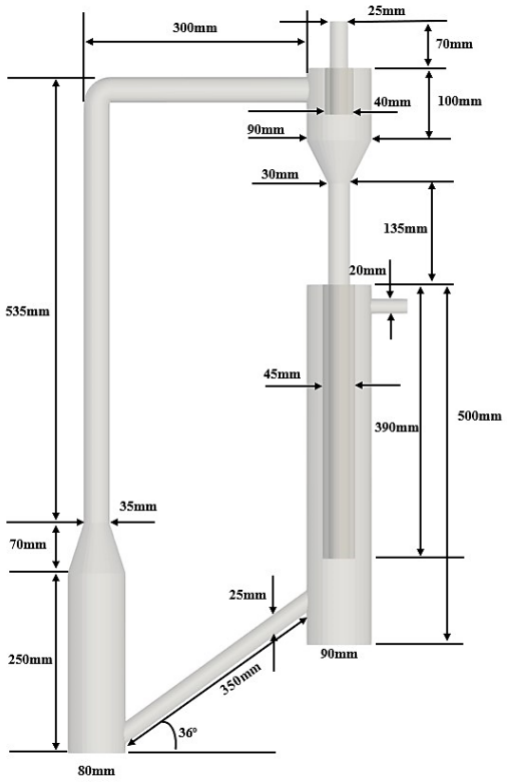

Figure 16. Geometric design and sectional dimensions.

Table 3: Mesh parameters and Conditions

Mesh Condition	**X**	**Y**	**Z**	**Unit**
Cell	64	144	13	
Cell size	$6.98x10^{-3}$	$6.99x10^{-3}$	$7.08x10^{-3}$	meter
Mesh Parameters				
Mesh Type	Quadrilateral			
Small Cell tolerance	0.01			Fraction
Facet angle tolerance	0.01			Fraction
Dot product tolerance	0.001			Fraction
Max facets per cell	40			

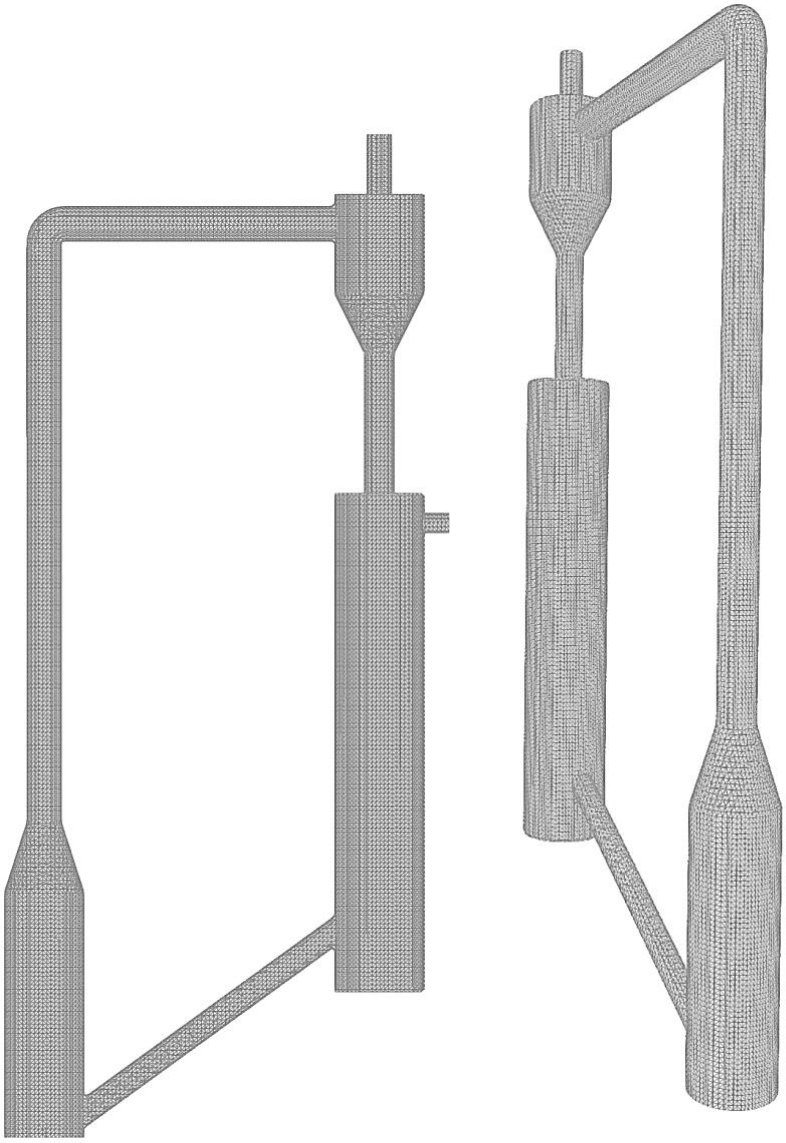

Figure 17. Quadrilateral meshing as viewed from the front.

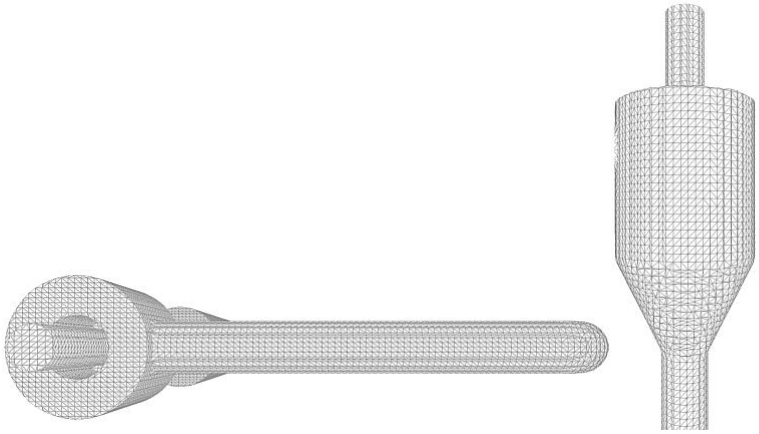

Figure 18. Quadrilateral meshing as viewed from the top and front (cyclone distributor).

Table 4: Simulation Parameters

Parameters	**Value or setting**	**Unit**
Turbulence Model	K- ε model	
Drag model	Syamal-O'Brien	
Gas density	1.225	Kg/m^3
Gas viscosity	1.8×10^{-5}	Pa. s
Avg. diam. of particles	3	mm
Avg. density of particles	2400	$kg\ m^{-3}$
Total number of particles Air Reactor	35424	
Total number of particles Fuel Reactor	20700	
Total number of particles bend loop	12304	
Collision Model	Linear Spring	
Two-way particle-fluid coupling	Dashpot	
Coulomb friction coefficient Particle - Particle	Fully Coupled	
Coulomb friction coefficient Particle – wall	0.1	
Normal spring constant	0.1	
Normal restitution coefficient for inter-particle collisions	0.9	N/m
Normal restitution coefficient for particle-wall collisions	0.9	N/m
Maximum Iteration	50	
Spatial Discretization Scheme	First order upwind	
Under relaxation pressure	0.8	
Under relaxation volume fraction	0.5	
Under relaxation momentum	0.5	
Nusselt number correlation	RANZ	
Simulation time	8.5-12	hours
Maximum time step size	25	Sec
Initial time step size	1.0000e-03	Sec

3.3 Boundary Conditions

The boundary conditions Table 6 assigned to the zones in this study is based on fluid-solid interaction. Air reactor is assigned a variable velocity ranging from 2.5 m/sec to 4 m/sec to analyze the optimum velocity value required for high velocity zone. Fuel reactor is assigned a minimum fluidization mass flow rate ranging from 0.001 Kg/sec to 0.005 Kg/sec to understand the impact of higher fluidization velocity on the chemical looping efficiency. The chemical loop circulated the particles with the outlets being under atmospheric condition with pressure equal to 1 atm. The

boundary condition for the wall is stated as a no-slip wall. An impermeable wall with a no-slip condition states that the tangential velocity vector is equal to the speed of the wall. While the condition for the normal velocity component is zero. This indicates that impermeable wall requires a zero-flow condition in the field of the normal direction.

Table 5: Initial Conditions

Region	Type	Value or setting
Air Reactor bed	Volume fraction - Solid	0.5
Fuel Rector bed	Volume fraction - Solid	0.5
Center Loop connection	Volume fraction - Solid	0.5

Table 6: Boundary Conditions

Region	**Type**	**Value or setting**	**Unit**
Inlet Air Reactor	Velocity	2.5 - 3.5	m/sec
Inlet Fuel Reactor	Mass inflow	0.001 - 0.1	Kg/sec
Cyclone Outlet	Pressure Outflow	$1.0132e^{+05}$	Pa
Fuel reactor Outlet	Pressure Outflow	$1.0132e^{+05}$	Pa
Wall	No- slip wall		

3.4 Simplification Assumption

Particle shape: The accurate incorporation of particle shape within Discrete Element Method (DEM) models is of paramount importance, as it enables the simulation of a wide range of flow features with greater precision than when using circular particles exclusively (Li et al., 2023). The inclusion of various particle shapes significantly impacts the flow pattern, flow rates, particle distribution, and inter-particle cohesion in distinct ways. It should be noted that particle interaction can result in breakage (Yang & Wang, 2020), which was not considered in this study. For the purpose of this analysis, the particles were assumed to have a uniform spherical shape by default.

However, it is important to acknowledge that real-world granular flows often consist of particles with non-uniform shapes, and therefore, further investigations are necessary to determine the effects of particle shape on the accuracy of DEM simulations.

Particle size: The Discrete Element Method (DEM) is a numerical tool that has been widely employed in simulating granular flow. Due to the large number of particles that are typically present in such flows, these simulations can be computationally intensive. In order to reduce the computational costs, models that employ a limited number of particle sizes are often used to determine the gas-solid hydrodynamics (J. Bandara et al., 2020). However, the use of such simplified models can compromise the accuracy of the simulation results. Therefore, it is necessary to thoroughly investigate the effects of particle size distribution on the accuracy of granular simulations. In the present study, a particle size range of 3-3.5 mm was chosen as a simplification in order to reduce the computational complexity of the simulation. However, it should be noted that this simplification may not fully represent the particle size distribution in real-world granular flows. Therefore, further studies that consider a wider range of particle sizes are needed to fully understand the effects of particle size distribution on the accuracy of granular simulation (J. Bandara et al., 2020).

Air as an injection fluid medium: For the purposes of simplification, air is employed as the fluid medium in this study, despite the injection of CO2 and CH4 in the oxidizer and reducer sections, respectively. The choice of fluid has a significant impact on the hydrodynamics of the system, as different fluids possess unique properties such as density, viscosity, temperature, pressure, specific volume, specific weight, specific gravity, and surface tension. The use of specific fluids is particularly important when applying energy equations to the system. In this study, air is used as a fluid medium, which follows the ideal gas law and has a viscosity value of 1.8*10-5 Kg/m3 and

a molecular weight of 29 Kg/kmol. While this simplification may not fully represent the real-world scenario, it allows for a more computationally efficient simulation, as the properties of air are well-understood and widely available.

CHAPTER 4: RESULTS AND DISCUSSIONS

4.1 Chemical looping flow pattern

Fig. 5a shows a typical particle flow pattern in a chemical looping reactor (CLR) (Gu et al., 2018); between time interval t=8.20 sec to t=12.85 sec. Overall, the solid particles are circulated between the fuel reactor and the air reactor through a periodic pulse flow, which causes the particles to move in a pulsating manner. Different types of fluidization (Li et al., 2023) are observed in separate geometrical section as explained in next sections. After reaching system stabilization, every cycle (or pulse) starts from the FR. The particles enter the FR through the downcomer (Figure 19a-1). At the same time, the excess particles begin to enter the loop connection because of the improved gas-solids hydrodynamics (Yang & Wang, 2020), which means the system has reached pressure stabilizing state. This prevents the accumulation of particles in FR. Meanwhile, particles are continuously transferred to the AR through the loop seal. However, the flow rate of the particles entering is larger than that leaving the loop seal. As a result, loop seal is ultimately filled up with particles (Figure 19a-4). Figure 19b shows the corresponding pressure contours of particle flow simulation through the chemical loop in every step. The pressure is dependent on the volume fraction of solids flowing through the system and the fluidization velocity injected in AR and FR, which is discussed in further section of the results. It is observed that once the loopseal is completely filled with particles, the pressure difference between the FR and AR reaches the maximum value (Figure 19b-3). At this moment, the AR undergoes a fluidization and pressure change during which the high velocity of fluidization injected into the AR causes sufficient volume fraction of solids to flow from the AR into the riser tube. Simultaneously, a sudden reaction in AR pressure happens. The particles then flow into the cyclone distributor, interacting with the cylindrical wall and then start to fall under the influence of gravity into the FR downcomer (Figure

19a-6). The flow pattern repeats again as the concentration of particles increase again in the fuel reactor due to particles entering the AR

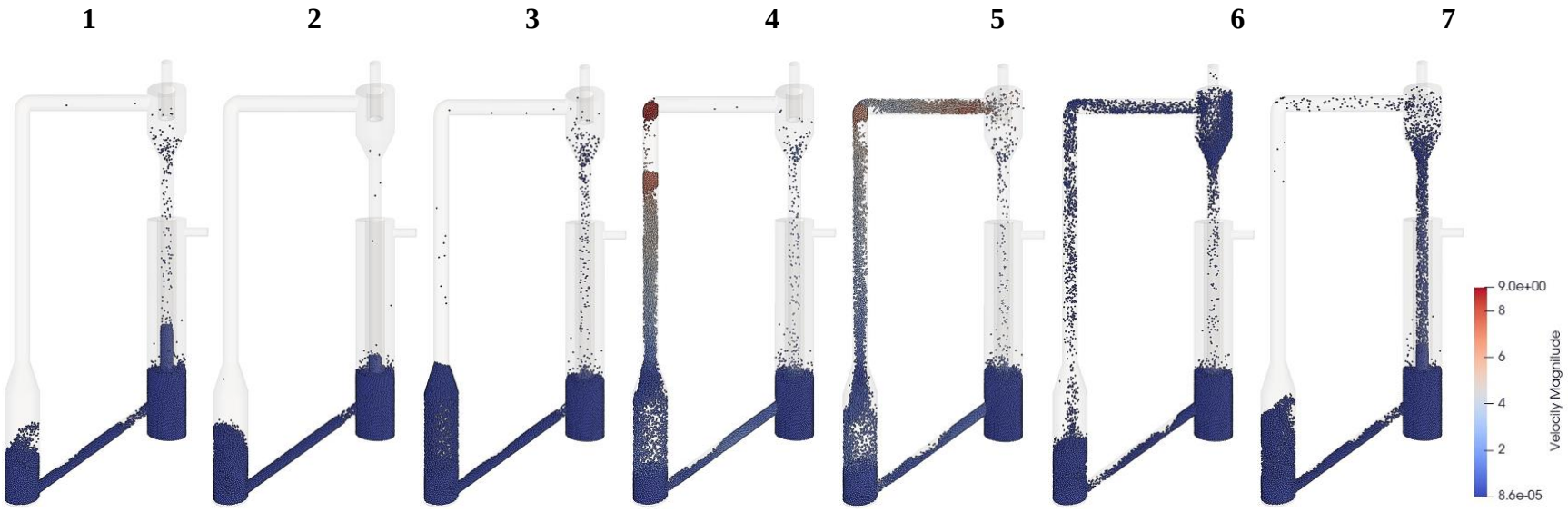

(a) t=8.20 sec t=9.20 sec t=12.15 sec t=12.26 sec t=12.31 sec t=12.44 sec t=12.85 sec

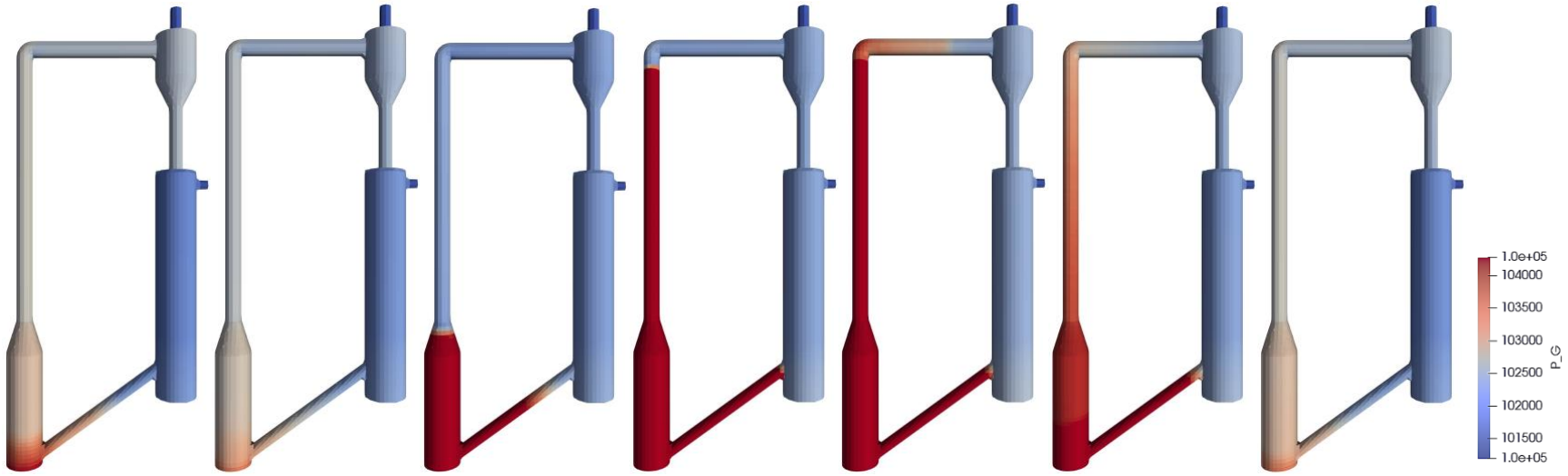

(b) t=8.20 sec t=9.20 sec t=12.15 sec t=12.26 sec t=12.31 sec t=12.44 sec t=12.85 sec

Figure 19. Circulation of catalytic solid particles between FR. (right) and AR (left) a) Particles velocity magnitude, b) Pressure in AR and riser. Simulation condition: V.AR: 3.2 m/sec, V_{FR}: 0.0025 kg/sec, Volume fraction of solid inside LC/AR/FR: 0.5

4.2 Flow pattern in the fuel reactor

The analysis of the flow pattern in the fuel reactor is critical to determine the transfer of particles flowing through the connection loop back into the air reactor. Figure 20 shows the particle flow pattern (in terms of vectors and particles volume fraction) at the time intervals of 3.3 to 4 sec and 6.8 to 7.4 sec, at gas inlet mass flow rate: 0.0025 Kg/sec in FR and gas inlet velocity 3.2 m/sec in AR The corresponding pressure contours are depicted in Figure 21. These time intervals are referred to the two major pressure peaks highlighted in Fig. 8, which gain insights into the fluid flow pattern at the moments of particle circulations. All explanations are based on the zones, which have been introduced in Figure 15. Only region F, which is in the fuel reactor is discussed here.

First, the initial bed height in FR was 105 mm, which increased to 141 mm upon gas injection and fluidization. The bed height was further enhanced to 157~161 mm in every cycle of particle circulation and their return to the FA. The increase of bed height at the period of circulation compared to the typical fluidization is due to the larger number of particles entering through the downcomer compared to the lower number of particles leaving the FR through the loop connect.
In a typical flow in the FR under the steady state condition (after stabilization), the particles move around freely and collide with each other and the bed surface. The velocity vectors in this region are typically pointing upward (Figure 20a, t: 3.63 sec) and downward (Figure 20a, t: 7.4 sec) or a combination of these two (Figure 20a, t: 3.62 sec), and are relatively uniform. Meanwhile, the particles gradually enter the loop connect (as highlighted in blue in Figure 20a, t: 3.3 and 7.4 sec). It can be observed that the vectors are toward the loop connect at the vicinity of the loop connect

inlet and the pressure difference between the AR and FR is around 1864 Pa at the steady state condition. However, every cycle of solid particle circulation and the exact moment of particles jump up at the AR affects the fluid flow pattern in the FR. Eliminating the first 2 secs during which the CL reactor stabilizes, the first main particles circulation happens at ~ 3.6 sec, which is slightly weaker than the second one at ~ 7 sec. As observed in Figure 20a, a backflow happens at t: 3.63 sec from the loop connect to the AR In this study, backflow refers to the flow of solid particles in the direction opposite to the intended direction of flow; (from the loop connected to the AR). Therefore, all the vectors show a reversed direction as highlighted by the red dashed oval in Figure 20a; at the velocity of 0.04 m/sec, which is higher than the typical velocity of the particles in AR at the steady state condition (Figure 20b, t: 3.62 and 3.63 sec). A similar behavior is observed during the second cycle of the solid particles (Figure 20a and b, t: 6.99). This phenomenon occurs in less than 10 msec, after which the flow pattern is stabilized in AR and the bed height is slightly reduced. Backflow occurs due to the unbalanced pressure between the AR and FR at the time of particle jump, which will be explained in detail in the next section. Although, the pressure value remained almost constant in the FR according to the pressure contours in Figure 21, closer attention to Figure 22 shows that a small pressure increase (~102385 Pa) occurs in FR at the moments of the particle's circulation (Zone F, blue color). This slight pressure increase is more visible for the second peak. Figure 23shows the volume fraction of solid particles at zones F (in FR close to the downcomer) and zone G (loop connect inlet). As observed, solid particles fill up around 60% of the FR. The value does not change significantly either during the particle’s circulation not at the steady state condition. However, the volume fraction at a certain time step is as low as 0.04 which confirms that the connection is filling up and it is not fully filled for the entire time interval.

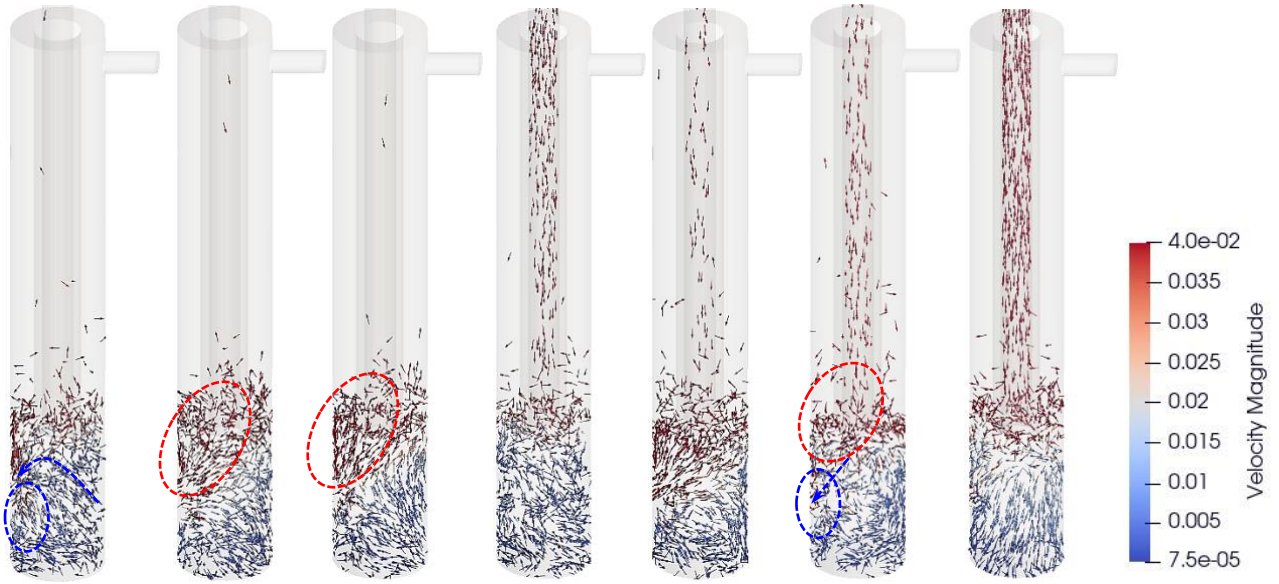

(a)

(b)

Figure 20. Circulation of catalytic solid particles inside FR. a) Velocity vectors magnitude, b) Particle velocity magnitude. Simulation condition: V_{AR}: 3.2 m/sec, V_{FR}: 0.0025 kg/sec, Volume fraction of solid inside LC/AR/FR: 0.5

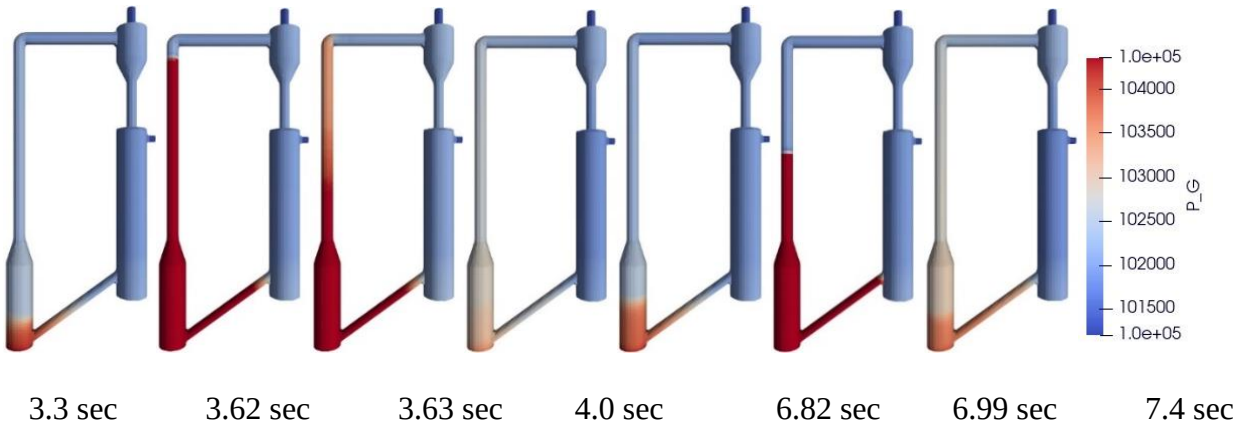

Figure 21. Pressure contours in chemical loop during time interval of 3.3-7.4 sec. Simulation condition: V_{AR}: 3.2 m/sec, V_{FR}: 0.0025 kg/sec, Volume fraction of solid inside LC/AR/FR: 0.5

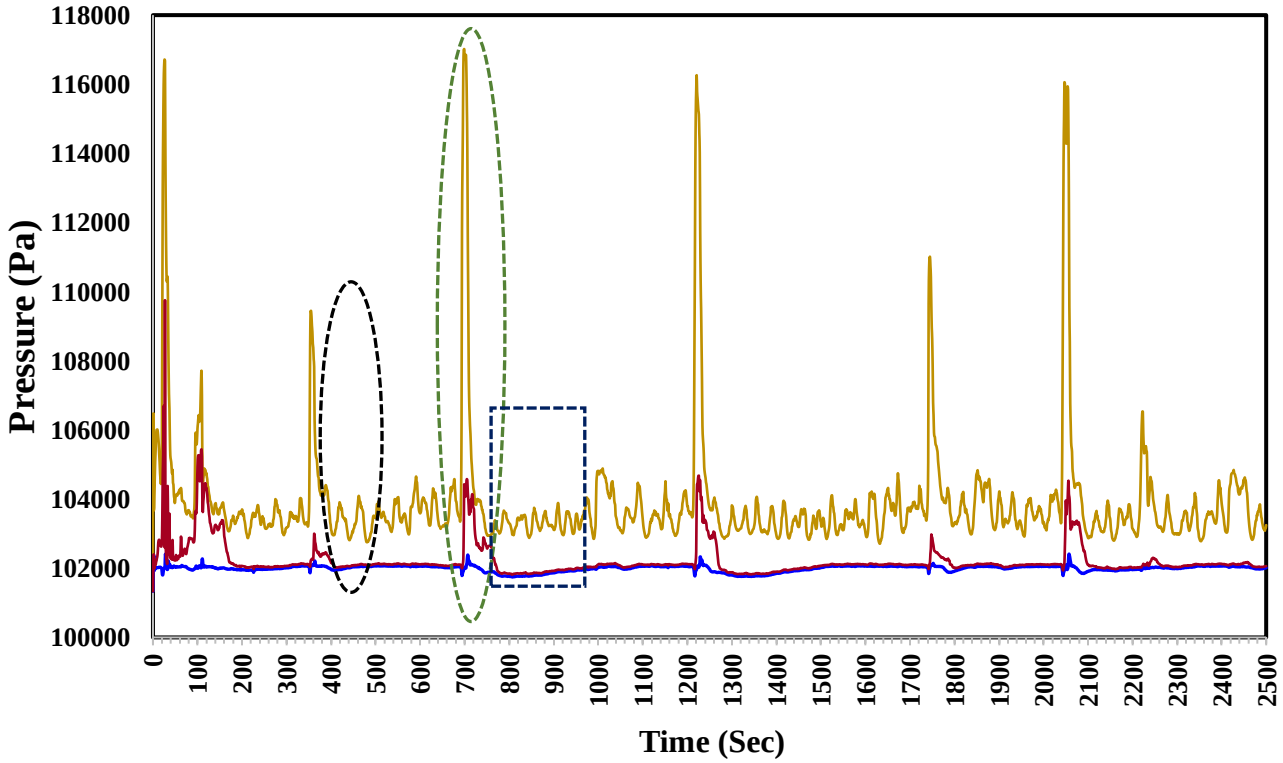

Figure 22. The graph between Pressure and time for — Avg (P_G) ZONE-F**,** — Avg (P_G) ZONE-G — and Avg (P_G) ZONE-A for time intervals 0-25seconds.

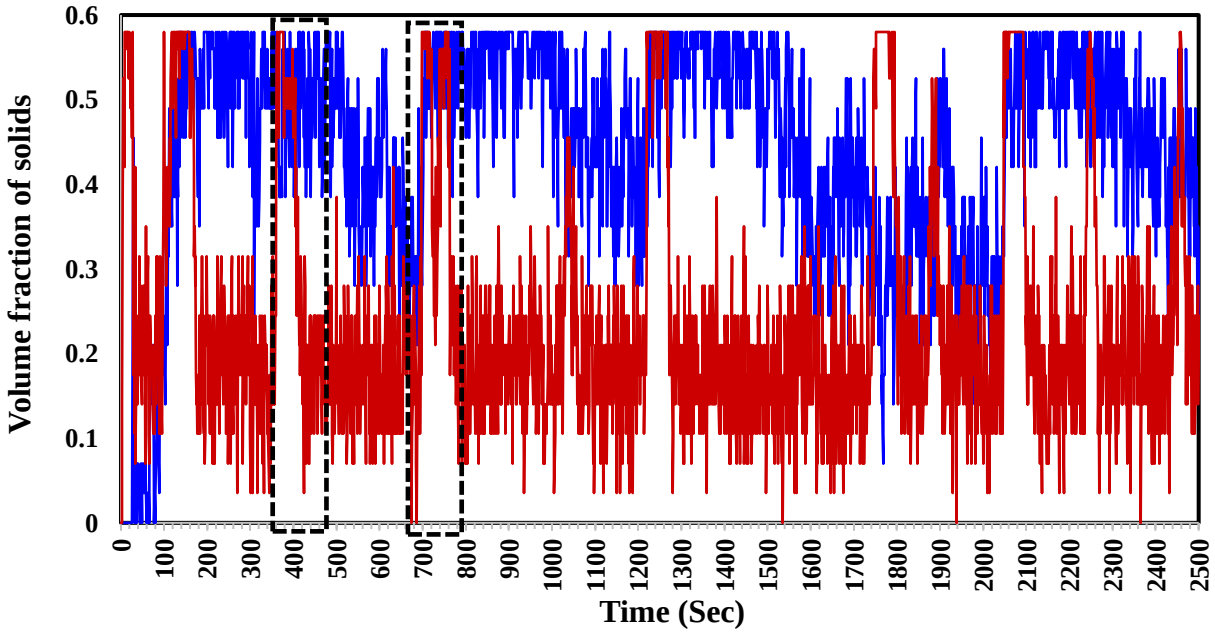

Figure 23. The graph between Volume fraction of Solids and time for ▬ Avg (EP_S) ZONE-F and ▬ Avg (EP_S) ZONE-G between time intervals 0-25 second

4.3 Flow pattern in Connection loop

4.3.1 Filling up of connection loop

The loop connection plays a critical role in balancing pressure between AR and FR. and maintain the recycling of particles through the Chemical loop (J. C. Bandara et al., 2020). Figs 10 and 11 respectively show the particle flow pattern and the corresponding pressure contours at the time intervals of 7.22 to 8.50 sec in the connection loop. This time interval is indicated to a pressure peak highlighted in Figure 22 (dotted blue box), during which the pressure stabilizes, and the connection loop is filled up with CSP.s. Region A (AR-connection loop intersection) and region G (FR-connection loop intersection) are considered for analysis.

The pressure contours confirm that a higher average pressure difference between the AR and FR. for the time interval selected is 2024 Pa, causing a backflow situation in connection loop (Figure

24a, t: 7.22-7.42 sec). Backflow inside the connection loop from AR to FR. increases the volume fraction of solid in the Region-G. Once the backflow ends, the average pressure difference between AR and FR. suddenly reduces to 602 Pa and the pressure starts to stabilize inside the loop (Figure 25, t: 7.51-8.50 sec). Meanwhile, the filling up of the connection loop occurs. Those particles entering the connection loop try to stop the backflow. As observed in Figure 24a (t: 7.51 and 7.70 sec), the velocity vectors intersect and point towards each other, and the connection loop begins balancing pressure inside the system. The pressure difference between zones A and G are 765.4 and 546.2 Pa at 7.51 and 7.70 sec, respectively. The quantity of particles entering the connection loop increases as pressure difference reduces. The concept of increasing volume fraction of solids particles inside the connection loop is observed through the velocity vectors (Figure 24a, t: 7.70 sec). The velocity vectors in Figure 24a (t:8.50sec) confirm the continuous flow of CSP. into the connection and the corresponding pressure contours (Figure 25, t:8.50sec) provide validation for stabilized pressure condition in between AR and FR.

Figure 26 shows the magnitude of gas velocity at ZONE-A and G withing the time interval t=7.22-8.50 sec (yellow dotted box). As observed, the moment of backflow begins when an abnormal high gas velocity peak (Figure 26, black dotted circle) occurs at Zone-G. The impact of gas velocity peak and its effect on backflow is discussed in next section. Apart from that, a general observed trend is that the value of gas velocity inside the loop at zone-A remains higher than that in zone-G because AR operates on higher fluidization velocity of 3.2m/sec while the magnitude of velocity observed in FR. ranges from 0-0.04m/sec (Figure 20a). Thus, due to this trend, the CSP. flow from FR. into connection and further into AR

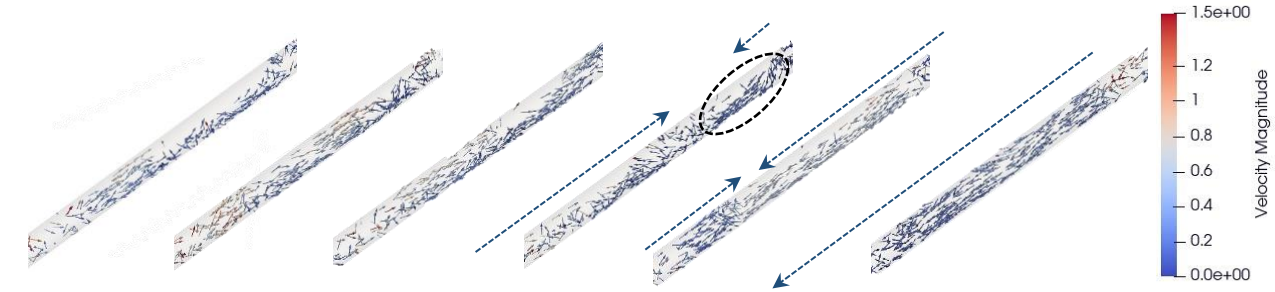

(a)

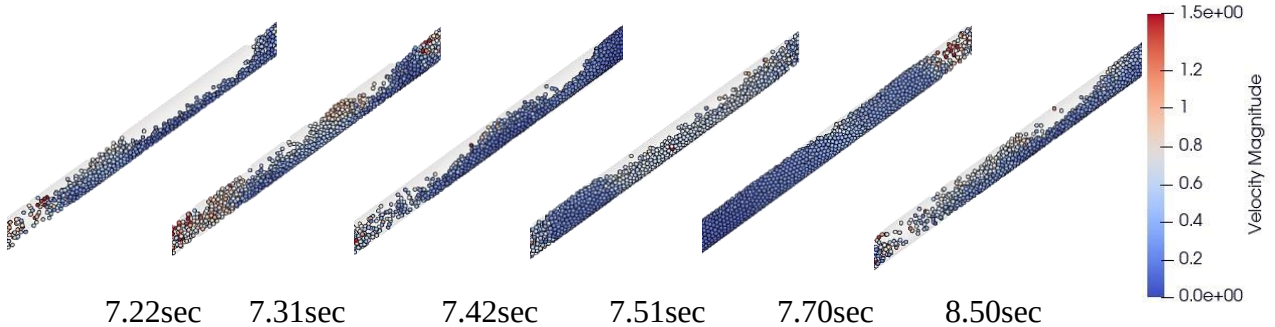

7.22sec 7.31sec 7.42sec 7.51sec 7.70sec 8.50sec

(b)

Figure 24. Circulation of catalytic solid particles inside connection loop a) Velocity vectors magnitude, b) Particle velocity magnitude. Simulation condition: V.AR: 3.2 m/sec, V_{FR}: 0.0025 kg/sec, Volume fraction of solid inside LC/AR/FR: 0.5

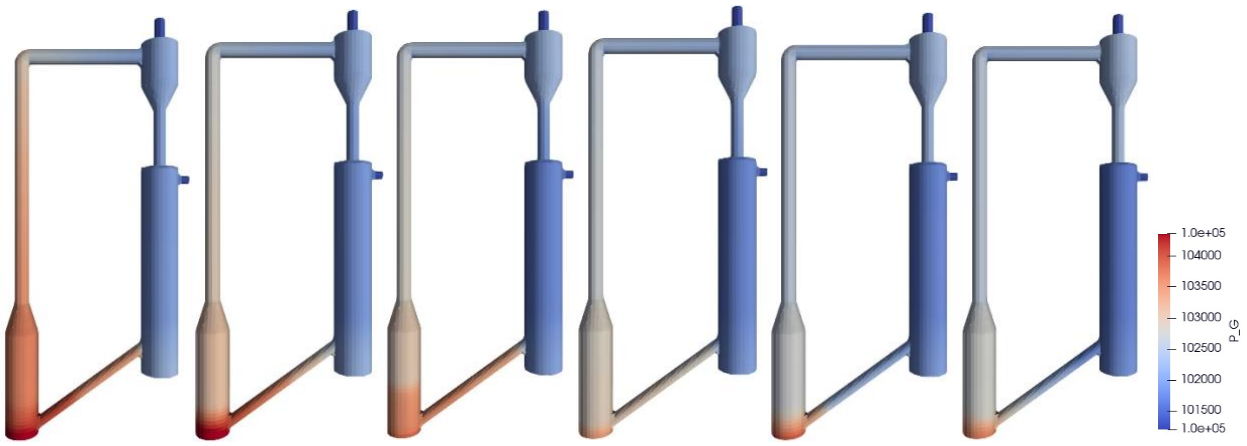

7.22sec 7.31sec 7.42sec 7.51sec 7.70sec 8.50sec

Figure 25. Pressure contours in chemical loop during time interval of 7.22-8.50 sec. Simulation condition: V.AR: 3.2 m/sec, V_{FR}: 0.0025 kg/sec, Volume fraction of solid inside LC/AR/FR: 0.5

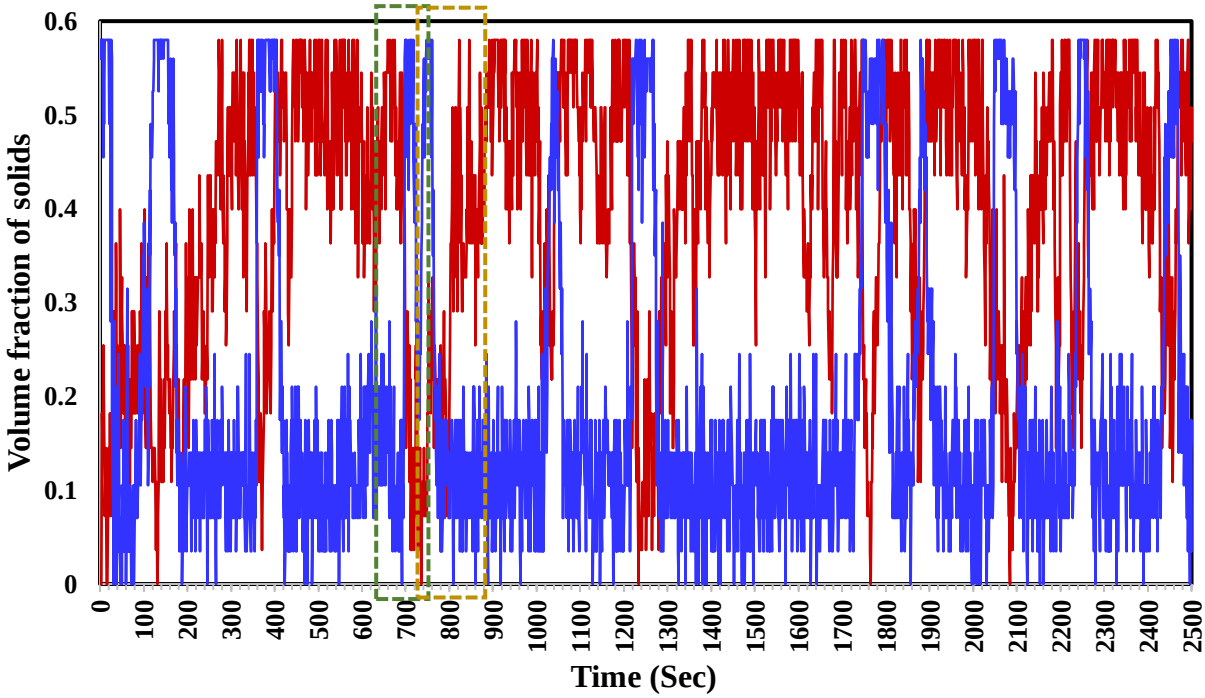

Figure 26. The graph between Volume fraction of Solids and time for — Avg (EP_S) ZONE-A and — Avg (EP_S) ZONE-G between time intervals 0-25 second.

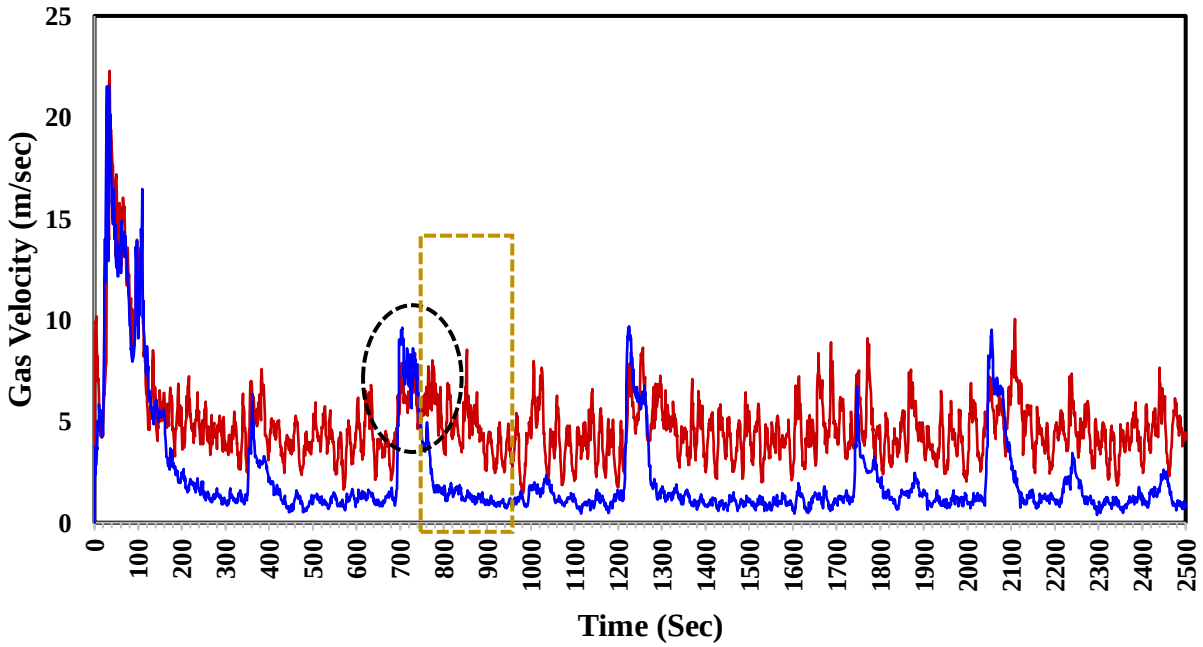

Figure 27. The graph between Gas velocity and time for — Avg (Gas_Velocity (Magnitude)) ZONE-A — Avg (Gas_Velocity (Magnitude)) ZONE-G between the time interval 0-25 sec.

4.3.2 Backflow in connection loop

Figure 28 a and b show the particle flow pattern at the moment of back flow formation between 6.98 to 7.20 sec in connection loop. The direction of vectors confirms the formation of backflow. The corresponding pressure contours and pressure peak are shown in Figure 29 and Figure 22 (dotted black oval), to explain the backflow of particles inside the loop connection which occurs due to instable pressure condition.

First, backflow is a condition in which a high fluidization velocity inside the AR forces the particles from AR entering back into FR through the connection loop, in the direction opposite to the intended direction of flow. The backflow forms when a very high-pressure difference is developed between AR and FR (Figure 29, t: 6.98-7.20sec). In this case, the pressure difference reaches the maximum value of 13841 Pa at time 6.98 and gradually reduces to 1562 Pa ultimately (7.20 sec). The details of the values can be observed in the pressure peak depicted in Figure 22 (green oval). During the same period, the majority of particles in AR gain sufficient kinetic energy to fluidized and enter the riser tube. The backflow begins with a creation of void space (Figs 14a, b: dotted curve, circle) inside the connection loop. The void space expands, and the pressure differences are declined as the particles are thrown out to the FR through the back flow inside the connection loop (Figure 28a, b).

The trend of volume fraction of particles flowing backwards through the connection loop can be analyzed from Zone-A and Zone-G (Figure 26, green dotted box). At time interval of 6.98-7.08 sec, a sudden increase in volume fraction of particles at Zone-A is observed from 0.22 to 0.29, which is accompanied with a sudden decrease is observed at Zone-G from 0.58 to 0.42 due to flow of particles backwards into the connection loop. The velocity magnitude of injection gas at Zone-A is always greater than Zone-G under the stabilized condition, when the particles flow from FR

to the AR through the connection loop. However, the flow pattern shows a high magnitude of particle velocity in Zone-G during the condition of backflow (Figure 28a, yellow dotted box). At time interval of 6.98-7.20 sec, the magnitude of gas velocity at Zone-G abruptly increases (Figure 27, black dotted circle) from 4.761 m/sec to 9.618 m/sec, which creates a high velocity zone near the intersection of FR and connection loop (Figure 28a, yellow dotted box). This is because, a high fluidization velocity of gas injected at the AR inlet with a diameter of 80 mm enters the connection loop with diameter of 25 mm and causes momentum exchange due to particle-gas interaction. According to the principle of continuity, the flow rate increases as the diameter is constricted. A similar phenomenon is observed when AR inlet gas velocity of 3.2 m/sec enters the riser.

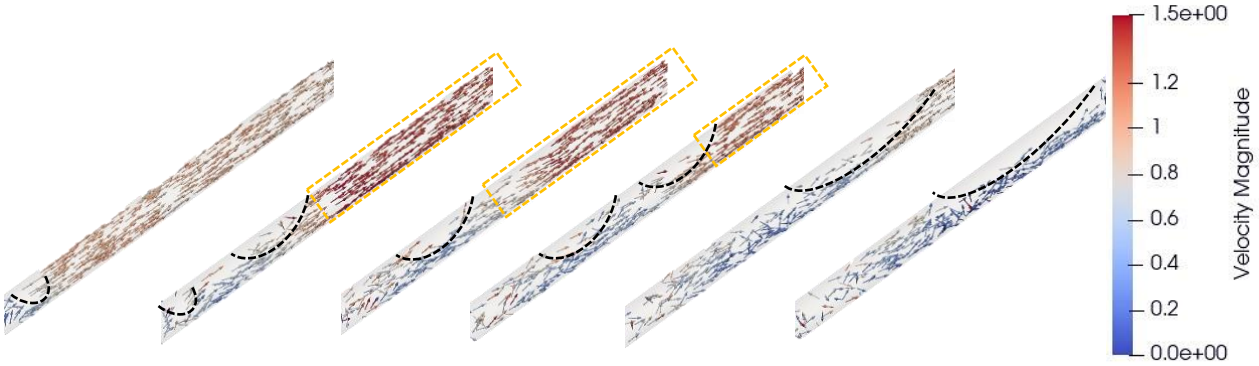

6.98sec 7.05sec 7.08sec 7.10sec 7.14sec 7.20sec

(a)

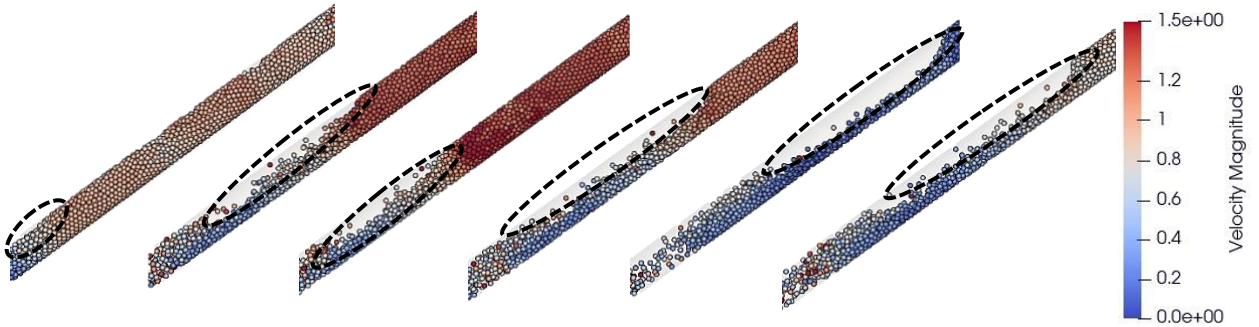

6.98sec 7.05sec 7.08sec 7.10sec 7.14sec 7.20sec

(b)

Figure 28. Circulation of catalytic solid particles inside connection loop a) Velocity vectors magnitude, b) Particle velocity magnitude. Simulation condition: V.AR: 3.2 m/sec, V_{FR}: 0.0025 kg/sec, Volume fraction of solid inside LC/AR/FR: 0.5

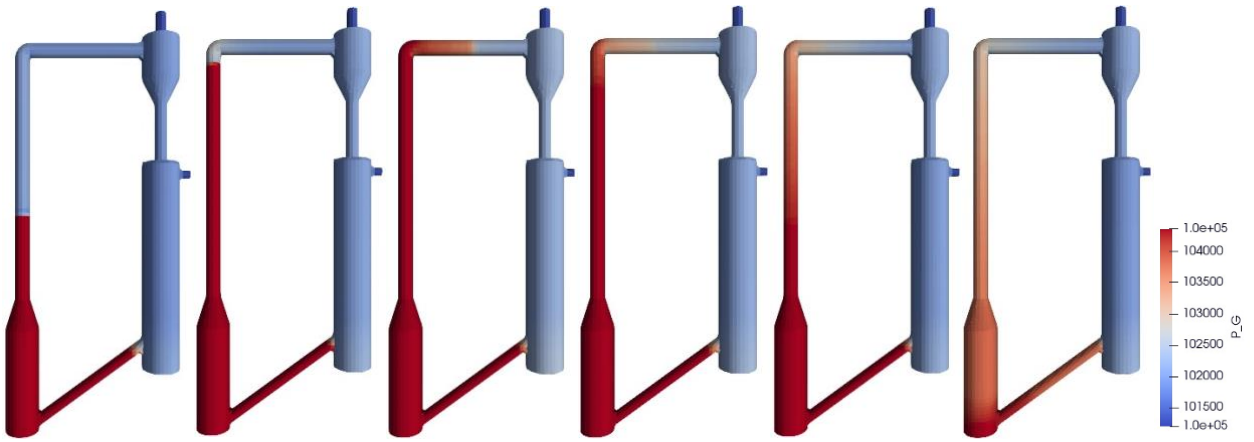

6.98sec 7.05sec 7.08sec 7.10sec 7.14sec 7.20sec

Figure 29. Pressure contours in chemical loop during time interval of 6.98-7.20 sec. Simulation condition: V.AR: 3.2 m/sec, V_{FR}: 0.0025 kg/sec, Volume fraction of solid inside LC/AR/FR: 0.5

4.4 Flow pattern in AR

4.4.1 Fluidization in the AR

Several turbulent regimes (Konan & Huckaby, 2021) are formed inside the AR due to injection of high fluidization velocity at AR inlet. The AR maintains particle flow in the chemical loop when particles enter through the connection loop from the FR and the AR fluidizes the particles through the riser tube into the cyclone distributor. Figure 30 shows the particle flow pattern (in terms of vectors and particles volume fraction) at the time interval of 2.80 to 3.1 sec, at gas inlet mass flow rate of 0.0025 Kg/sec in FR and gas inlet velocity of 3.2 m/sec in AR The time interval indicated in this section corresponds to the minor pressure fluctuation highlighted in Figure 31 (the first dotted black box), to explain the general fluidization pattern inside AR Region B (conical section), Region-C (inlet riser tube), Region-D (pipe bend) and Region-H (inlet CD) depicted in Fig. 1 are considered to analyze the flow pattern in section 5.4.1, 5.4.2 and 5.4.3, respectively.

Under a conventional flow inside the AR before a large volume fraction of particles fluidize into riser, the particles flow forms a region of vortex (like blue dotted circle Figure 30a, t: 2.80-2.85 sec). Vortex is a phenomenon in which a curved or circular flow pattern is formed with the flow revolving around an axis line (black dotted line, Figure 30a) with fluid or particles either pointing circular upwards above an axis or vice versa. The velocity vectors in Figure 30a shows that vortex (curved vectors with circular zone) is first formed at 2.80 sec, which gradually widens and expands at time 2.85 sec. The formation of vortex confirms that the particles have gained sufficient kinetic energy from the injected gas with a velocity 3.96 m/sec (black dotted box Figure 33, Zone-B) to start fluidization inside AR (Bartocci et al., 2022), but the particle velocity (Figure 30b, range 0.4-0.7 m/sec) is not high enough to cause the particles to enter the riser tube. The bed height at this time (2.8 sec) is 122 mm. A different flow pattern is formed if the particles velocity is sufficiently high to fluidize and enter the particles into the riser tube (zone D). Under any steady state fluidization condition, which is a balanced pressure state (Figure 31), the particles near the boundaries of vortex start travelling upwards from the axis line (like red dotted circle Figure 30a, 2.80-3 sec) and they rise until the weight force due to gravity dominate the counteract lift force, which ultimately causes the particles to fall back into the AR again. While the rest of the particles below the axis line fall back, downwards into the AR (like black dotted pointer Figure 30a, 2.9-3.1 sec). According to the velocity vectors pointing downwards, the majority of volume fraction of particles entered back into the AR at 3.1 sec, while a new region of vortex (blue dotted circle) is observed. The particles volume fraction of 0 between 2.80-3.1 sec in Fig. 18 (black dotted box) validates the fluidization flow pattern inside AR

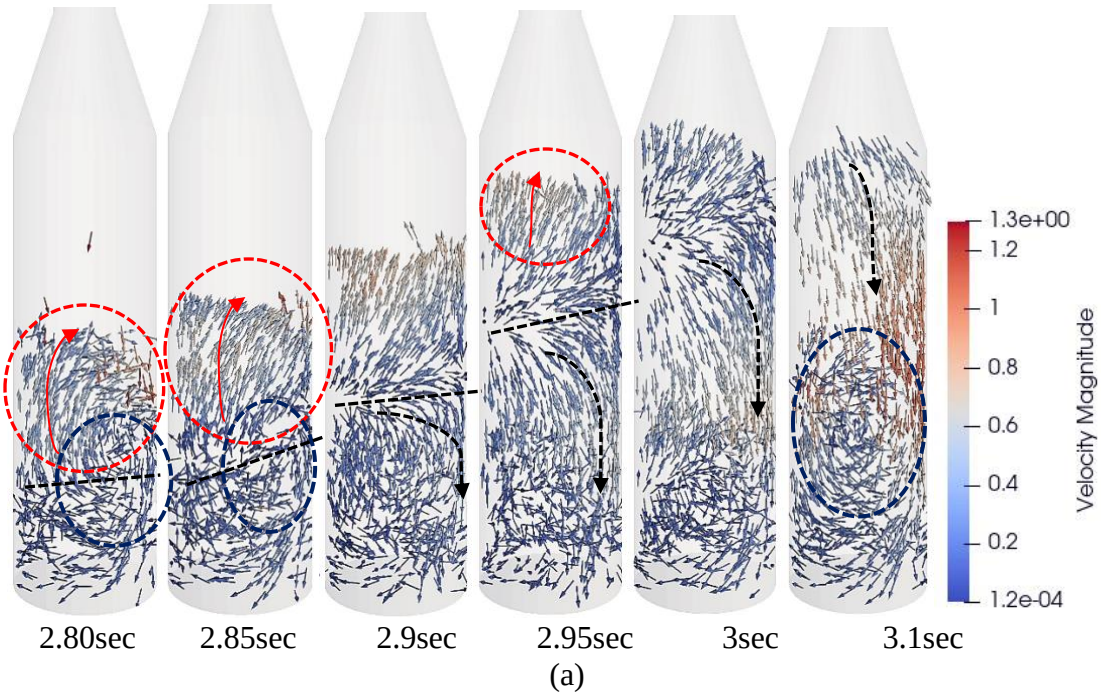

(a)

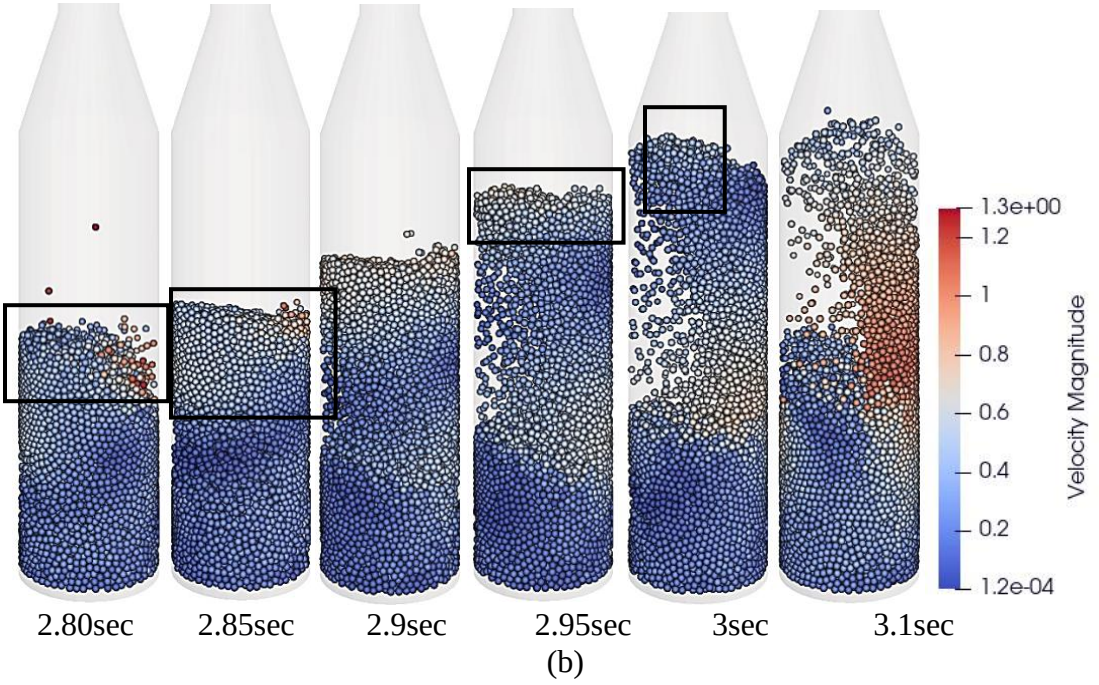

(b)

Figure 30. Circulation of catalytic solid particles inside AR a) Velocity vectors magnitude, b) Particle velocity magnitude. Simulation condition: V.AR: 3.2 m/sec, V_{FR}: 0.0025 kg/sec, Volume fraction of solid inside LC/AR/FR: 0.5

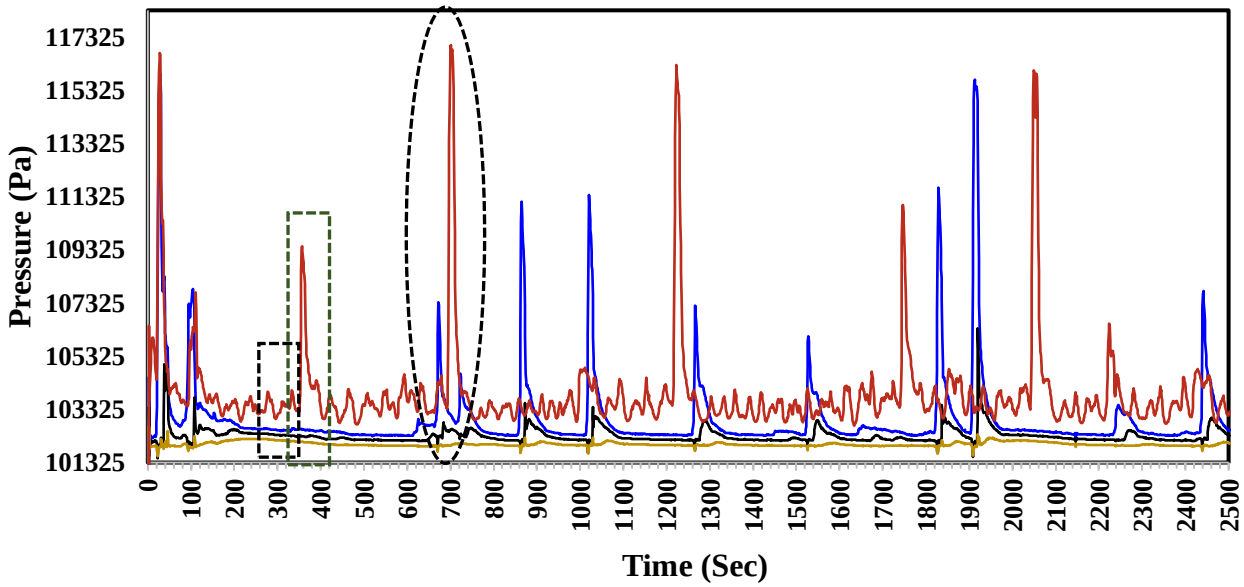

Figure 31. The graph between Pressure and time for Avg(P_G) ZONE-A, Avg(P_G) ZONE-B, Avg(P_G) ZONE-D and Avg(P_G) ZONE-H for time intervals 0-25seconds.

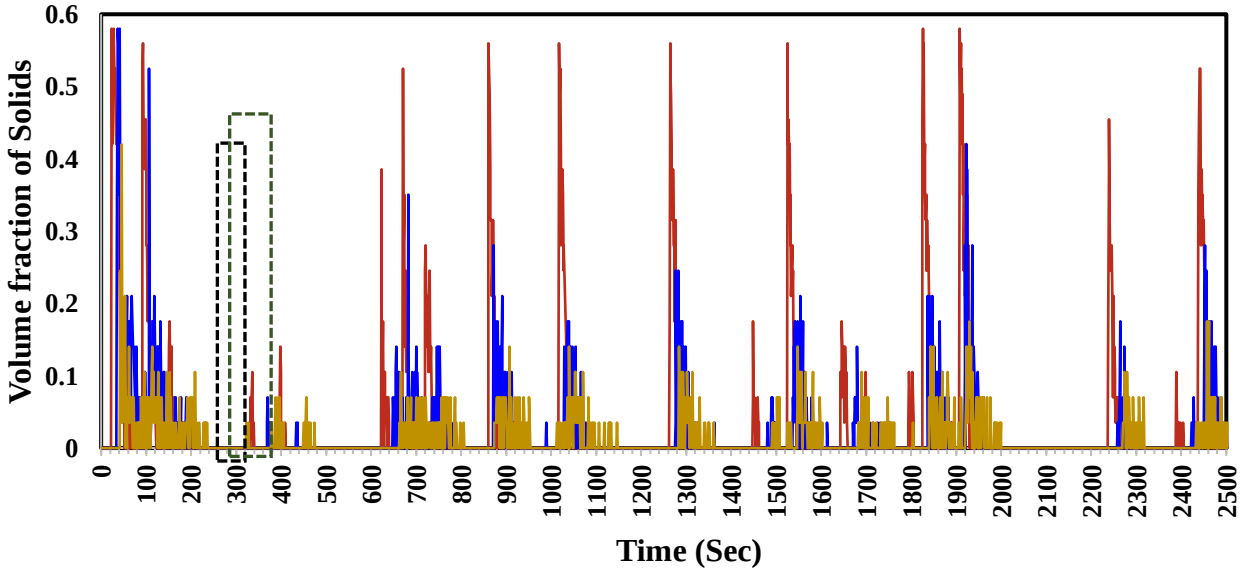

Figure 32. The graph between Volume fraction of Solids and time for Avg (EP_S) ZONE-C, Avg (EP_S) ZONE-D and Avg (EP_S) ZONE-H between time intervals 0-25 second.

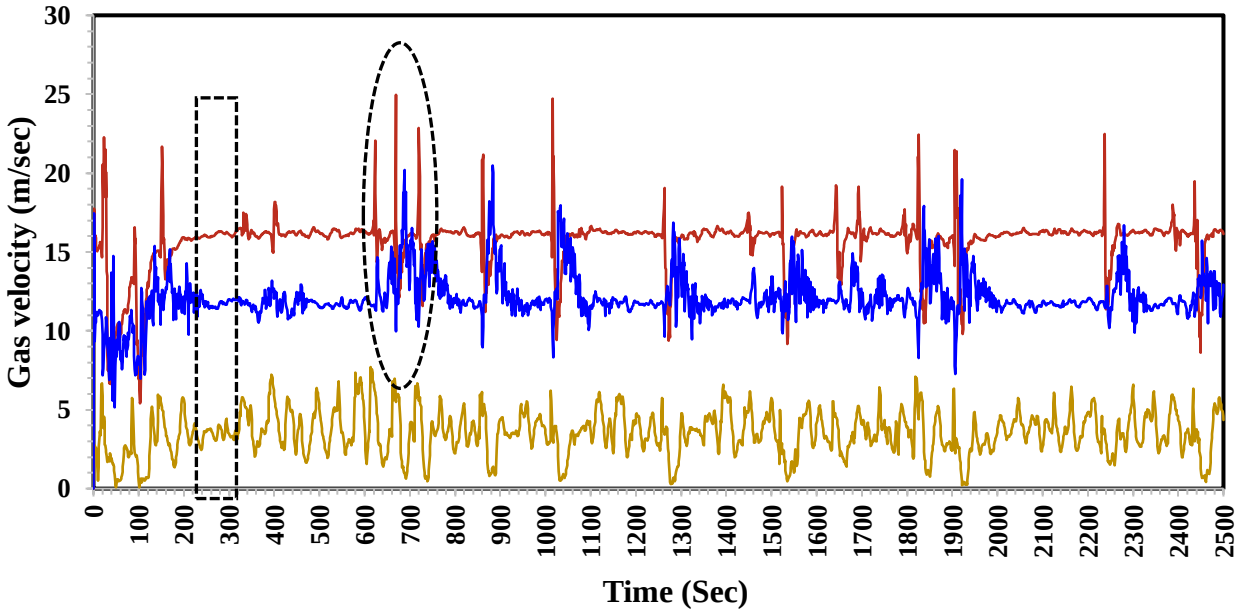

Figure 33. The graph between Gas velocity and time for — Avg (Gas Velocity (Magnitude)) ZONE-B, — Avg (Gas Velocity (Magnitude)) ZONE-C, and — Avg (Gas Velocity (Magnitude)) ZONE-H between the time interval 0-25 sec

4.4.2 Particles Rise in the AR

This section explains the second flow pattern observed inside the AR only when the particles turbulent zone has sufficient kinetic energy to fluidize from inside the AR into the riser tube. Figure 34 shows the particle flow pattern at the time intervals of 3.40 to 3.70 sec, which corresponds to the pressure peak highlighted in dotted green in Figure 31.

The development of vortex regions inside the AR due to development of high turbulent zones is a continual process. These regions are created because the velocity of injection gas at AR inlet (3.2 m/sec) is higher than the minimum fluidization velocity required (2.65 m/sec, calculated based on volume fraction of solid=0.5, density of particles: 2400 Kg/m^3 (Anantharaman et al., 2018)). The AR is gradually and partially filled with incoming particles from the connection loop, and the number of particles keeps rising, until the moment that pressure gradient between the AR and FR increased to the maximum value. At this moment, the suspension splits into two parts, resulting in

the formation of slug-like structure. Gas-solid vertical co-current upflow systems involve the upward transportation of particles as a dispersed suspension at high gas velocity. Hence a significant fraction of particles moves up the riser and the other fraction moves downward. This point is characterized by severe instability in the system. When the amount of particles reaches a sufficient bed height, which in this case is 263 mm, the particles enter the riser tube and flow through the loop. The bed height in this case is 68 mm higher than the fluidization condition. At these moments, a different flow pattern is observed inside AR, which is always accompanied by a phenomenon of backflow. However, in circulating fluidized beds like chemical looping systems, unstable conditions other than choking, such as vortex formation. First, in section 5.4.1 (Figure 30a, 3.1 sec), it was observed that a region of vortex which was developed continues into the flow pattern explained in this section. As only when the velocity imparted to particles is sufficiently high, they rise into the riser tube. As per Figure 30b, the average velocity of particles during steady fluidized condition (section 5.4.1) flowing in the upward direction is 0.4-0.7 m/sec, while the range of velocity of particles in this section (Figure 34b) is 0.8-1.5 m/sec. From 3.1 to 3.4 sec, the particles velocity vectors above the black dotted line of axis flow upwards gradually (red dotted circle, Figure 34a). At the same time, the particles below the line fall back into the AR (like Figure 34a, t: 3.40-3.70 sec) due to dominating force of gravity. Due to the principle of continuity, the velocity value increases (like Figure 34a/b, t: 3.48-3.55 sec) as the particles flow from a conical section with inlet diameter (80 mm) to the outlet section with diameter of 30 mm and they experience a constriction. At 3.5 sec, 15% of the particles have entered the conical section (vectors pointing upward, Figure 34a), while majority of particles have flowed back to AR (vectors pointing downward). Also, at the same time, a region of new vortex is formed (blue doted circle, Figure 34a). Finally, at 3.70 sec, the particles are falling back into the AR (black dotted arrow, Figure

34a). As per Figure 32 (green dotted box), the volume fraction of particle between 3.40-3.70 sec ranges from 0-0.11. This increase in trend confirms that the particles enter the riser section which is explained in the next section.

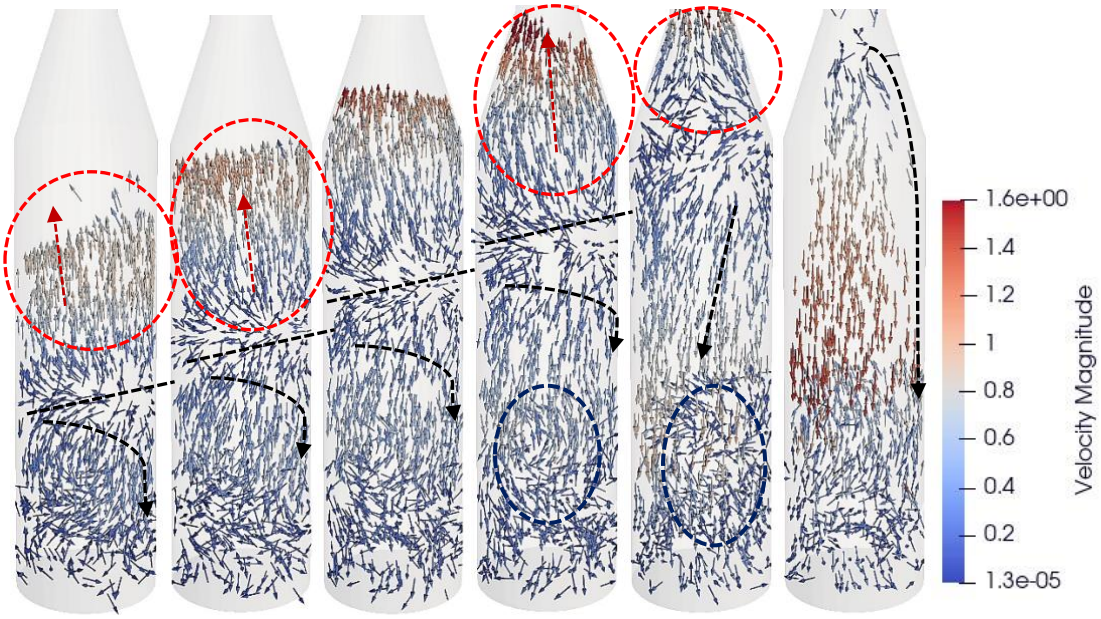

3.40sec 3.45sec 3.48sec 3.5sec 3.55sec 3.70sec

(a)

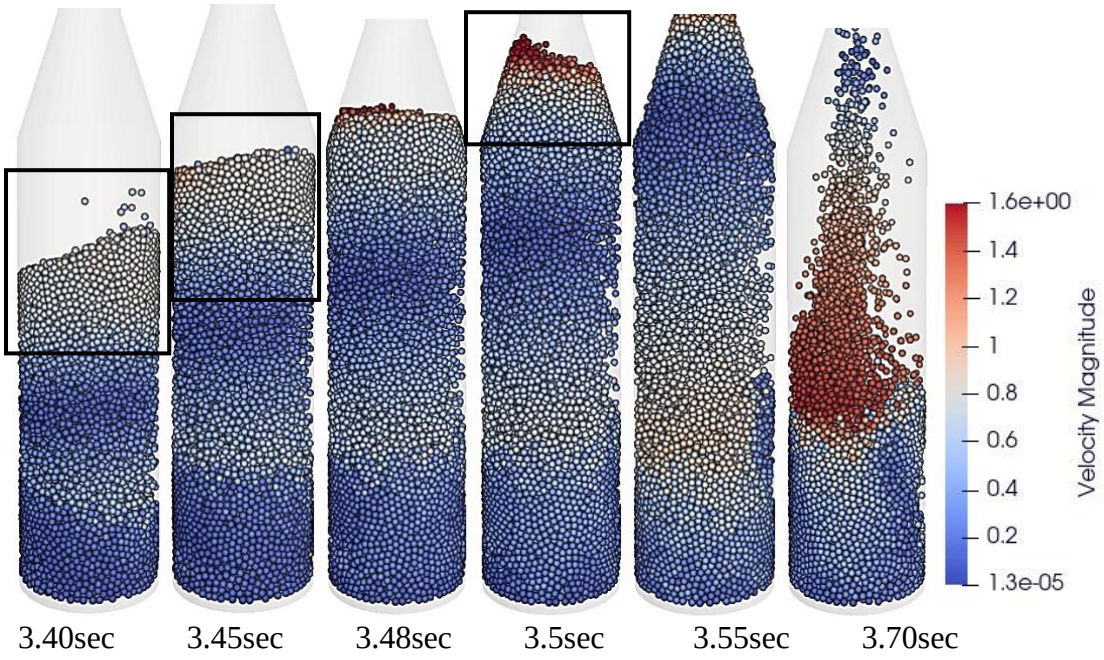

(b)

Figure 34. Circulation of catalytic solid particles inside AR a) Velocity vectors magnitude, b) Particle velocity magnitude. Simulation condition: V.AR: 3.2 m/sec, V_{FR}: 0.0025 kg/sec, Volume fraction of solid inside LC/AR/FR: 0.5

4.4.3 Flow pattern through Riser tube

The third flow pattern in AR occurs when the particles under the turbulent zone get sufficient kinetic energy to fluidize into the riser tube. Figure 35 shows the particle flow pattern at the time intervals of 6.95 to 7.06 sec, during which particles flow into riser tube. This time interval corresponds to a pressure peak highlighted in Figure 31 (dotted black circle), and the pressure contours depicted in Figure 36.

The particles flow into the riser when two requirements are satisfied: I) a high-pressure zone is developed in AR and II) a turbulent exchange of momentum happens between gas velocity and particles. Pressure contours (Figure 36, 6.95 sec) show the development of a high-pressure zone with the value of 116293 Pa (Figure 31, Zone-A). Figure 33, Zone-C confirms a sufficiently high gas velocity (19.92 m/sec).

The particle flow begins with upper half of the velocity vectors (red dotted box, Figure 35a, 6.95 sec) pointing upwards, while the lower half of the particles falling back into the AR (blue dotted circle, Figure 35a, 6.95 sec). Two void spaces (yellow dotted circle, Figure 35b) are created as the particle flow begins at 6.95 sec and these empty spaces are formed due to particles trying to escape the AR At 6.98 sec, the particles begin to rise high inside the riser tube gaining kinetic energy from the injected gas (Figure 35a, 21.24 m/sec). Meanwhile, the particles rising through the riser tube tend to split into smaller clusters and the void spaces between the clusters begin to expand (red dotted circle Figure 35b, 7.02 sec). Clusters are due to hydrodynamics effects and weak inter-particle forces. These particles gain a high velocity in range 8-10 m/sec, which is almost three times higher than the fluidization velocity (2.6 m/sec) (red dotted circle, Set-A). Simultaneously, the void spaces in lower section of AR (yellow dotted circle Figure 35b) keep expanding as particles fall back into the AR and, the first cluster of particles (cluster A) reaches the pipe bend (Figure 35b). These particles gain a velocity magnitude ranging between 12-14 m/sec, while a newer cluster of particles is formed (cluster B), which follows a similar trend. At 7.04-7.06 sec (Figure 35a, b), the particles flow through the pipe bend, the horizontal section of the riser tube and ultimately cyclone distributor. On the other side, the rest of the particles (blue dotted circle Figure 35a, 7.06 sec) below the inlet of riser section tend to fall back into the AR due to the act of weight force. The development of pressure counters during the transition of particles from AR into the riser tube, pipe bend and the cyclone distributor is depicted in Figure 36. Starting 6.95 sec to 7.06 sec, the pressure on AR-Riser section is in the range of 116293 Pa-117019 Pa (Figure 31), and this pressure range is higher to cause the particles to enter the riser tube. Also, a concurrent phenomenon of backflow occurs in the similar time range.

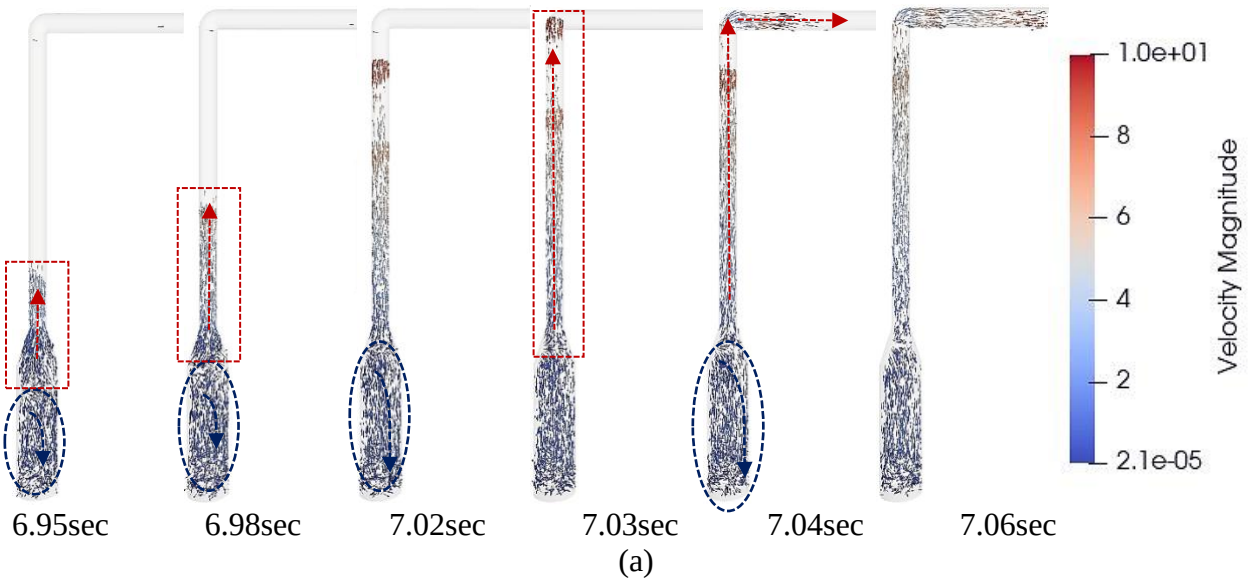

(a)

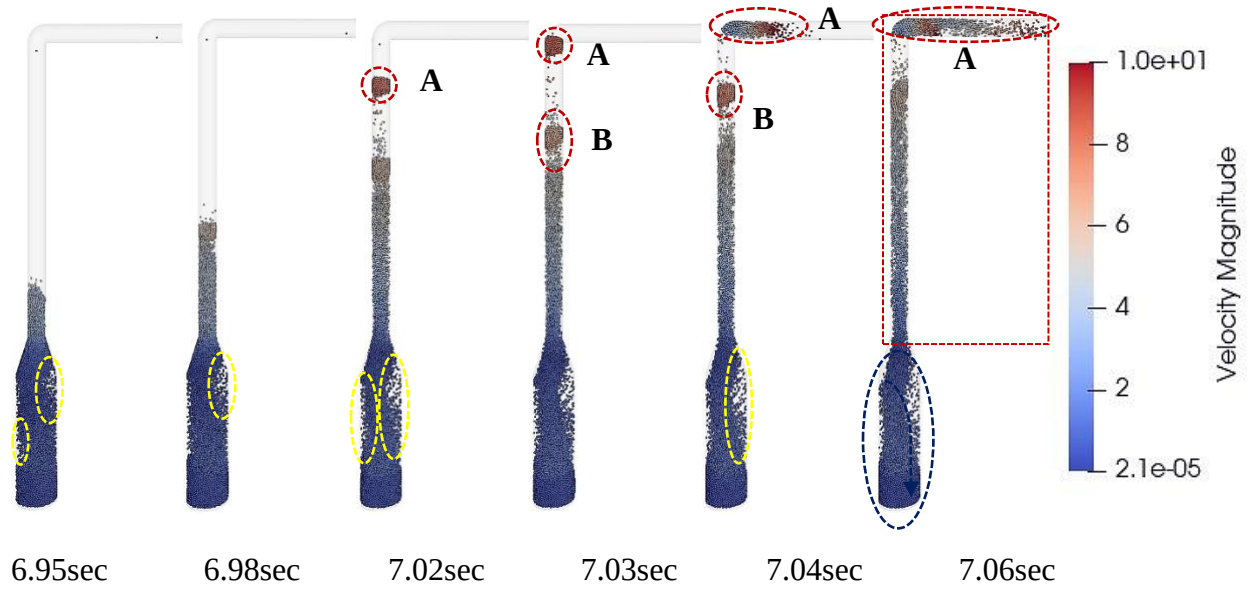

(b)

Figure 35. Circulation of catalytic solid particles inside AR and riser a) Velocity vectors magnitude, b) Particle velocity magnitude. Simulation condition: V.AR: 3.2 m/sec, V_{FR}: 0.0025 kg/sec, Volume fraction of solid inside LC/AR/FR: 0.5

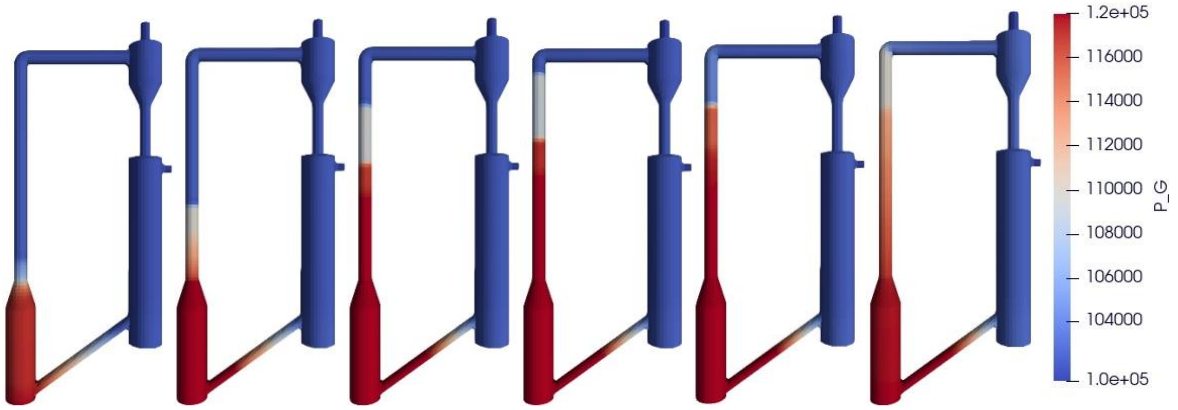

6.95sec 6.98sec 7.02sec 7.03sec 7.04sec 7.06sec

Figure 36. Pressure contours in chemical loop during time interval of 6.95-7.06 sec. Simulation condition: V.AR: 3.2 m/sec, V_{FR}: 0.0025 kg/sec, Volume fraction of solid inside LC/AR/FR: 0.5

4.5 Flow pattern in the Cyclone distributor

It is substantial to comprehend the flow pattern of particles entering the cyclone distributor from the AR because it separates the particles from the stream of gas and function like filtration method (Deng et al., 2019). The particles experience three different flow patterns and interaction in cyclone, including particle-wall interaction in the cylindrical zone, swirling pattern in the inverted cone section, and finally falling into the downcomer zones due to the gravity. Figure 37 shows the particle flow pattern at the time intervals of 7.09 to 7.79 sec, corresponding to the pressure peak highlighted in Figure 38 (dashed black circle-Zone E). Region-D (Riser pipe bend), Region E (inverted conical section of cyclone distributor) and Region-H (inlet CD) depicted in Fig. 1 are considered to analyze the flow pattern in section.

The particles flow through the horizontal section of riser tube (red dashed line Figure 35a, 7.04 sec) into the CD inlet. They finally enter the cylindrical section of cyclone distributor (like red dashed circle Figure 37a, 7.09 sec), at a high velocity from riser tube ranging from 6.5-8 m/sec. Right after they entered the CD (7.10 sec), the particles interact with the wall of cylindrical section,

developing a spiral (vortex) motion (dashed red line Figure 37a). Since the inertia of solid particles is larger than the gas medium, the particles begin to hit the cylindrical walls of the CD and start off to fall downward into the inverted conical section (red circle, Figure 37a/b, 7.20 sec). Cyclone distributor is a low-pressure system with an outlet open to atmosphere for the exit gases to evacuate the chemical loop freely and thus maintaining the pressure balance (stability condition) inside the system (Wang et al., 2019). This phenomenon can be corroborated by observing a transition in pressure value from a high-pressure turbulent zone from AR (Zone-D) with a pressure (102390 Pa) into a low pressure (101730 Pa) inside the CD (Zone-E) as it is confirmed from the pressure peak (Figure 38) as well. At 7.37 sec, the particles interact with the wall of the inverted conical section and flow downwards (red circle Figure 37a/b), entering the downcomer pipe below the conical connection. It should be noted that, a sudden drop in the particle velocity occurs from 0.6 to 0.2 m/sec before the particles enter the inverted conical section. At the exit of this section, the particles velocity again increases to the values of 1.6-2 m/sec due to the principle of continuity. The maximum volume fraction of particles in CD is accumulated at its conical section.

Fig. 25 gives the volume fraction of particles flowing through regions D, E, and H. From t: 7.09-7.79 sec, the volume fraction of particles (Zone-H) reduced from 0.07 to 0.03, confirming that particles flooded through the CD inlet into cyclone distributor. At the same time, the volume fraction of particles in Zone-E increased from 0.03 to 0.17 and finally decreased back to 0.03 as the particles flow through the inverted conical section.

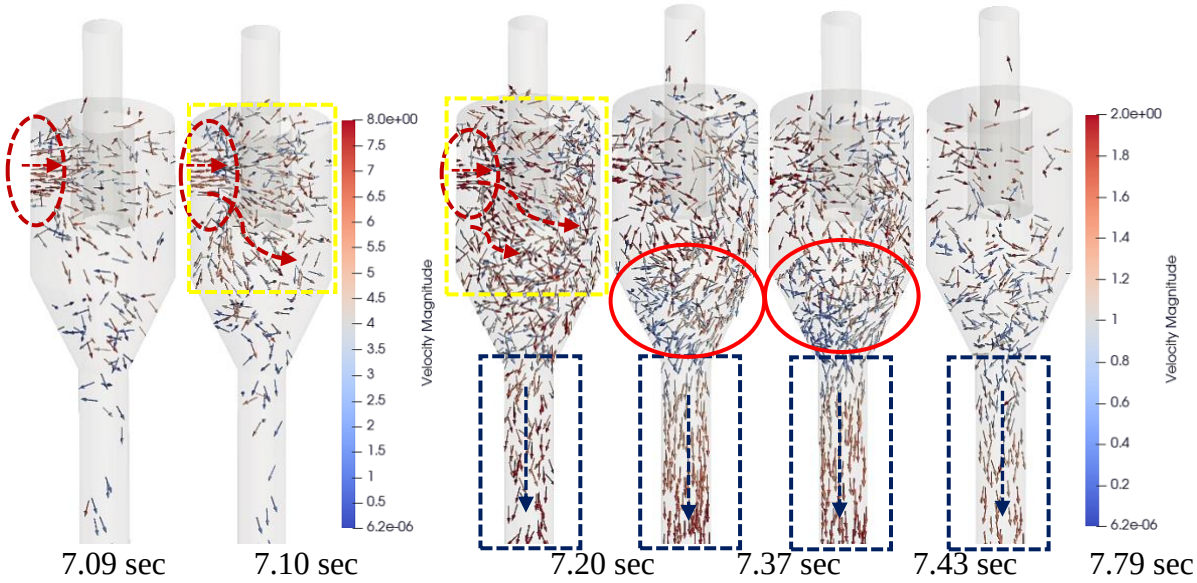

(a)

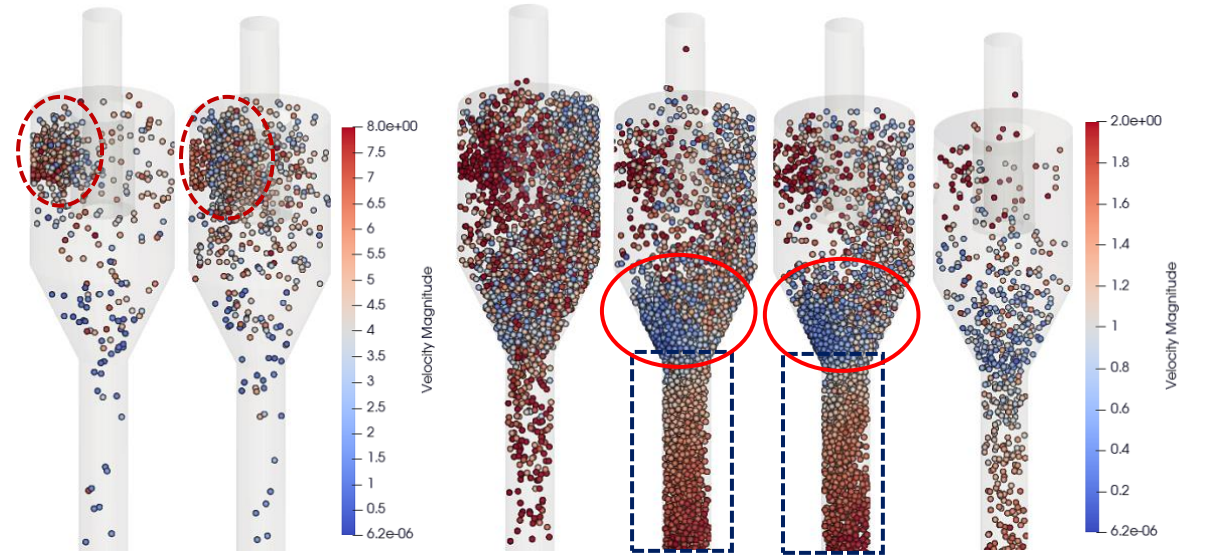

(b)

Figure 37. Circulation of catalytic solid particles inside the cyclone distributor a) Velocity vectors magnitude, b) Particle velocity magnitude. Simulation condition: V.AR: 3.2 m/sec, V_{FR}: 0.0025 kg/sec, Volume fraction of solid inside LC/AR/FR: 0.5

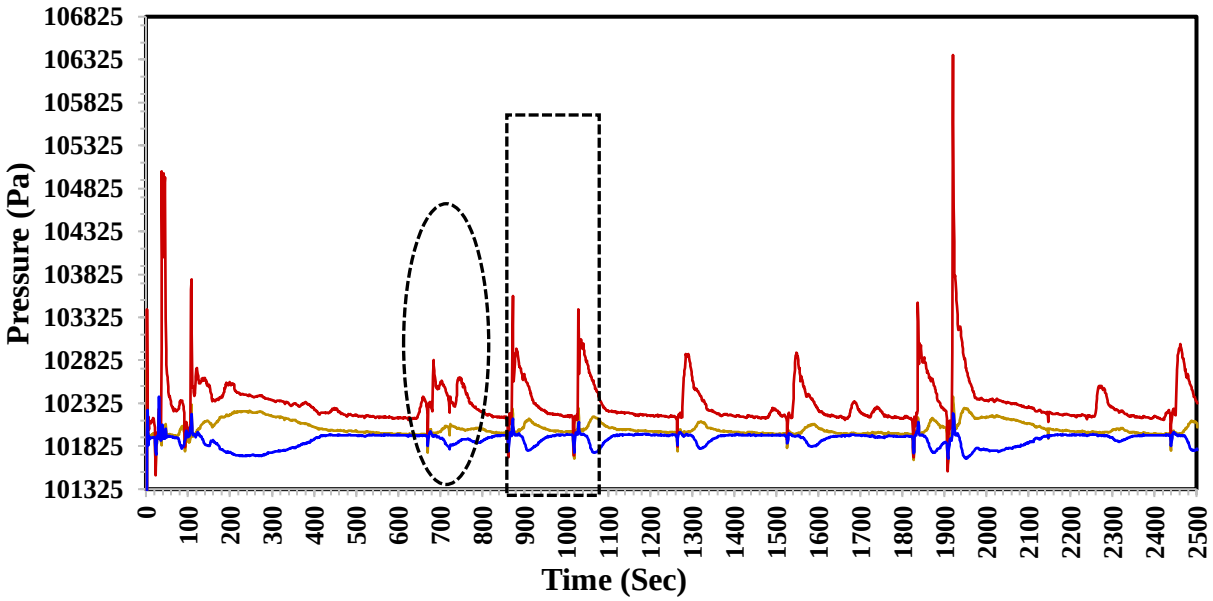

Figure 38. The graph between Pressure and time for — Avg (P_G) ZONE-D, — Avg (P_G) ZONE-E, and — Avg (P_G) ZONE-F for time intervals 0-25seconds.

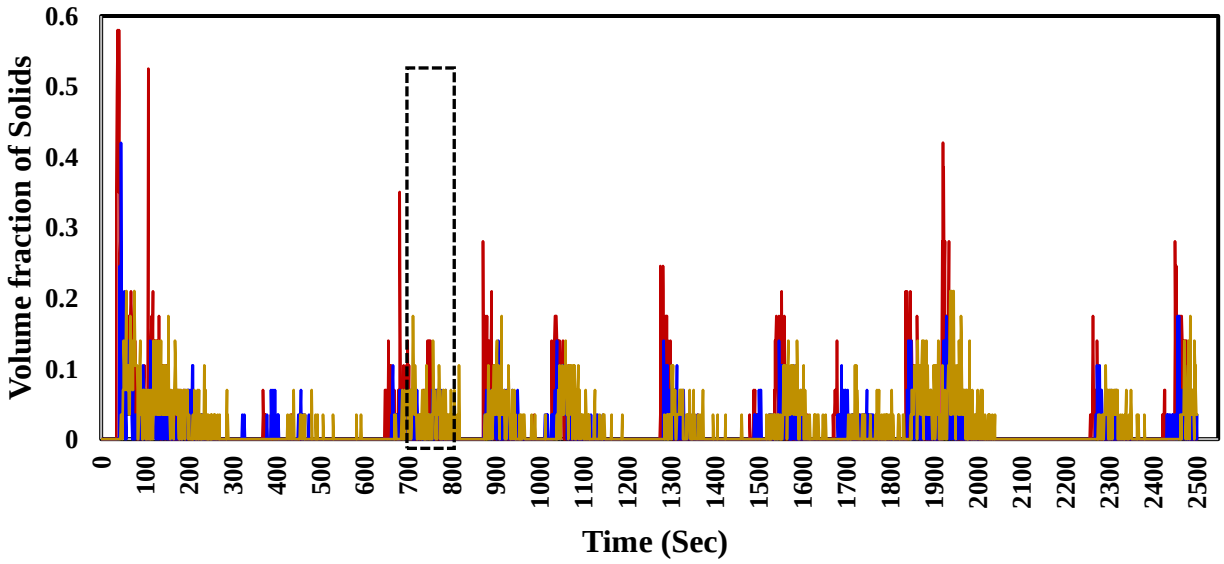

Figure 39. The graph between Volume fraction of Solids and time for — Avg (EP_S) ZONE-D, — Avg (EP_S) ZONE-E and — Avg (EP_S) ZONE-H between time intervals 0-25 second.

4.6 Flow pattern in downcomer

Fluid flow pattern inside the downcomer is shown in Figure 40. The time interval indicated in this section corresponds to the pressure peak highlighted in Figure 38 (dotted black box). Region E (inverted conical section of cyclone distributor) and Region-F (inlet FR) depicted in Fig. 1 are considered to analyze the flow pattern in section.

The particles enter the FR in a gradual process. First, the particles fall into the downcomer under the influence of gravity, and they fill up around 30% of the downcomer (Figure 40, 8.20 sec). At this moment pressure at Zone-E (102203 Pa) is larger than the pressure at Zone-F (101945Pa). This pressure difference prevents the backflow of particles from FR into the cyclone distributor. Then, the particle inside the downcomer gradually flows into the FR, where they initially experience fluidization. The velocity vectors (like blue dotted circle Figure 40a) confirm the particle flow inside the downcomer, while the direction of flow of particles inside the FR shows the beginning of the particle's entry inside FR (like red dashed box Figure 40a). As observed in Figure 38, the pressure differences between the Zone-E (101904 Pa) and Zone-F (101908 Pa) reduces to - 4 Pa after 8.55 sec. Negative sign indicates a condition of pressure relief and thus a vortex is generated (yellow dashed box Figure 40a). The vortex is generated since the forces acting due to fluidization velocity at AR inlet begin to dominate the gravitation forces and this marks the beginning of fluidization in the FR. Further at 9.25 sec, a fluidization pattern (like yellow dashed box Figure 40a) is observed inside the FR. while the vectors of particles inside the downcomer points downward (blue dashed circle), which confirms the FR being filled with particles. However, the bed height of FR does not increase with the incoming particles because an almost the same

number of particles leaves the FR into the connection loop (8.20 to 9.95 sec). The whole process of filling up the downcomer and particles departure to the FR takes around 2 sec.

Figure 41 shows the volume fraction of particles flowing from the cyclone distributor inside the downcomer. The gradual reduction of particles inside the downcomer Figure 37b (blue dashed circle) validates the emptying of the particles from downcomer into the FR. The reduction of volume fraction of particles (Figure 41) at Zone-E (yellow dotted box) from 0.034 to 0 show that the particles emptying the cyclone distributor. While the volume fraction of particles at Zone-F (Fig 27, black circle) increases from 0.39 - 0.58. This increase in volume fraction of particles validates the entry of particles inside the FR.

(a)

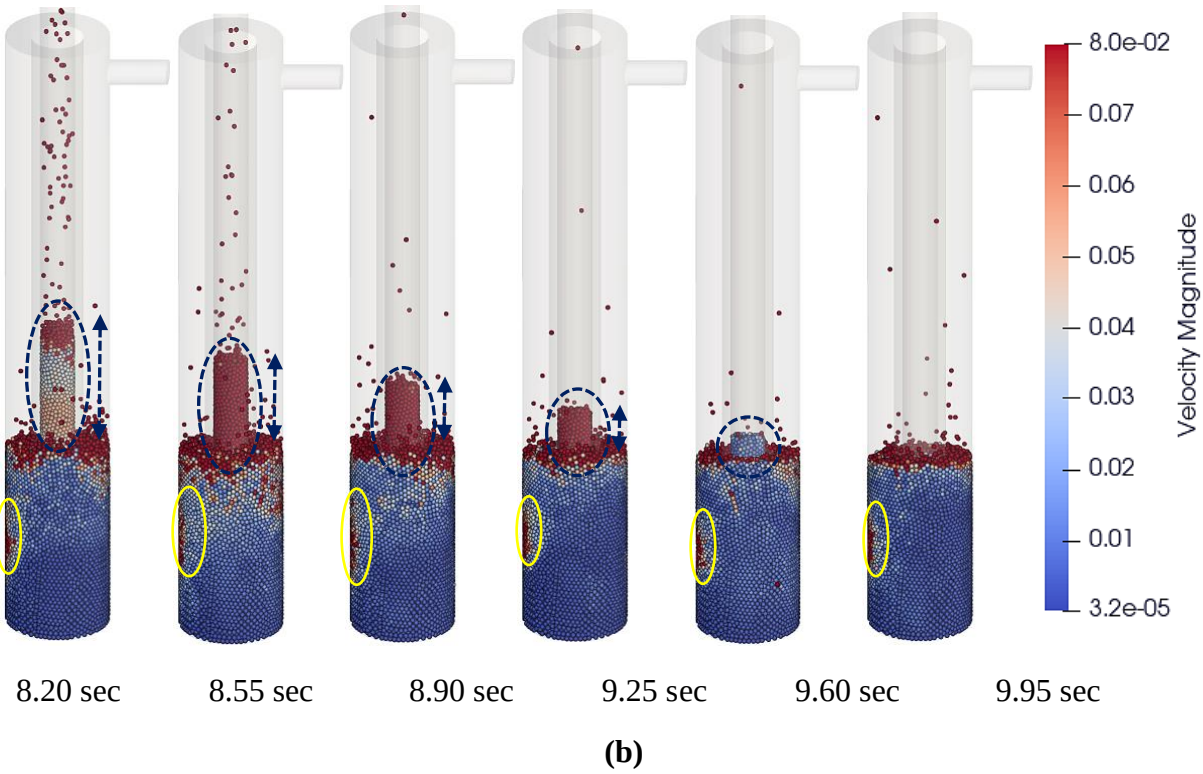

(b)

Figure 40. Circulation of catalytic solid particles inside the downcomer a) Velocity vectors magnitude, b) Particle velocity magnitude. Simulation condition: V.AR: 3.2 m/sec, V_{FR}: 0.0025 kg/sec, Volume fraction of solid inside LC/AR/FR: 0.5

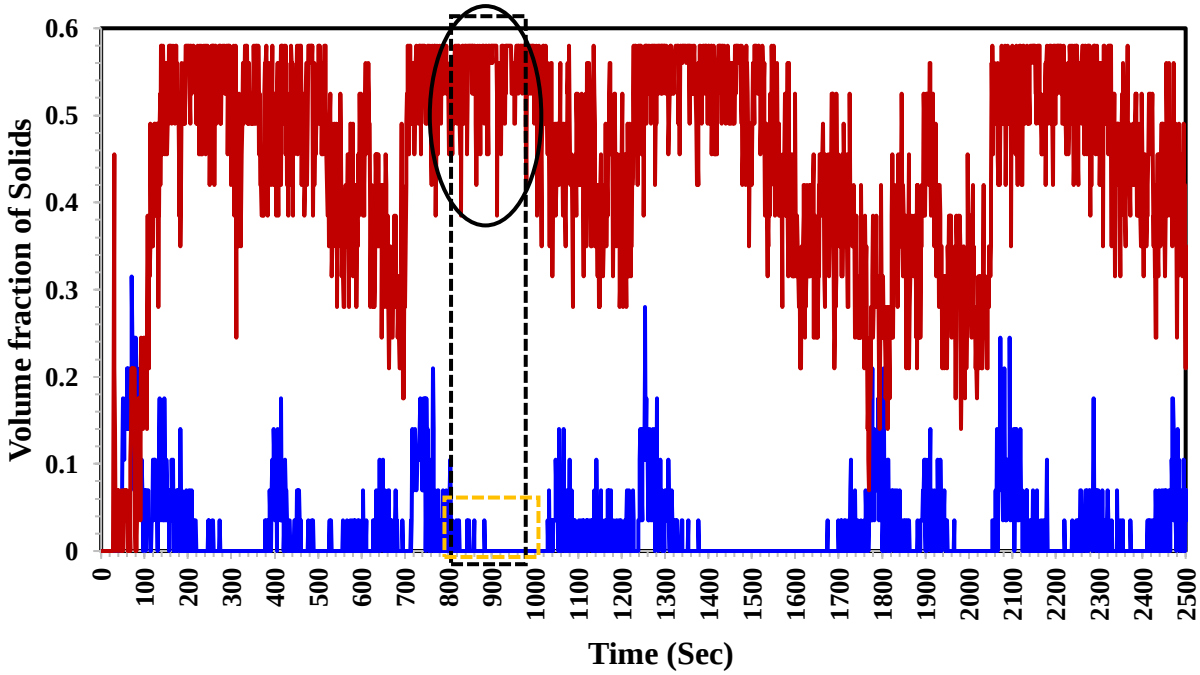

Figure 41. The graph between Volume fraction of Solids and time for — Avg (EP_S) ZONE-E and — Avg (EP_S) ZONE-F between time intervals 0-25 second.

4.7 Impact of Velocity in AR on Chemical loop

AR inlet velocities ranging from 2.6-3.5 m/sec were chosen to understand the impact of variable velocity inside the looping system. The time interval of 10-12 sec indicated in this section is to a pressure peak highlighted in Figure 42 and Figure 43 (dashed black box). Region-B (AR conical section) and Region F (Exit at downcomer to FR), which are at the same elevation inside two different reactor zones were considered to analyze the impact of variable velocity.

First, the impact of different velocities on a looping system is the development of pressure zones inside the AR, which increases with velocity increases from 2.6-3.5 m/sec. A variable velocity impacts the pressure inside the looping system, which further impacts the time taken for the system to reach steady state condition. A velocity value that causes abnormally high-pressure zones (increased pressure drop) (Li & Shen, 2020) inside the geometry is undesirable. The differences in pressure further impact the volume fraction of particles flowing through the loop. This study is performed to determine the value of velocity, which gives moderate pressure differences inside the system, imparts maximum volume fraction though the loop and enters steady state flow condition within a reasonable time frame.

At 2.6 m/sec (Figure 42, black pressure line), which is the minimum fluidization velocity, the pressure within the system ranges from 101325-103782 Pa (Figure 42, peak D, t: 0.01 sec). It is a minimum velocity for fluidization, which is not sufficient to cause the particles rise into the riser section. The typical particle flow in CL technology occurs only when a large pressure difference is developed between Zones A and F. Since, the pressure difference in this case (2.6 m/sec) is within the range of 0-351 Pa (a very low-pressure difference), no high-volume fraction of particles happens from AR to riser section at zone-B.

By further increasing the velocity to 2.7 m/sec, a pressure peak-C (yellow circle, Figure 42, Figure 43) appeared and the pressure within the system ranged from 101325-108157 Pa (maximum pressure was observed at 1111 sec) with a pressure difference between Zone-A and Zone-B being -9 Pa to 6439 Pa. The pressure difference observed was still lower in comparison to that at velocity ranges of 3.2-3.5 m/sec and therefore the volume fraction flowing through zone-B was 0.28 (related to pressure peak 1111 sec, Figure 42). The maximum pressure observed at velocity of 3.2 m/sec (Figure 42 blue circle-peak A, 1911 sec) within the time range 18-20 sec is 115717 Pa. This causes a very high-pressure difference between zones B and F, which results in the volume fraction of 0.56 (yellow dashed box, Figure 44).

At the maximum pressure applied to AR (3.5 m/sec), system's pressure difference reached the maximum value of 16488 Pa, which is the highest among all AR velocities applied from 2.6 m/sec to 3.5 m/sec. However, this pressure difference resulted in the maximum volume fraction of particles of 0.5 m, which is lower than that observed at AR at the velocity of 3.2 m/sec. Even, comparison of the pressure peaks and the particles volume fractions of the three velocities of 2.7, 3.2, and 3.5 m/sec at time interval of 10-12 sec, confirm that the maximum pressure peak of 1114058 (red circle-peak B, 1061 sec) ended with only 0.42 volume fraction of particles at Zone B. The value was lower than that for the AR inlet velocity of 3.2. It can be concluded that the velocity of 3.2 m/sec gives a moderate pressure value and its difference while still imparts maximum volume fraction of particle of 0.56 which is desirable, in comparison to 3.5 m/sec, which gives a very high-pressure values and its differences and yet, gives a low value of volume fraction, which is undesirable.

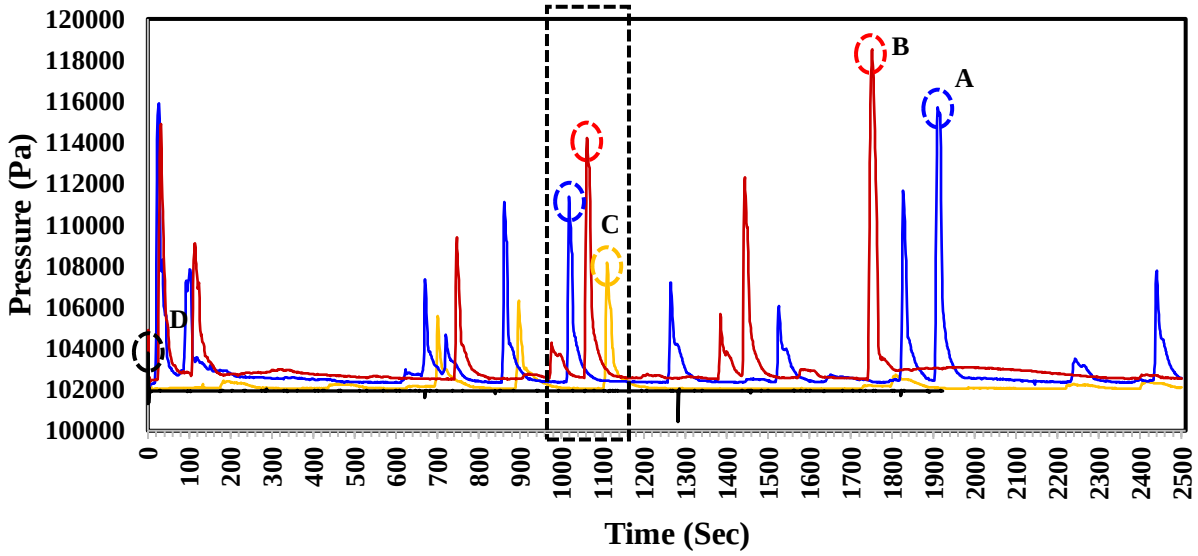

Figure 42. The graph between Pressure and time at ZONE-B for different velocities ▬ Avg(P_G) Vel_2.6, ▬ Avg(P_G) Vel_2.7, ▬ Avg(P_G) Vel_3.2, and ▬ Avg(P_G) Vel_3.5 for time intervals 0-25seconds.

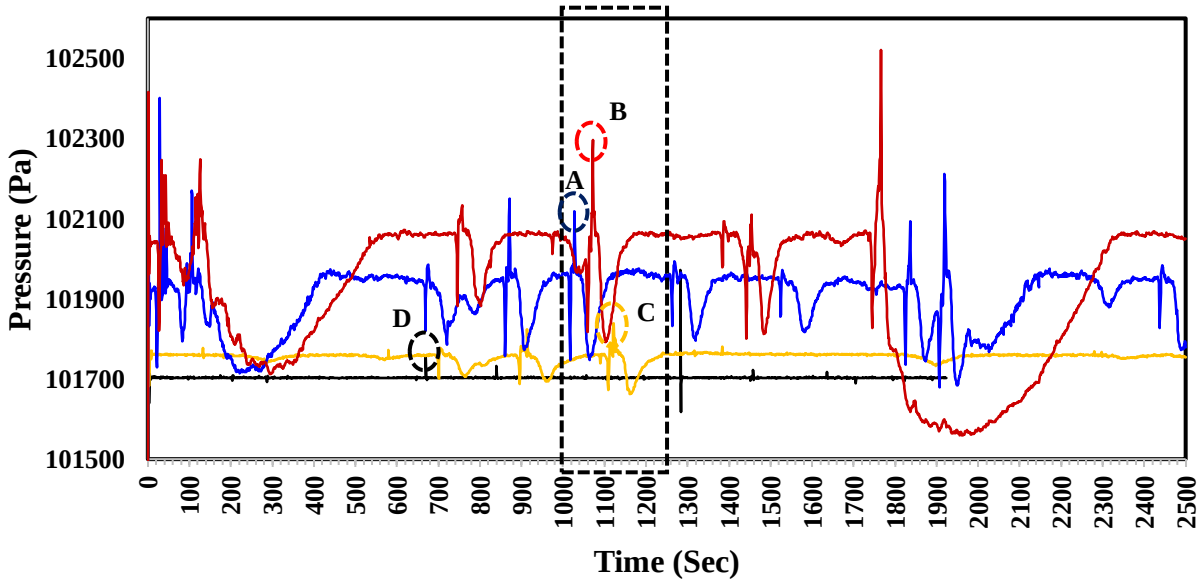

Figure 43. The graph between Pressure and time at ZONE-F for different velocities ▬ Avg(P_G) Vel_2.6, ▬ Avg(P_G) Vel_2.7, ▬ Avg(P_G) Vel_3.2, and ▬ Avg(P_G) Vel_3.5 for time intervals 0-25seconds.

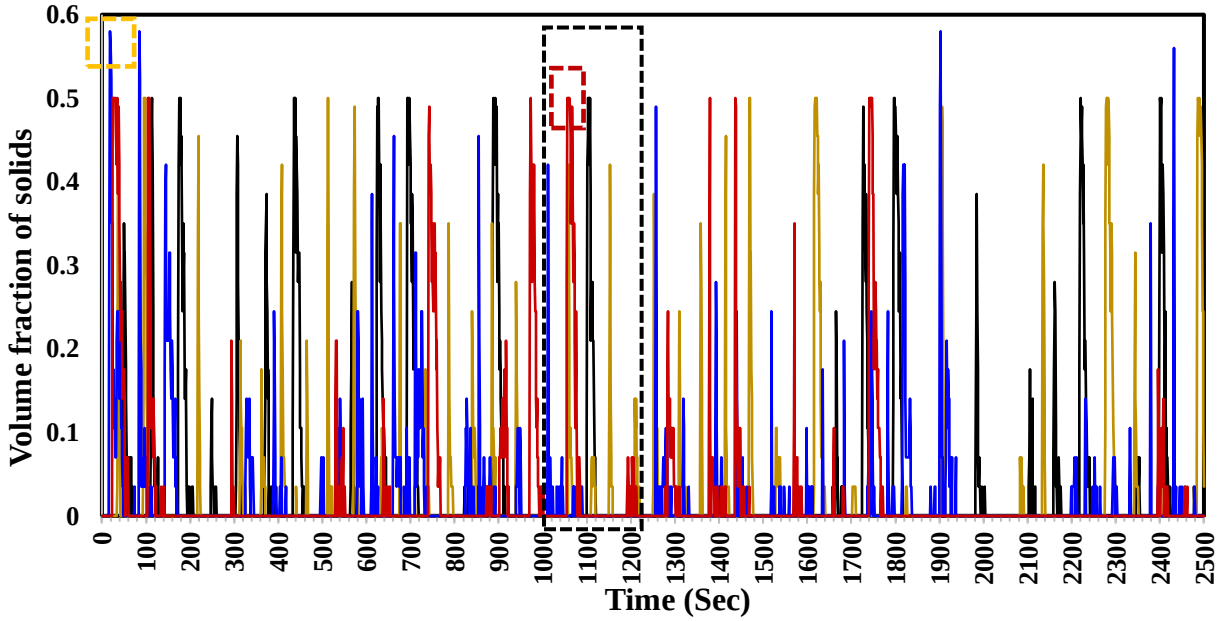

Figure 44. The graph between Volume fraction of Solids and time for different velocities. — Avg (EP_S) Vel_2.6, — Avg (EP_S) Vel_2.7, — Avg (EP_S) Vel_3.2, and — Avg (EP_S) Vel_3.5 between time intervals 0-25 second.

4.8 Impact of Mass flow rate in FR on Chemical Loop

The inlet mass flow rate of FR impacts the changes in pressure and the volume fraction of solids that flow through the loop. The range of mass flow rate used in this study is from 0.0025-0.1 kg/sec. The time interval of 0-7 sec indicated in this section is to a pressure peak highlighted in Figure 46 (dashed black box/circle). Region F (downcomer exit to FR) was considered to analyze the impact of variable mass flow rate. Figure 45 shows the velocity vectors for mass flow rate ranging between 0.0025-0.1 kg/sec, corresponding to the pressure peak highlighted in a solid circle, Figure 46.

The FR operates on a minimum mass flow rate to let the particles fluidize inside the reactor without any high turbulent zone (high-pressure peak). A typical flow inside the FR must have a stable pressure throughout the system. As explained in the previous section, a higher-pressure difference

between AR and FR increases volume fraction of particles flowing through the loop until the optimum value of AR's inlet velocity. Yet, a high mass flow rate inside the FR causes a backflow condition to the downcomer, which is undesirable. An optimum value of mass flow keeps the bed to a minimum fluidization, causes maximum transfer of particles into the connection loop and keep the chemical loop under circulation.

At a mass flow rate value of 0.0025 kg/sec, the pressure within the FR ranges between 101334-102421 Pa (Figure 46). The pressure values are stable (green line, Figure 46), which resulted in the volume fraction of 0.58 for the time interval 0-25 sec. The direction of the velocity vectors (Figure 45a, 0.28 sec) confirms the typical fluidization pattern observed inside the FR. For mass flow rate 0.0075, the pressure ranges between 101325-103092 Pa (yellow circle, Figure 46), which is a stable range. The volume fraction of particles observed under this condition was 0.57 and the peaks (black dashed circle, Figure 47) fluctuate indefinitely throughout the time interval 0-25 sec. The highest mass flow rate applied (0.05-0.1 kg/sec) resulted in a predominant backflow pattern inside the FR-cyclone distributor channel (explained in the next section). The pressure value for 0.05 kg/sec ranges from 101325-116710 Pa with P_{max} 116710 Pa observed at 0.24 sec (blue circle, Figure 45). At such a high-pressure value, a backflow of particles flowing from FR into the cyclone distributor is witnessed (Figure 45d). Also, due to the backflow condition, the FR is emptied with particles in 21 sec, and it is validated from the reduction of the solids volume fraction which starts at 0.58 and ends at 0 (blue peaks, Figure 47). A similar backflow phenomenon (Figure 45e) is observed at 0.1 kg/sec and the P_{max} 147518 Pa (red circle, Figure 46) was noted at 0.14 sec. Also, the particles emptied the FR in 10.51 sec and can be validated from the volume fraction of particles which reduces from 0.58 to 0.

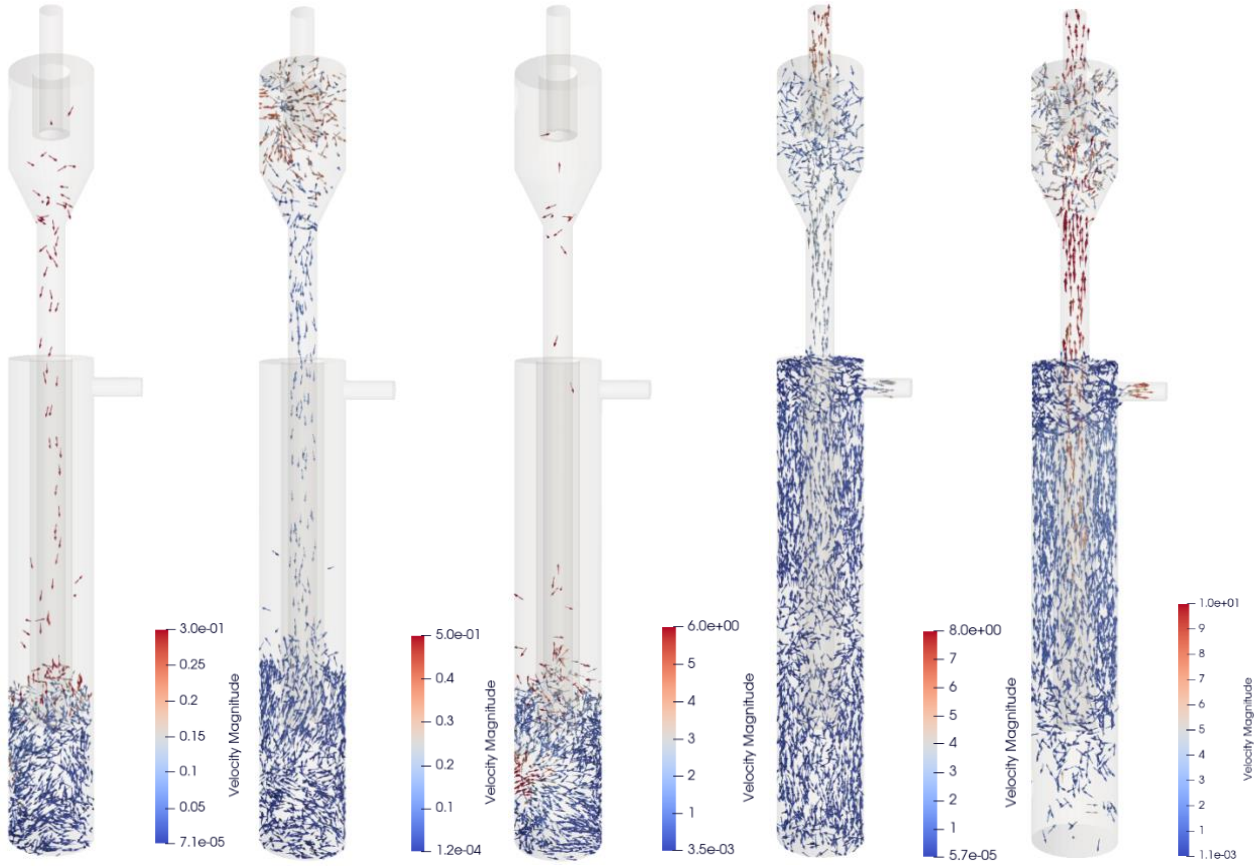

(a) 0.0025 Kg/sec (b) 0.0075Kg/sec (c) 0.01 Kg/sec (d) 0.05Kg/sec (e) 0.1Kg/sec

Figure 45. Circulation of catalytic solid particles inside the downcomer and FR. representing velocity vectors magnitude. Simulation condition: V.AR: 3.2 m/sec, Volume fraction of solid inside LC/AR/FR: 0.5.

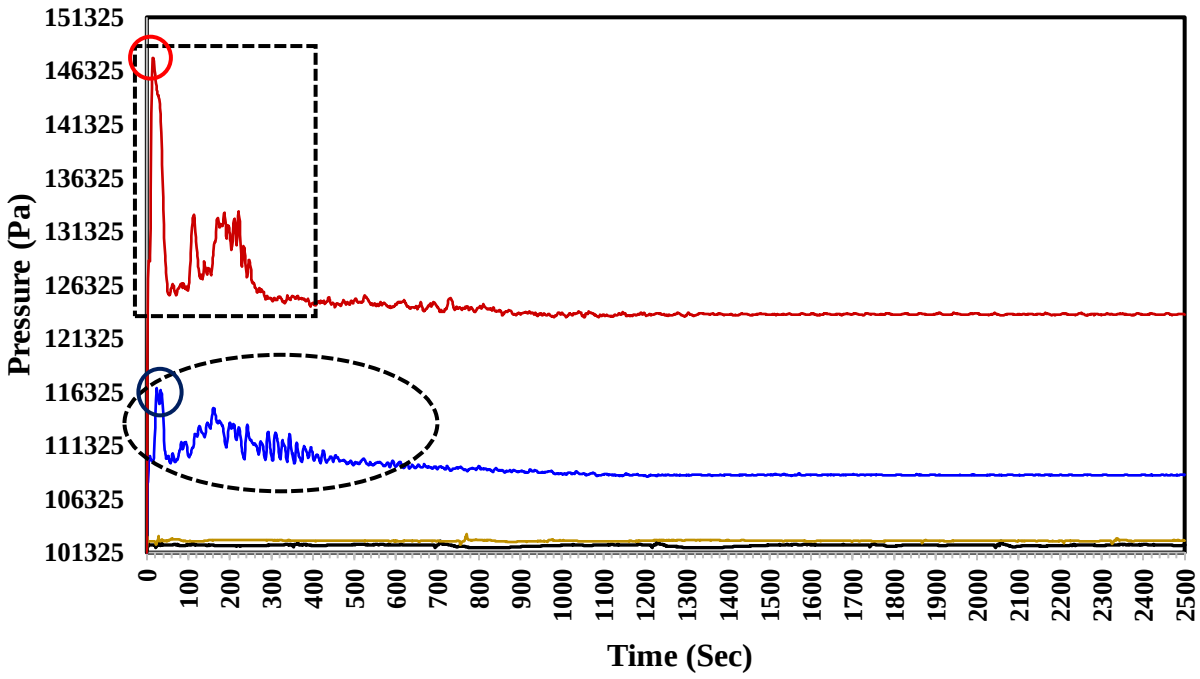

Figure 46. The graph between Pressure and time at zone-F for different mass flow rate — Avg(P_G) MFR_0.0025, — Avg(P_G) MFR_0.0075, — Avg(P_G) MFR_0.05, and — Avg(P_G) MFR_0.1 for time intervals 0-25seconds. Zone-F

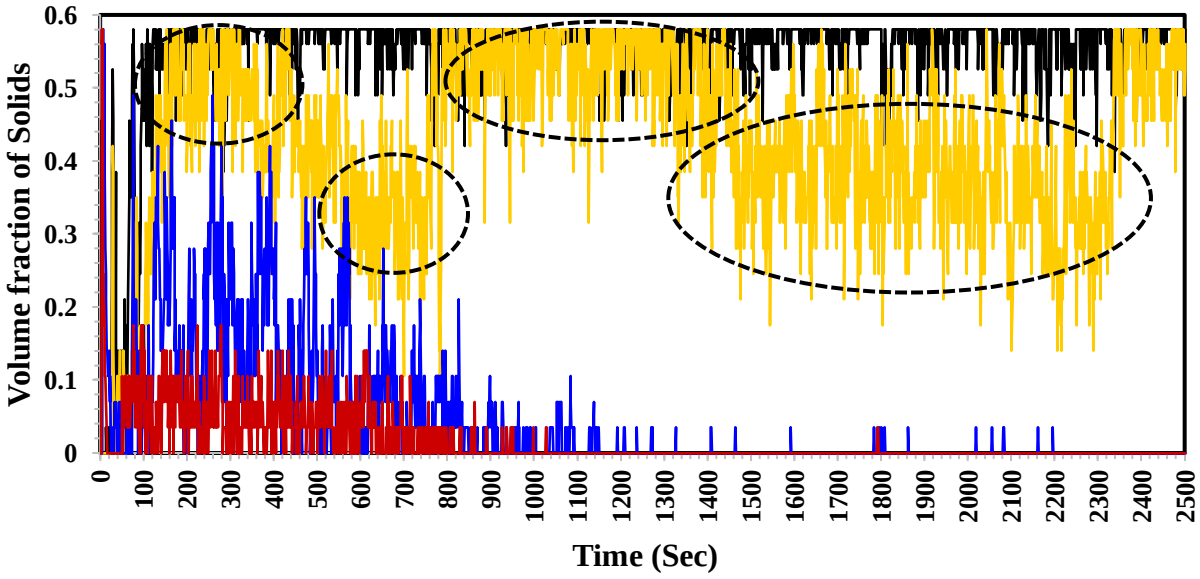

Figure 47. The graph between Volume fraction of Solids and time at zone-F for different mass flow rates — Avg (EP_S) MFR_0.0025, — Avg (EP_S) MFR_0.0075, — Avg (EP_S) MFR_0.05, and — Avg (EP_S) MFR_0.1 between time intervals 0-25 second.

4.9 Backflow inside FR

The pressure difference between the AR and FR maintains particle flow in the chemical loop. When a high mass flow rate is applied to the FR inlet, a mass flow inlet at FR counterbalances the high pressure developing inside AR and thus causes the backflow of particles through FR into a cyclone. Figure 48 shows the particle flow pattern at a gas inlet mass flow rate of 0.1 kg/sec in FR and gas inlet velocity of 3.2 m/sec in AR The time interval indicated in this section is to a pressure peak highlighted in Figure 49 (dotted black box), to explain the occurrence of backflow between Region E (inverted conical section of cyclone distributor) and Region F (exit riser tube inside FR). A typical direction of the granular flow in CL technology starts at FR into the connection loop, then into the AR through the riser, and finally into the cyclone distributor into the downcomer. The pressure condition under this steady flow condition is $P_{AR} > P_{FR}$. In this part, an abnormally high value of mass flow rate ranging between 0.05-0.1 kg/sec was considered to analyze the change in flow pattern. At 0.1 sec, the commencement of the backflow is observed through the direction of velocity vectors (Figure 48a) pointing upwards. At the same time, a void begins to develop inside the FR as noted in Figure 48a/b. The pressure at 0.1 sec was noted inside zone-E and zone-F are 107537 Pa and 110054 Pa respectively, where P_{FR} (Zone-F) > P_{CD} (Zone-E). In a typical steady flow condition, the pressure inside the cyclone distributor (P_{CD}) is greater than the pressure inside the FR (P_{FR}). A reverse behavior ($P_{FR} > P_{CD}$) is observed under the backflow case, Figure 49.

At 0.15 sec, the particles are observed to fluidize inside the FR as well as enter the downcomer as confirmed by the direction of velocity vectors (Figure 48a). Moreover, P_{FR} (Zone-F) is larger than P_{CD} (Zone-E) (P_{CD}=107556 Pa and P_{FR}=109862 Pa). The particles enter the cyclone distributor through the reversed direction intended in downcomer (Figure 48a, 0.25 sec) and the void space

begins to expand (Figure 48a/b, blue/yellow dashed circle). Consequently, the particles filling the CD begin to exit through the outlet of the cyclone distributor and fuel reactor (yellow dotted circle, Figure 48a). As a result, the volume fraction of solids reduces from time 0-25 sec (Figure 50). Once the majority of the particles left the cyclone distributor (0.53 sec), the hydrostatic pressure created by the particles in the cyclone causes a pressure drop inside the FR, and the particles inside the FR start to flow in the downward direction (blues dashed box, Figure 48a). Meanwhile, the particles enter the cyclone distributor from the AR riser tube, as expected in a typical flow pattern in CL technology under S.S. condition. Similarly, the flow pattern observed in the FR is like what was explained in the section low pattern inside FR. The particles continue to exit the outlets (Figure 48a, 0.88 sec) while the volume fraction of particles keeps reducing (Figure 50). Finally, due to this high mass flow rate, the volume fraction of particles is reduced from 0.58 to 0.03 (Figure 50), and the cyclone distributor is emptied while the FR keeps fluidizing with a minimum volume fraction of 0.03, which is consequently emptied.

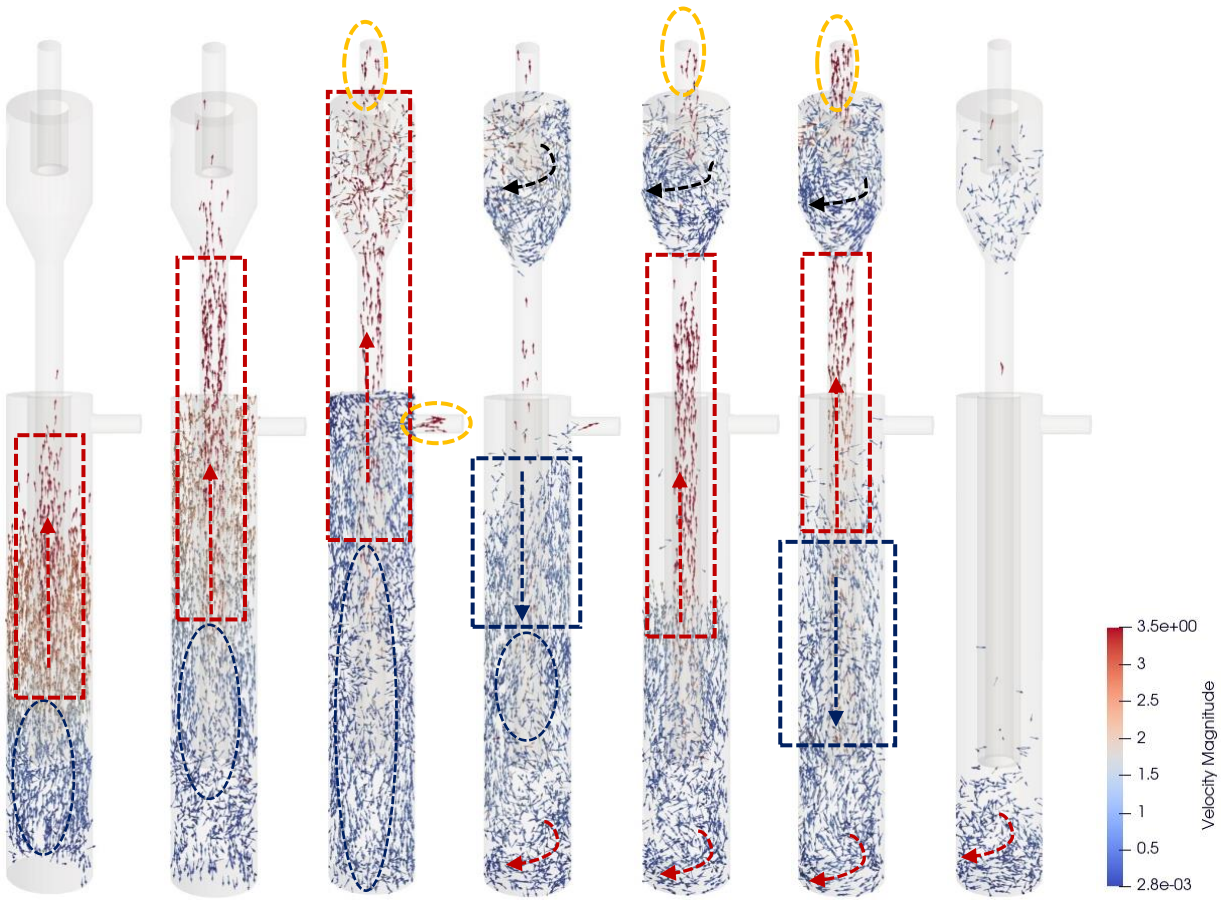

0.1 sec 0.15 sec 0.25 sec 0.53 sec 0.88 sec 1.25 sec 14.20 sec

(a)

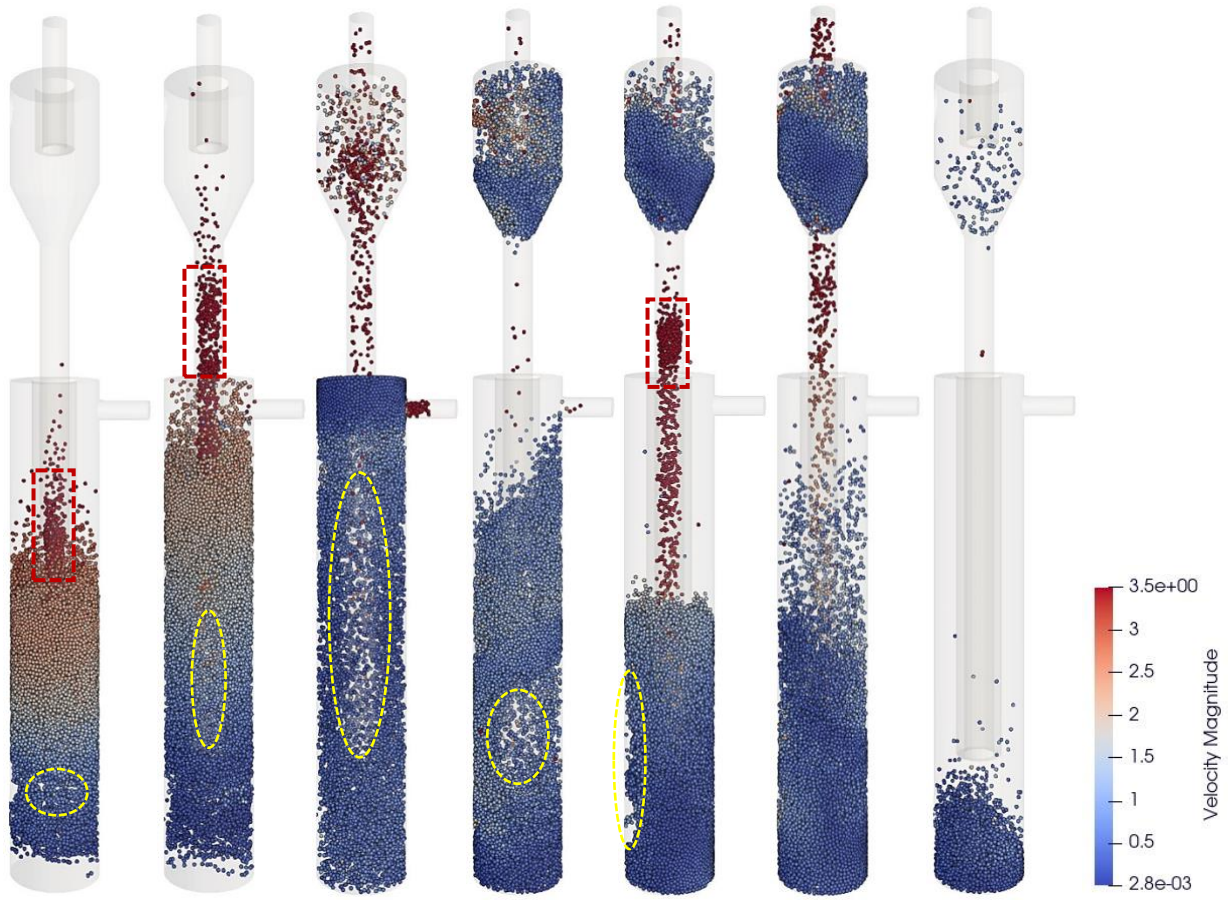

0.1 sec 0.15 sec 0.25 sec 0.53 sec 0.88 sec 1.25 sec 14.20 sec

(a)

Figure 48. Circulation of catalytic solid particles inside the downcomer and FR. depicting backflow condition. a) Velocity vectors magnitude, b) Particle velocity magnitude. Simulation condition: V.AR: 3.2 m/sec, MFR_{FR}: 0.05 kg/sec, Volume fraction of solid inside LC/AR/FR: 0.5

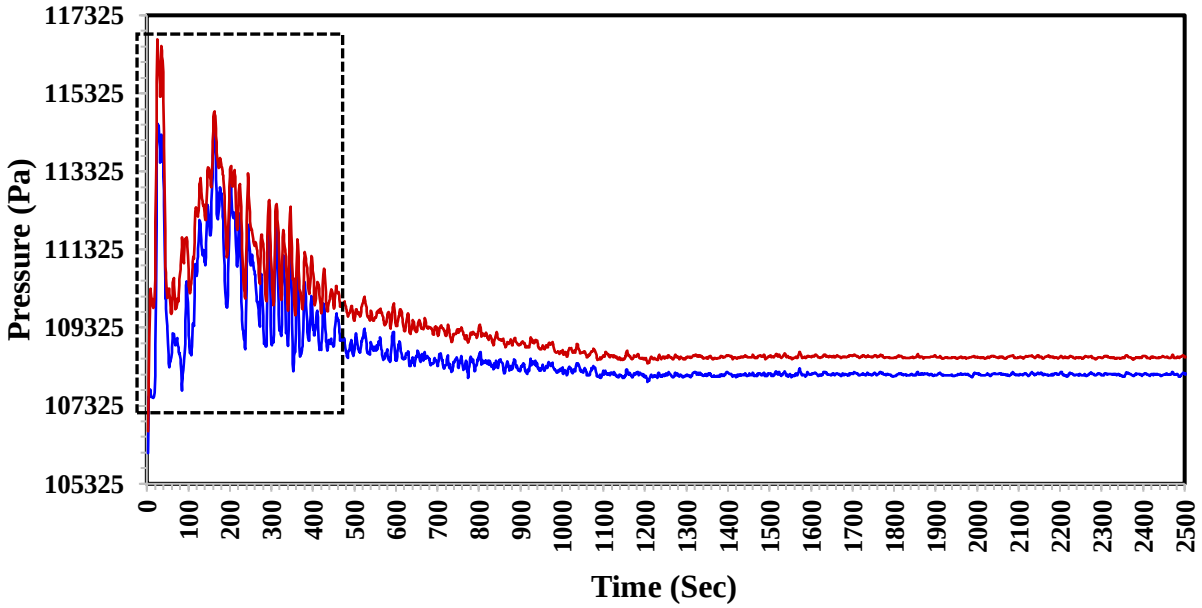

Figure 49. The graph between Pressure and time at different zones — Avg(P_G) Zone-E and — Avg(P_G) Zone-F for time intervals 0-25seconds.

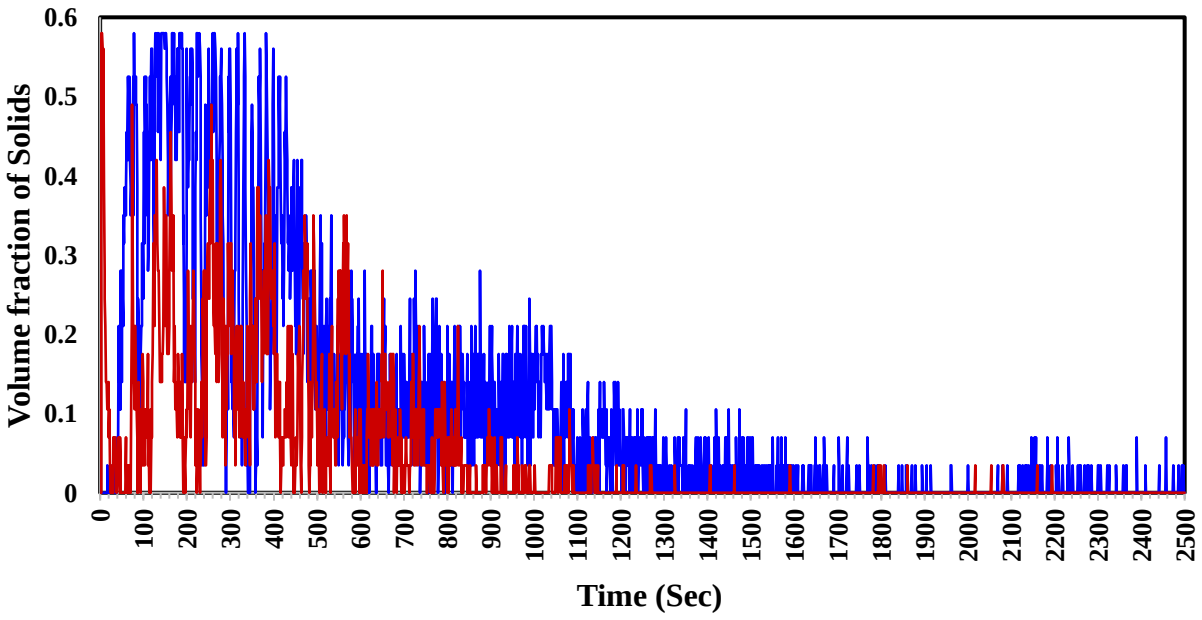

Figure 50. The graph between Volume fraction of Solids and time at different zones — Avg (EP_S) Zone-E and — Avg (EP_S) Zone-F between time intervals 0-25 second.

4.10 Geometric Modification

4.10.1 Impact of variable Connection Loop diameter

The diameter of connection loop impacts the changes in pressure and the volume fraction of solids that flow through the loop. The range of diameter used in this study is from 25-40 mm. The time interval of 17-19 sec indicated in this section is to a pressure peak highlighted in Figure 51 and Figure 52 (dashed black box). Region B (AR conical section) and Region F (downcomer exit to FR) was considered to analyze the impact of variable connection loop diameter. Figure 53 shows the volume fraction of solids rising through the region-B.

First, the impact of different connection loop diameter on a looping system is the number of high-volume fraction fluidization that occur from AR into the riser section. In a chemical looping technology, the pressure must stabilize in order to reach steady state condition. The particles must have sufficient reaction time inside both AR and FR to let the redox reaction to complete before the particles are transferred inside the loop. The ideal flow pattern explained in the previous sections should occur in timely manner and the large number of these chemical looping cycles are undesirable as it impacts reaction kinetics. The increase in the diameters from 25-40 mm increases the number of chemical looping cycle and decrease the system stability.

At 25 mm (Figure 51, black pressure line), the pressure within the system ranges from 101325-116750 Pa (Figure 51, peak D, t: 6.98 sec). The number of cycles observed between the time interval 0-25 sec are 10 cycles. The average pressure difference between the region-B and region-F is observed to be 1159 Pa while the maximum pressure difference was observed to be 14781 Pa. As the average difference in pressure increases inside the looping system, the number of cycles is

found to increase (explained for other values of diameter). Although the maximum pressure in this study is found to be 116750 Pa which corresponds to d_{CL} of 25 mm, the corresponding maximum pressure inside the FR is as low as 102415 Pa (peak-d, Figure 52).

At diameter of 30 mm (Figure 51, yellow pressure line), the pressure within the system ranges from 101325-116623 Pa (Figure 51, peak C, 9.48 sec). The number of cycles observed between the time interval 0-25 sec increased to 15 cycles. The average and maximum pressure difference between the Region-B and Region-F is observed to be 1266 and 14634 Pa, respectively. Although the maximum pressure difference between the diameters of 25 mm and 30 mm is 147 Pa (a very low-pressure difference), the number of cycles increased by a value of 5. Also, the maximum volume fraction of particles flowing through the loop for 25 mm and 30 mm are found to be 0.58 (Figure 53) and the increase in diameter by 5 mm does not cause a significant change.

The pressure range as observed from Figure 51 (at zone-B, blue pressure line) for d_{CL} of 35 mm is 101325-115896 Pa (peak-B, t:17.20 sec). The corresponding maximum pressure inside the FR at region-F is 102478 Pa (peak-B, blue dashes circle) which is higher than the value observed at 30 mm and 25 mm. It can be confirmed maximum pressure inside the FR (region F) increases with the diameter of the connection loop. Because of this trend, it takes a shorter time for the chemical loop to stabilize, which subsequently increases the number of cycles which in this case is 18 cycles (which is undesirable). There is not any increase in the volume fraction of particles flowing through region B, as 0.58 is observed as the maximum volume fraction flowing through the loop for all sets of diameters selected.

For 40 mm (Figure 51, red pressure line), the pressure within the system ranges from 101325-115447 Pa (Figure 51, peak A, 5.63 sec). The number of cycles observed between the time interval 0-25 sec further increase to 20 cycles. The average and maximum pressure difference between the region-B and region-F is observed to be 1449 Pa and 13443 Pa, respectively. At d_{CL} 35 mm, the average pressure difference was 1418 Pa, while the maximum pressure was found to be 13895 Pa. Consistent with the previous trend, the number of cycles of particles flowing through the loop increased to 21 cycles (total number of red pressure peaks).

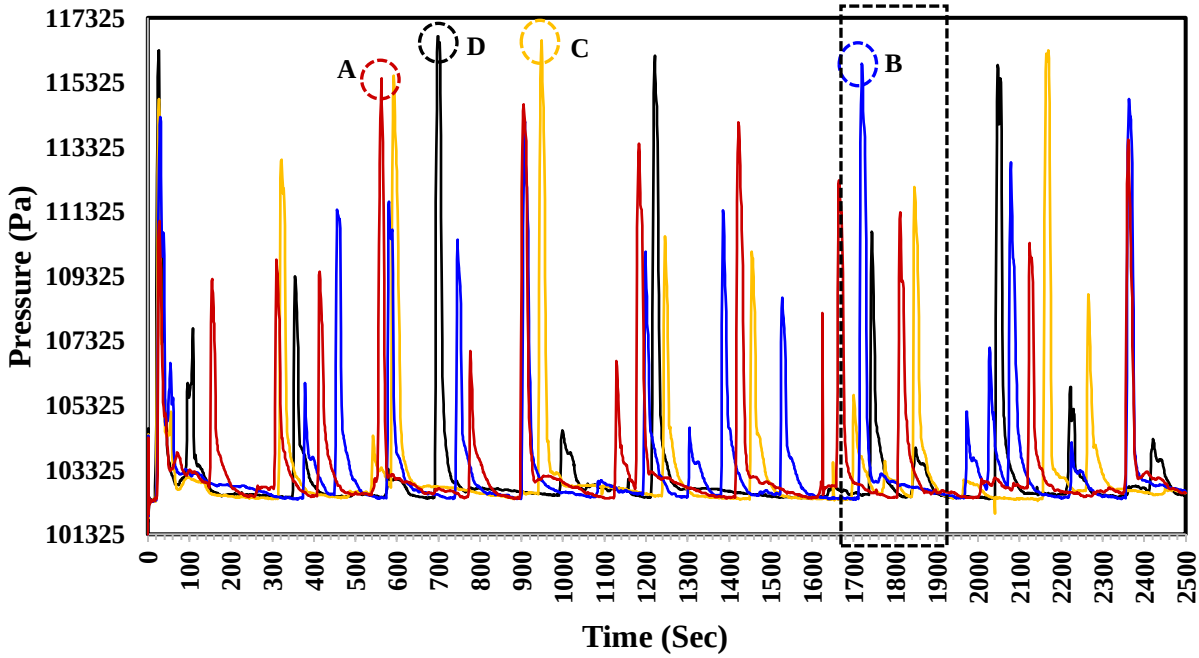

Figure 51. The graph between Pressure and time at ZONE-B for different velocities ▬ Avg(P_G) 25mm, ▬ Avg(P_G) 30mm, ▬ Avg(P_G) 35mm, and ▬ Avg(P_G) 40mm for time intervals 0-25seconds.

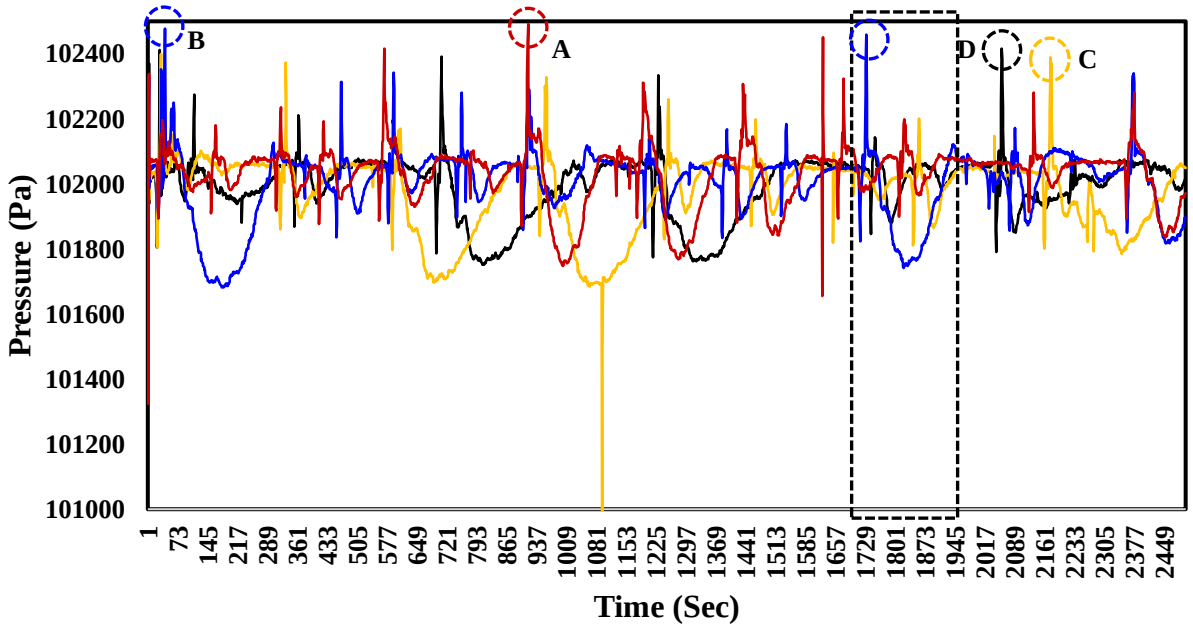

Figure 52. The graph between Pressure and time at ZONE-F for different velocities — Avg(P_G) 25mm, — Avg(P_G) 30mm, — Avg(P_G) 35mm, and — Avg(P_G) 40mm for time intervals 0-25seconds.

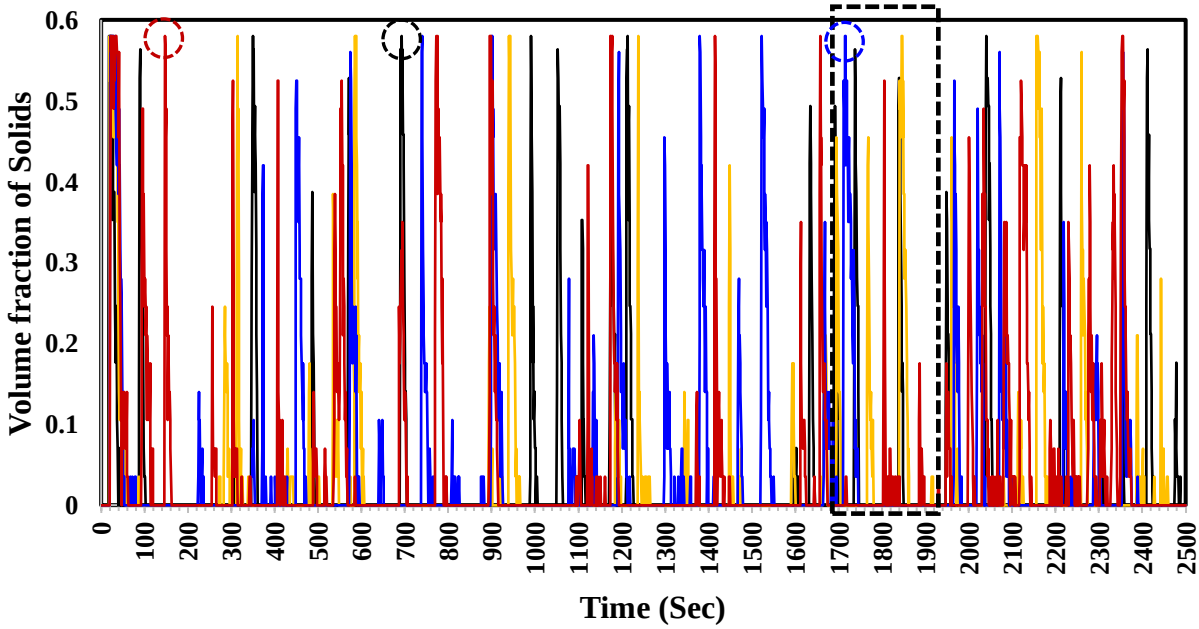

Figure 53. The graph between Volume fraction of Solids and time at Zone-B for different velocities — Avg (EP_S) 25mm, — Avg (EP_S) 30mm, — Avg (EP_S) 35mm, and — Avg (EP_S) 40mm between time intervals 0-25 second.

CHAPTER 5: VALIDATION OF SIMULATION RESULTS

Minimum fluidization velocity

The phenomenon of fluidization occurs when an upward-flowing gas applies sufficient drag force on particles to balance the gravitational force, causing the particles to behave like a fluid. The degree of fluidization affects the local gas velocity around the particles due to the drag forces (Anantharaman et al., 2018). This effect is generally insignificant for spherical particles but can be significant for particles with irregular shapes (Coltters & Rivas, 2004).

In this study, particles with a diameter of dp=3mm, a density of ρs=2400 Kg/m3, and a particle volume fraction of 0.5 were used. The minimum fluidization velocity was estimated using empirical calculations based on the following correlation, which yielded a value of 2.57m/sec:

$$\mathrm{umf} = \mathrm{C} \times (\rho_g - \rho_p) \times g \times dp^2 / 18\mu \quad (44)$$

where umf is the minimum fluidization velocity, C is a dimensionless constant (typically between 1.4 and 1.8), ρg is the density of the gas, ρp is the density of the particle, g is the acceleration due to gravity, dp is the particle diameter, and μ is the viscosity of the gas.

It was observed in section 4.3.1 that insufficient kinetic energy imparted to the particles resulted in a fluidization pattern without rising in the riser section. Furthermore, numerical simulations showed that at a velocity of 2.6 m/sec, the particles followed a minimum fluidization trend, as evidenced by figures 42-43 (black pressure peaks). These results suggest that the minimum fluidization velocity for the given system is approximately 2.6 m/sec. These findings underscore the significance of accurately determining the minimum fluidization velocity for optimizing gas-solid fluidization processes.

Formation of clusters

Particle clusters are widely recognized as significantly impacting the hydrodynamics and overall performance of gas-solid fluidized beds. In gas-solid fluidization systems, particles exist as individual particles and clusters or agglomerates (groups of particles). It is important to distinguish between particle clusters and particle agglomerates (Cahyadi et al., 2017). Particle clusters arise from hydrodynamic effects and weak inter-particle forces, whereas particle agglomerates result from strong inter-particle bonding (Cocco et al., 2010).

The formation of particle clusters during a pulsed flow, as depicted in Figure 35 (Section A and Section B), validates the particle flow pattern observed in this study. During each pulse, a similar clustering trend was observed, confirming the general flow characteristics inside the riser section of a circulating fluidized bed reactor. This observation highlights the importance of understanding particle clustering behavior for the optimization of gas-solid fluidization processes.

CHAPTER 6: CONCLUSIONS

While well-established, traditional hydrogen generation systems such as SMR emit considerable volumes of carbon dioxide (CO_2) as a byproduct. Dry reforming of methane is a potentially beneficial process since it employs CO_2 as a reducing agent, but it has certain downsides, including catalyst deactivation by coke and yield limitations due to thermodynamic equilibrium. These drawbacks may be offset by better fluidized bed reactors and chemical looping technologies. Due to the economic restrictions of building reactors without understanding the solid-fluid interaction, three-dimensional numerical modeling is a means to lower early costs while also improving particle physics understanding.

Our preliminary findings in this study explain the hydrodynamics of a chemical looping fluidized bed reactor through a three-dimension model using Eulerian-Lagrangian approach in a transient timeframe (25 sec). The fluid flow pattern of particles in fuel reactor, connection loop, air reactor, cyclone distributor, and downcomer were discussed in detail. In addition, the impacts of velocity inlet values in both fuel and air reactors and the loop connect diameter were explored. It was observed that the two looped fluidized bed develop a periodic pulse pattern. The 3D results showed that solid particles develop an extremely complicated pulse turbulent flow in the CL system. Every pulse is accompanied by a series of phenomena including a pressure asymmetry between the reduction and oxidation zones, a reverse flow between these two zones and formation of vortices, or swirling patterns in reduction zone all of which happen in a milli second; and that every pulse carries a certain amount of solid particulates in the form of solid particles clusters. After analyzing the flow patterns, pressure contours and operating parameters, ideal parameters were concluded to be AR velocity of 3.2 m/sec, FR mass flow rate of 0.0025 kg/sec and diameter of connection loop

of 25 mm. The optimal settings were determined after examining the flow patterns, pressure contours, and operational characteristics to determine an optimum geometrical configuration.

Nomenclature

ΔH	Enthalpy change
$\bar{\bar{\tau}}_g$	Fluid viscous stress tensor
g	Gravitational acceleration
p	Static pressure
ν_g	Velocity vector
ρ_g	Gas density
φ_g	Gas phase volume fraction
φ_f	Fluid phase volume fraction
F_{DEM}	External force by moving particles
μ	Gas dynamic viscosity
μ_t	Turbulent viscosity
$\bar{\bar{I}}$	Unit I tensor
k	Turbulent energy
ϵ	Turbulent dissipation rate
ρ_m	Mixture density
$\overrightarrow{\nu_m}$	Mixture velocity
$\overrightarrow{\nu_p}$	Average velocity of particles
β	Redistribution term
$\Delta\nu_g$	Gas fluctuating velocity
C_μ	Turbulence model constant
$\Delta\nu_p$	Particle fluctuating velocity
τ_I	Time scale of the Lagrangian for the gas phase
τ_d	Time scale of response for the particle phase
β	Inter–phase momentum exchange coefficient
C_{D0}	Standard drag coefficient
m_i	i-th particle's mass
v_i	i-th particle's velocity
I_i	i-th particle's moment of inertia
ω_i	i-th particle's angular velocity
$F_{h,i}$	Hydrodynamic force
$F_{g,i}$	Gravity forces
$F_{k,i}$	Cohesive/adhesive
$T_{c,\,ij}$	Torque contributions non-collinear collisions
$T_{r,\,ij}$	Rolling friction torque
T_{fp}	Fluid-particle torque
δ's	Displacements between the contacting particles
ν	Relative velocity
K	Spring stiffness constants
η	Dashpot damping coefficient
e_n	Coefficient of restitution
η_n	Damping coefficient
E_{eq}	Equivalent properties
F_{ct}	Coulomb's sliding limit tangential contribution of the force

Reference

Anantharaman, A., Cocco, R. A., & Chew, J. W. (2018). Evaluation of correlations for minimum fluidization velocity (Umf) in gas-solid fluidization. *Powder Technology*, *323*, 454-485. https://doi.org/https://doi.org/10.1016/j.powtec.2017.10.016

Aouad, S., Labaki, M., Ojala, S., Seelam, P. K., Turpeinen, E., Gennequin, C., Estephane, J., & Abi-Aad, E. (2018). A Review on the Dry Reforming Processes for Hydrogen Production: Catalytic Materials and Technologies. In (pp. 60-128). https://doi.org/10.2174/9781681087580118020007

Armor, J. N. (1999). The multiple roles for catalysis in the production of H2. *Applied Catalysis A: General*, *176*(2), 159-176. https://doi.org/https://doi.org/10.1016/S0926-860X(98)00244-0

Bandara, J., Jayarathna, C., Thapa, R., Nielsen, H., Moldestad, B., & Eikeland, M. (2020). Loop seals in circulating fluidized beds – Review and parametric studies using CPFD simulation. *Chemical Engineering Science*, *227*, 115917. https://doi.org/10.1016/j.ces.2020.115917

Bandara, J. C., Jayarathna, C., Thapa, R., Nielsen, H. K., Moldestad, B. M. E., & Eikeland, M. S. (2020). Loop seals in circulating fluidized beds – Review and parametric studies using CPFD simulation. *Chemical Engineering Science*, *227*, 115917. https://doi.org/https://doi.org/10.1016/j.ces.2020.115917

Bartocci, P., Abad, A., Cabello, A., de las Obras Loscertales, M., Lu, W., Yang, H., & Fantozzi, F. (2022). CFD Modelling of the Fuel Reactor of a Chemical Loping Combustion Plant to Be Used with Biomethane. *Processes*, *10*(3).

Cabello, A., Abad, A., de las Obras Loscertales, M., Bartocci, P., García-Labiano, F., & de Diego, L. F. (2023). Exploring design options for pressurized chemical looping combustion of natural gas. *Fuel*, *342*, 126983. https://doi.org/https://doi.org/10.1016/j.fuel.2022.126983

Cahyadi, A., Anantharaman, A., Yang, S., Karri, S. B. R., Findlay, J. G., Cocco, R. A., & Chew, J. W. (2017). Review of cluster characteristics in circulating fluidized bed (CFB) risers. *Chemical Engineering Science*, *158*, 70-95. https://doi.org/https://doi.org/10.1016/j.ces.2016.10.002

Carapellucci, R., & Giordano, L. (2020). Steam, dry and autothermal methane reforming for hydrogen production: A thermodynamic equilibrium analysis. *Journal of Power Sources*, *469*, 228391. https://doi.org/https://doi.org/10.1016/j.jpowsour.2020.228391

Cheng, Y., Lien, F.-S., Yee, E., & Sinclair, R. (2003). A comparison of large Eddy simulations with a standard k– ε Reynolds-averaged Navier–Stokes model for the prediction of a fully developed turbulent flow over a matrix of cubes. *Journal of Wind Engineering and Industrial Aerodynamics - J WIND ENG IND AERODYN*, *91*, 1301-1328. https://doi.org/10.1016/j.jweia.2003.08.001

Chibane, L., & Djellouli, B. (2011). Methane Steam Reforming Reaction Behaviour in a Packed Bed Membrane Reactor. *International Journal of Chemical Engineering and Applications*, *2*, 147-156. https://doi.org/10.7763/IJCEA.2011.V2.93

Cocco, R., Shaffer, F., Hays, R., Reddy Karri, S. B., & Knowlton, T. (2010). Particle clusters in and above fluidized beds. *Powder Technology*, *203*(1), 3-11. https://doi.org/https://doi.org/10.1016/j.powtec.2010.03.023

Coltters, R., & Rivas, A. L. (2004). Minimum fluidation velocity correlations in particulate systems. *Powder Technology*, *147*(1), 34-48. https://doi.org/https://doi.org/10.1016/j.powtec.2004.06.013

Cormos, C.-C. (2020). Energy and cost efficient manganese chemical looping air separation cycle for decarbonized power generation based on oxy-fuel combustion and gasification. *Energy*, *191*, 116579. https://doi.org/https://doi.org/10.1016/j.energy.2019.116579

Czakiert, T., Krzywanski, J., Zylka, A., & Nowak, W. (2022). Chemical Looping Combustion: A Brief Overview. *Energies*, *15*(4).

de Diego, L. F., Ortiz, M., García-Labiano, F., Adánez, J., Abad, A., & Gayán, P. (2009). Hydrogen production by chemical-looping reforming in a circulating fluidized bed reactor using Ni-based oxygen carriers. *Journal of Power Sources*, *192*(1), 27-34. https://doi.org/https://doi.org/10.1016/j.jpowsour.2008.11.038

Deng, Y., Zhang, L., Hou, H., Yu, B., & Sun, D. (2019). Modeling and simulation of the gas-liquid separation process in an axial flow cyclone based on the Eulerian-Lagrangian approach and surface film model. *Powder Technology*, *353*, 473-488. https://doi.org/https://doi.org/10.1016/j.powtec.2019.05.039

Di Giuliano, A., Capone, S., Anatone, M., & Gallucci, K. (2022). Chemical Looping Combustion and Gasification: A Review and a Focus on European Research Projects. *Industrial & Engineering Chemistry Research*, *61*(39), 14403-14432. https://doi.org/10.1021/acs.iecr.2c02677

Elbadawi, A. H., Ge, L., Li, Z., Liu, S., Wang, S., & Zhu, Z. (2021). Catalytic partial oxidation of methane to syngas: review of perovskite catalysts and membrane reactors. *Catalysis Reviews*, *63*(1), 1-67. https://doi.org/10.1080/01614940.2020.1743420

Erlach, B., Schmidt, M., & Tsatsaronis, G. (2011). Comparison of carbon capture IGCC with pre-combustion decarbonisation and with chemical-looping combustion. *Energy*, *36*(6), 3804-3815. https://doi.org/https://doi.org/10.1016/j.energy.2010.08.038

Ge, H., Guo, W., Song, T., & Xiao, J. (2015). Biomass Gasification using Chemical Looping in a 25kWth Reactor with Natural Hematite as Oxygen Carrier. *Chemical Engineering Journal*, *286*. https://doi.org/10.1016/j.cej.2015.10.092

Gu, J., Shao, Y., Liu, X., Zhong, W., & Yu, A. (2018). Modelling of particle flow in a dual circulation fluidized bed by a Eulerian-Lagrangian approach. *Chemical Engineering Science*, *192*, 619-633. https://doi.org/https://doi.org/10.1016/j.ces.2018.08.008

Hadjipaschalis, I., Poullikkas, A., & Efthimiou, V. (2009). Overview of current and future energy storage technologies for electric power applications. *Renewable and Sustainable Energy Reviews*, *13*(6), 1513-1522. https://doi.org/https://doi.org/10.1016/j.rser.2008.09.028

Halabi, M., Croon, M. H. J. M., Schaaf, J., Cobden, P., & Schouten, J. (2008). Modeling and analysis of autothermal reforming of methane to hydrogen in a fixed bed reformer. *Chemical Engineering Journal*, *137*, 568-578. https://doi.org/10.1016/j.cej.2007.05.019

Hossain, M. M., & de Lasa, H. I. (2008). Chemical-looping combustion (CLC) for inherent CO2 separations—a review. *Chemical Engineering Science*, *63*(18), 4433-4451. https://doi.org/https://doi.org/10.1016/j.ces.2008.05.028

Hu, J., Galvita, V., Poelman, H., & Marin, G. (2018). Advanced Chemical Looping Materials for CO2 Utilization: A Review. *Materials*, *11*, 1187. https://doi.org/10.3390/ma11071187

Index. (2014). In A. Basile & A. Iulianelli (Eds.), *Advances in Hydrogen Production, Storage and Distribution* (pp. 525-546). Woodhead Publishing. https://doi.org/https://doi.org/10.1016/B978-0-85709-768-2.50023-7

Ishida, M., Zheng, D., & Akehata, T. (1987). Evaluation of a chemical-looping-combustion power-generation system by graphic exergy analysis. *Energy*, *12*, 147-154.

Iulianelli, A., & Basile, A. (2014). *Advances in Hydrogen Production, Storage and Distribution*. Elsevier Science. https://books.google.com/books?id=85hzAwAAQBAJ

Kang, D., Lim, H. S., & Lee, J. W. (2020). Mesoporous Fe2O3–CeO2–Al2O3 Oxygen Carrier for Chemical Looping Dry Reforming with Subsequent Water Splitting. *Industrial & Engineering Chemistry Research*, *59*(36), 15912-15920. https://doi.org/10.1021/acs.iecr.0c03197

Khan, M. N., & Shamim, T. (2016). Investigation of hydrogen generation in a three reactor chemical looping reforming process. *Applied Energy*, *162*, 1186-1194. https://doi.org/https://doi.org/10.1016/j.apenergy.2015.08.033

Kolbitsch, P., Pröll, T., Bolhar-Nordenkampf, J., & Hofbauer, H. (2009). Design of a Chemical Looping Combustor using a Dual Circulating Fluidized Bed (DCFB) Reactor System [https://doi.org/10.1002/ceat.200800378]. *Chemical Engineering & Technology*, *32*(3), 398-403. https://doi.org/https://doi.org/10.1002/ceat.200800378

Konan, N. D. A., & Huckaby, E. D. (2021). CFD investigation of low-attrition air-reactor designs for the NETL chemical-looping combustion reactor. *Powder Technology*, *391*, 142-156. https://doi.org/https://doi.org/10.1016/j.powtec.2021.06.010

Kothari, R., Buddhi, D., & Sawhney, R. L. (2008a). Comparison of environmental and economic aspects of various hydrogen production methods. *Renewable and Sustainable Energy Reviews*, *12*, 553-563. https://doi.org/10.1016/j.rser.2006.07.012

Kothari, R., Buddhi, D., & Sawhney, R. L. (2008b). Comparison of environmental and economic aspects of various hydrogen production methods. *Renewable and Sustainable Energy Reviews*, *12*(2), 553-563. https://doi.org/https://doi.org/10.1016/j.rser.2006.07.012

Kronberger, B., Johansson, E., Löffler, G., Mattisson, T., Lyngfelt, A., & Hofbauer, H. (2004). A Two-Compartment Fluidized Bed Reactor for CO2 Capture by Chemical-Looping Combustion [https://doi.org/10.1002/ceat.200402137]. *Chemical Engineering & Technology*, *27*(12), 1318-1326. https://doi.org/https://doi.org/10.1002/ceat.200402137

Lamb, J. J., Hillestad, M., Rytter, E., Bock, R., Nordgård, A. S. R., Lien, K. M., Burheim, O. S., & Pollet, B. G. (2020). Chapter | three - Traditional Routes for Hydrogen Production and Carbon Conversion. In J. J. Lamb & B. G. Pollet (Eds.), *Hydrogen, Biomass and Bioenergy* (pp. 21-53). Academic Press. https://doi.org/https://doi.org/10.1016/B978-0-08-102629-8.00003-7

Li, H., & Zhao, Z. (2009). Advancements in Development of Chemical-Looping Combustion: A Review. *International Journal of Chemical Engineering*, *2009*. https://doi.org/10.1155/2009/710515

Li, S., & Shen, Y. (2020). Numerical study of gas-solid flow behaviors in the air reactor of coal-direct chemical looping combustion with Geldart D particles. *Powder Technology*, *361*, 74-86. https://doi.org/https://doi.org/10.1016/j.powtec.2019.10.045

Li, S., & Shen, Y. (2021). CFD study of nonuniformity of gas-solid flow through a chemical looping combustion system with symmetrical series loops. *Powder Technology*, *387*, 108-124. https://doi.org/https://doi.org/10.1016/j.powtec.2021.04.008

Li, S., Zhuo, Y., & Shen, Y. (2023). Modelling of multiphase reactive flows in a full-loop coal-direct chemical looping combustor. *Chemical Engineering Journal*, *457*, 141306. https://doi.org/https://doi.org/10.1016/j.cej.2023.141306

Liu, K., Deluga, G., Bitsch-Larsen, A., Schmidt, L., & Zhang, L. (2009). Catalytic Partial Oxidation and Autothermal Reforming. In (pp. 127-155). https://doi.org/10.1002/9780470561256.ch3

Löfberg, A., Kane, T., Guerrero-Caballero, J., & Jalowiecki-Duhamel, L. (2017). Chemical looping dry reforming of methane: toward shale-gas and biogas valorization. *Chemical Engineering and Processing: Process Intensification*, *122*, 523-529. https://doi.org/https://doi.org/10.1016/j.cep.2017.05.003

Luo, M., Yi, Y., Wang, S., Wang, Z., Du, M., Pan, J., & Wang, Q. (2018). Review of hydrogen production using chemical-looping technology. *Renewable and Sustainable Energy Reviews*, *81*, 3186-3214. https://doi.org/https://doi.org/10.1016/j.rser.2017.07.007

Lyngfelt, A. (2020). Chemical Looping Combustion: Status and Development Challenges. *Energy & Fuels*, *34*(8), 9077-9093. https://doi.org/10.1021/acs.energyfuels.0c01454

Mantripragada, H. C., & Veser, G. (2021). Intensifying chemical looping dry reforming: Process modeling and systems analysis. *Journal of CO2 Utilization*, *49*, 101555. https://doi.org/https://doi.org/10.1016/j.jcou.2021.101555

Mattisson, T., Lyngfelt, A., & Leion, H. (2009). Chemical-looping with oxygen uncoupling for combustion of solid fuels. *International Journal of Greenhouse Gas Control*, *3*(1), 11-19. https://doi.org/https://doi.org/10.1016/j.ijggc.2008.06.002

Moghtaderi, B. (2010). Application of Chemical Looping Concept for Air Separation at High Temperatures. *Energy & Fuels*, *24*(1), 190-198. https://doi.org/10.1021/ef900553j

Momirlan, M., & Veziroglu, T. N. (2005). The properties of hydrogen as fuel tomorrow in sustainable energy system for a cleaner planet. *International Journal of Hydrogen Energy*, *30*, 795-802.

Muradov, N. (2008). Production of Hydrogen from Hydrocarbons. In (pp. 33-101). https://doi.org/10.1201/9781420045772.ch2

Muradov, N. Z., & Veziroğlu, T. N. (2005). From hydrocarbon to hydrogen–carbon to hydrogen economy. *International Journal of Hydrogen Energy*, *30*(3), 225-237. https://doi.org/https://doi.org/10.1016/j.ijhydene.2004.03.033

Nikolaidis, P., & Poullikkas, A. (2017a). A comparative overview of hydrogen production processes. *Renewable and Sustainable Energy Reviews*, *67*, 597-611. https://doi.org/https://doi.org/10.1016/j.rser.2016.09.044

Nikolaidis, P., & Poullikkas, A. (2017b). A comparative overview of hydrogen production processes. *Renewable and Sustainable Energy Reviews*, *67*(C), 597-611. https://EconPapers.repec.org/RePEc:eee:rensus:v:67:y:2017:i:c:p:597-611

Osman, M., Khan, M., Zaabout, A., Cloete, S., & Amini, S. (2021). Review of pressurized chemical looping processes for power generation and chemical production with integrated CO2 capture. *Fuel Processing Technology*, *214*, 106684. https://doi.org/10.1016/j.fuproc.2020.106684

Pen˜a, M. A., Gómez, J. P., & Fierro, J. L. G. (1996). New catalytic routes for syngas and hydrogen production. *Applied Catalysis A: General*, *144*(1), 7-57. https://doi.org/https://doi.org/10.1016/0926-860X(96)00108-1

Peng, Z., Doroodchi, E., Alghamdi, Y. A., Shah, K., Luo, C., & Moghtaderi, B. (2015). CFD–DEM simulation of solid circulation rate in the cold flow model of chemical looping systems. *Chemical Engineering Research and Design*, *95*, 262-280. https://doi.org/https://doi.org/10.1016/j.cherd.2014.11.005

Pröll, T., Bolhàr-Nordenkampf, J., Kolbitsch, P., & Hofbauer, H. (2010). Syngas and a separate nitrogen/argon stream via chemical looping reforming – A 140kW pilot plant study. *Fuel*, *89*, 1249-1256. https://doi.org/10.1016/j.fuel.2009.09.033

Rafi, M., Kolupula, A. P., Vadali V.S.S, S., & Varam, S. (2023). An overview of hydrogen generation by hydrolysis of Al and its alloys with the addition of carbon-based materials. *International Journal of Hydrogen Energy*. https://doi.org/https://doi.org/10.1016/j.ijhydene.2022.12.318

Richesson, S., & Sahimi, M. (2019). Hertz-Mindlin Theory of Contacting Grains and the Effective-Medium Approximation for the Permeability of Deforming Porous Media [https://doi.org/10.1029/2019GL083727]. *Geophysical Research Letters*, *46*(14), 8039-8045. https://doi.org/https://doi.org/10.1029/2019GL083727

Roshan Kumar, T., Mattisson, T., Rydén, M., & Stenberg, V. (2022). Process Analysis of Chemical Looping Gasification of Biomass for Fischer–Tropsch Crude Production with Net-Negative CO2 Emissions: Part 1. *Energy & Fuels*, *36*(17), 9687-9705. https://doi.org/10.1021/acs.energyfuels.2c00819

Rothenberg, G. (2013). Chemical Technology. An Integral Textbook. By Andreas Jess and Peter Wasserscheid. *Angewandte Chemie International Edition*, *52*(33), 8501-8502.

Rydén, M., Lyngfelt, A., & Mattisson, T. (2006). Synthesis gas generation by chemical-looping reforming in a continuously operating laboratory reactor. *Fuel*, *85*(12), 1631-1641. https://doi.org/https://doi.org/10.1016/j.fuel.2006.02.004

Rydén, M., Lyngfelt, A., & Mattisson, T. (2008). Chemical-Looping Combustion and Chemical-Looping Reforming in a Circulating Fluidized-Bed Reactor Using Ni-Based Oxygen Carriers. *Energy & Fuels*, *22*(4), 2585-2597. https://doi.org/10.1021/ef800065m

Sgouros, G. A., & Digkas, A.-G. (2021). Blue Hydrogen – A strong potential bridge between Europe, Middle East & North Africa Countries under the Green Deal strategy. *11*, 41-57.

Sharma, A., Al Dushaishi, M., & Nygaard, R. (2021). *Fixed Bit Rotary Drilling Failure Criteria Effect on Drilling Vibration* 55th U.S. Rock Mechanics/Geomechanics Symposium,

Sharma, A., Burak, T., Nygaard, R., Hellvik, S., Hoel, E., & Welmer, M. (2023). *Projection of Logging While Drilling Data at the Bit by Implementing Supervised Machine Learning Algorithm* SPE Oklahoma City Oil and Gas Symposium, https://doi.org/10.2118/213070-MS

Sharma, A., Iradukunda, P., Karami, H., McCoy, J. N., Podio, A. L., & Teodoriu, C. (2020). *Experimental Evaluation of a Prototype Centrifugal Packer-Type Downhole Separator* SPE Artificial Lift Conference and Exhibition - Americas, https://doi.org/10.2118/201147-MS

Snoeck, J.-W., Froment, G., & Fowles, M. (2002). Kinetic Evaluation of Carbon Formation in Steam/CO2-Natural Gas Reformers. Influence of the Catalyst Activity and Alkalinity. *1*(1). https://doi.org/doi:10.2202/1542-6580.1001 (International Journal of Chemical Reactor Engineering)

Spallina, V., Romano, M., Chiesa, P., & Lozza, G. (2013). Integration of Coal Gasification and Packed Bed CLC process for High Efficiency and Near-zero Emission Power Generation. *Energy Procedia*, *37*, 662-670. https://doi.org/10.1016/j.egypro.2013.05.154

Steinberg, M., & Cheng, H. C. (1989). Modern and prospective technologies for hydrogen production from fossil fuels. *International Journal of Hydrogen Energy*, *14*(11), 797-820. https://doi.org/https://doi.org/10.1016/0360-3199(89)90018-9

Subhodeep, B., & Ramesh, K. A. (2016). Numerical Simulation of Chemical Looping and Calcium Looping Combustion Processes for Carbon Capture. In G. K. Konstantinos & S. Jan (Eds.), *Developments in Combustion Technology* (pp. Ch. 11). IntechOpen. https://doi.org/10.5772/63520

Sun, L., Lin, J., Kong, D., Luo, K., & Fan, J. (2022). Numerical Simulation of a 10 kW Gas-Fueled Chemical Looping Combustion Unit. *Energies*, *15*(6).

Thiemsakul, D., Kamsuwan, C., Piemjaiswang, R., Piumsomboon, P., & Chalermsinsuwan, B. (2021). Computational fluid dynamics simulation of internally circulating fluidized bed reactor for dry reforming of methane. *Energy Reports*, *8*. https://doi.org/10.1016/j.egyr.2021.11.008

Wang, M., Wu, Y., Shi, X., Lan, X., Wang, C., & Gao, J. (2019). Full-Loop Simulation of Gas-Solids Flow in a Pilot-Scale Circulating Fluidized Bed [https://doi.org/10.1002/ceat.201800542]. *Chemical Engineering & Technology*, *42*(4), 932-939. https://doi.org/https://doi.org/10.1002/ceat.201800542

Xu, T., Xiao, B., Fu, G., Yang, S., & Wang, X. (2019). Chemical looping hydrogen production with modified iron ore as oxygen carriers using biomass pyrolysis gas as fuel [10.1039/C9RA08936E]. *RSC Advances*, *9*(67), 39064-39075. https://doi.org/10.1039/C9RA08936E

Yang, S., Wang, H., Wei, Y., Hu, J., & Chew, J. W. (2019). Eulerian-Lagrangian simulation of air-steam biomass gasification in a three-dimensional bubbling fluidized gasifier. *Energy*, *181*, 1075-1093. https://doi.org/https://doi.org/10.1016/j.energy.2019.06.003

Yang, S., & Wang, S. (2020). Eulerian-Lagrangian simulation of the full-loop gas-solid hydrodynamics in a pilot-scale circulating fluidized bed. *Powder Technology*, *369*, 223-237. https://doi.org/https://doi.org/10.1016/j.powtec.2020.05.043

Yao, P., Yu, Z., Zhang, Y., & Xu, T. (2023). Application of machine learning in carbon capture and storage: An in-depth insight from the perspective of geoscience. *Fuel*, *333*, 126296. https://doi.org/10.1016/j.fuel.2022.126296

Yu, Z., Yang, Y., Yang, S., Zhang, Q., Zhao, J., Fang, Y., Hao, X., & Guan, G. (2019). Iron-based oxygen carriers in chemical looping conversions: A review. *Carbon Resources Conversion*, *2*(1), 23-34. https://doi.org/https://doi.org/10.1016/j.crcon.2018.11.004

Zheng, H., Jiang, X., Gao, Y., Tong, A., & Zeng, L. (2022). Chemical looping reforming: process fundamentals and oxygen carriers. *Discover Chemical Engineering*, *2*(1), 5. https://doi.org/10.1007/s43938-022-00012-3

Zhou, L., Zhang, L., Bai, L., Shi, W., Li, W., Wang, C., & Agarwal, R. (2017). Experimental study and transient CFD/DEM simulation in a fluidized bed based on different drag models [10.1039/C6RA28615A]. *RSC Advances*, *7*(21), 12764-12774. https://doi.org/10.1039/C6RA28615A

Zhu, X., Imtiaz, Q., Donat, F., Müller, C. R., & Li, F. (2020). Chemical looping beyond combustion – a perspective [10.1039/C9EE03793D]. *Energy & Environmental Science*, *13*(3), 772-804. https://doi.org/10.1039/C9EE03793D

Appendix A: Probe setting

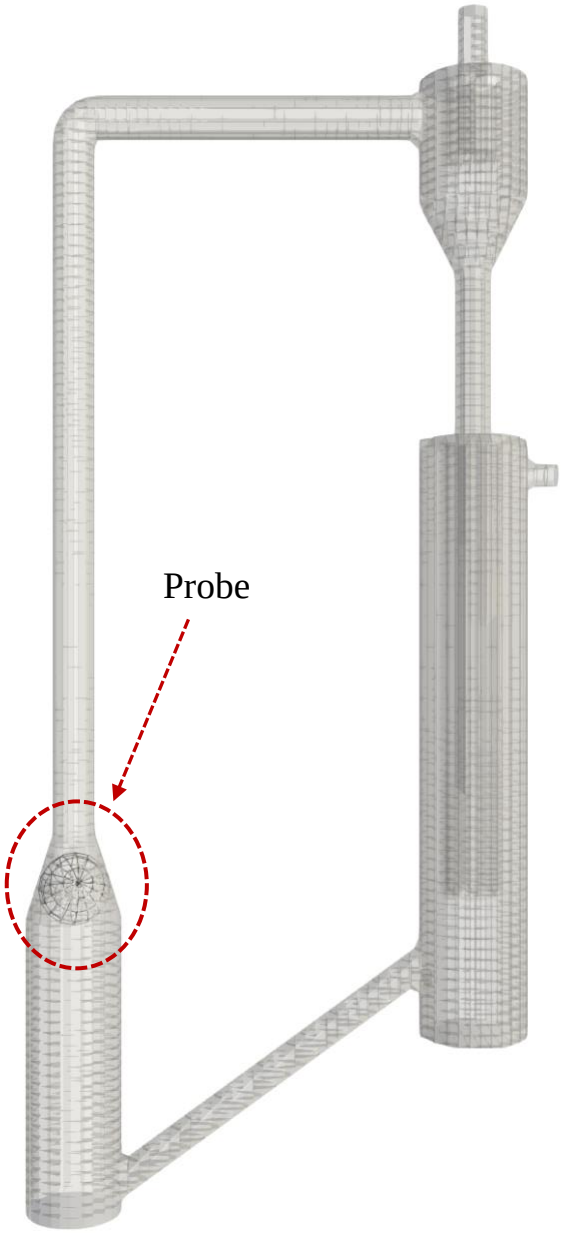

Figure 54. Selection of probe at specific zones to determine data such as pressure, volume fraction and pressure

Note: The probe selection is done in post-processing software PARAVIEW and the zones for the probes are defined to extract data such as pressure, volume and volume fraction.

Appendix B: Meshing

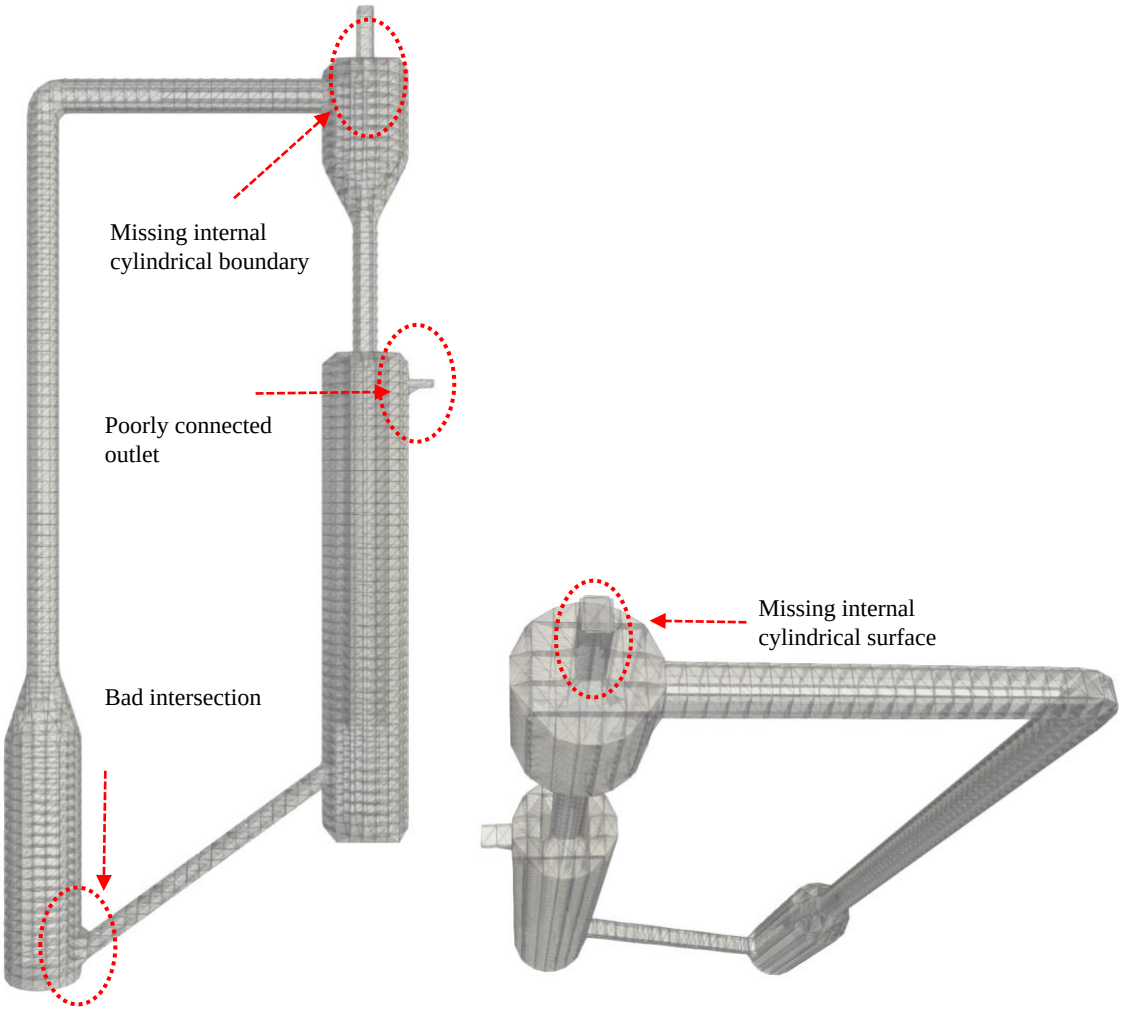

A **B**

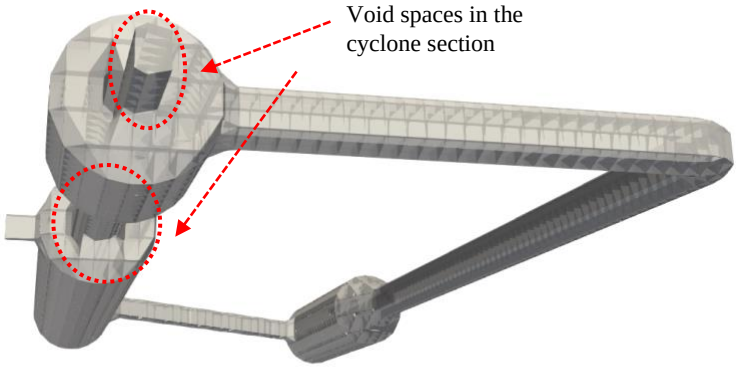

C

Figure 55. Poor meshing as a result of higher cell size selection

Note: For figure 55 A and B, the cell size in X, Y and Z direction is 0.0128m, 0.0112m, and 0.0184m. due to poor cell size, the connection zones of connection loop and pressure outlet are not properly merged with the geometry. The cyclone distributor has a pressure outlet, but the internal walls are missing because the wall geometry is very refined while the mesh isn't well defined.

For figure 55 C, the cell size in X, Y and Z direction is 0.0112m, 0.0112m, and 0.0184m. The cell size comparatively better than the above, but still not well defined. As it can be seen from the cyclone distributor section, there are void spaces near the pressure outlet. These poor spaces are due to improper meshing, and it can be improved by further reducing the cell size.